Numerical model development and analysis of a drop-on-demand inkjet application

Patrick Wagner

LUND
UNIVERSITY

Department of Energy Sciences

This degree project for the degree of Master of Science in Engineering has been conducted at the Division of Fluid Mechanics, Department of Energy Sciences, Faculty of Engineering, Lund University in collaboration with the Virtual Modelling team at Tetra Pak Packaging Solutions AB and FS Dynamics.

Main supervisor at Tetra Pak Packaging Solutions AB was Aurelia Vallier. Main supervisor at FS Dynamics was Emma Gustavsson. Supervisor at the Division of Fluid Mechanics was Senior lecturer Hesameddin Fatehi. Examiner at Lund University was Researcher Robert-Zoltán Szász.

Msc Thesis
ISRN LUTMDN/TMHP-24/5580-SE
ISSN 0282-1990

Department of Energy Sciences
Lund University
Box 118
SE-221 00 LUND
Sweden

Lund 2024

Abstract

The jet breakup and the potential occurrence of satellite droplets play a crucial role in the print quality of drop-on-demand (DOD) systems. This thesis focuses on developing a numerical model to simulate droplet formation utilizing the volume-of-fluid (VOF) method. A particular focus is on the occurrence of satellite droplets and how different fluid properties influence the jetting behaviour. The research centres on a printhead with a native droplet size of 2-3 pL and limited data availability. Therefore, an inlet boundary approximation method is developed to accurately simulate the droplet formation for different actuation waveforms. The study utilized the software StarCCM+ and experimental results from a JetXpert dropwatcher for the creation of the numerical model. With the developed approximation method, a validated model was created that effectively captures both droplet formation and velocity. Multiple experimental observations were recreated after the calibration process, successfully predicting the tail breakup. Finally, the validated model was used to investigate the effect of viscosity, density, surface tension and contact angle on the droplet formation process.

Keywords: Drop-on-demand (DOD) Ink Jetting, Volume-of-fluid (VOF) Method, Newtonian Fluid, Waveform Approximation, Satellite Formation

Acknowledgements

I would like to express my deepest gratitude to all those who have supported and guided me throughout the course of this thesis.

Firstly, I am immensely grateful to all my supervisors for their insightful guidance and continuous support. Their expertise and encouragement have been invaluable and were crucial in the successful completion of this work.

I want to thank my university supervisor, Hesameddin Fatehi, who provided exceptional guidance and support.

I also extend my deepest gratitude to my external main supervisors at Tetra Pak, Aurelia Vallier, and at FS Dynamics, Emma Gustavsson. Their practical insights and constant support were vital throughout this project.

Furthermore, I am deeply thankful to my additional supervisors at Tetra Pak, Eskil Andreasson, and at FS Dynamics, Mikael Fredenberg and Björn Ullbrand. Their feedback and expertise greatly enhanced the process of this work.

I wish to thank my family for their unwavering support throughout my personal and professional life.

Lastly, I want to thank my girlfriend for her support and encouragement throughout the last years and her patience in the last months in particular.

Contents

List of Figures

List of Tables

Nomenclature

Latin characters

v	Velocity	$\mathrm{m\,s^{-1}}$
A_p	Pressure Amplitude	Pa
A_V	Voltage Amplitude	V
d_∞	Characteristic Length	m
g	Standard Gravitational Acceleration	$9.81\,\mathrm{m\,s^{-2}}$
L_η	Viscous Length Scale	m
n	Normal Vector	–
S	Source Term	–
t	Time	s
V	Volume	$\mathrm{kg\,m^{-3}}$
x	Jetting Direction	m

Greek characters

β	Transformation Coefficient	$\mathrm{Pa\,V^{-1}}$
η	Dynamic Viscosity	$\mathrm{Pa\,s}$
γ	Surface Tension	$\mathrm{N\,m^{-1}}$
ν	Kinematic Viscosity	$\mathrm{J\,kg^{-1}\,s}$
ω	Resonance Period	s
Φ	Nozzle Angle	°
ρ	Density	$\mathrm{kg\,m^{-3}}$
Θ_a	Advancing Contact Angle	°
Θ_{eq}	Equilibrium Contact Angle	°
Θ_r	Receding Contact Angle	°

ζ	Dampening Factor	–

Abbreviations

Bo	Bond Number
$FENE$	Finite Extensible Nonlinear Elastic
$HRIC$	High-Resolution Interface Capturing
$MEMS$	Micro-Electromechanical System
VOF	Volume Of Fluid
Ca	Capillary Number
CIJ	Continuous Inkjet
De	Deborah Number
DOD	Drop-on-Demand
Oh	Ohnesorge Number
Re	Reynolds Number
We	Weber Number

Introduction

Printing technologies have been around for centuries and are used in many different areas, including packaging, advertising, books, magazines, and bioprinting. Traditional methods have evolved over time into sophisticated systems that allow high precision at incredible speeds and low costs. These traditional systems often work with physical forms, such as rolls, plates or screens, that transfer a specific pattern onto a substrate. However, these technologies are limited in flexibility, since a pattern needs to be defined and manufactured in order to change the print. The development of digital printing methods, such as inkjet printing, has eliminated this constraint by gradually forming a desired image through the precise deposition of thousands of individual droplets.

The commercial development of inkjet printing technologies started during the 1970s, and has become a widely used printing method in all types of areas (Hoath 2016). In the last decades, a tremendous effort has been devoted to optimising the droplet generation process and the underlying physical mechanisms since printing speeds and quality demands constantly increase. Modern inkjet systems print on paperboard at around 250 m/min, with a resolution of 1200 dpi (Bauer 2024). Each droplet's diameter is roughly equivalent to that of a human hair, typically ranging between 10 and 100 micrometers. Creating precise droplets at this size and time scale is a challenging task influenced by many factors, including fluid properties, nozzle design, actuation mechanisms, and environmental conditions. An example of a droplet formation recorded by single flash imaging is presented in Figure 1.1 and shows the intricate formation process of individual drops. To increase the print quality, unwanted additional droplets must be prohibited. These are commonly referred to as satellite droplets and result from the uncontrolled and unstable ligament breakup during the jetting. This leads to misting and a reduction in print quality.

Tetra Pak drives innovation in the packaging industry and continues to develop and investigate new and intelligent packaging solutions. One of these processes involves the high-speed ink application on paperboard. Knowledge building in this field is essential for the company to understand, predict, and optimise this rapid ink-paperboard interaction and, therefore, increase the print quality. Different material characteristics of the ink can influence the printing process and should, therefore, be investigated.

Consequently, this thesis aims to develop a numerical model of the droplet formation process at a single printhead nozzle. The model should be able to simulate the occurrence of satellite droplets and enable an investigation regarding their occurrence.

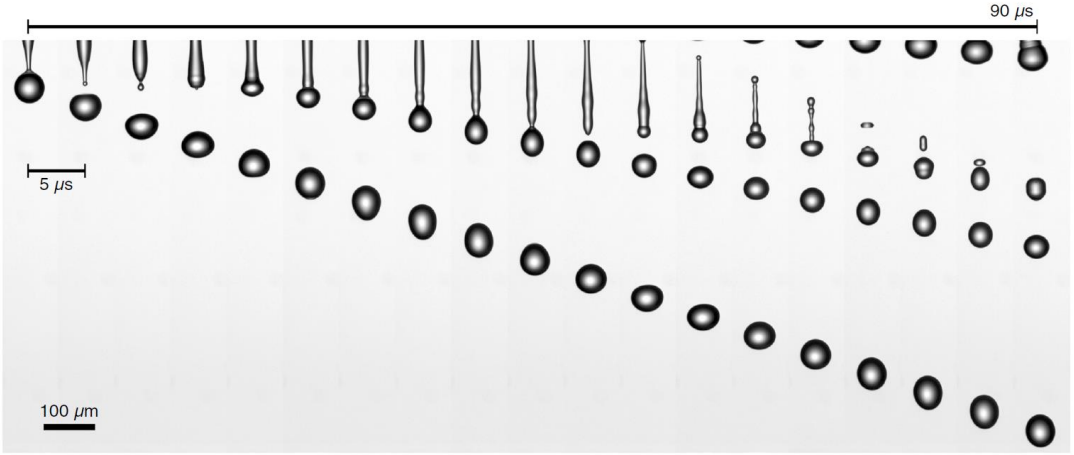

Figure 1.1: Stroboscopic sequence of an inkjet droplet, which breaks up into several droplets, recorded by Staat et al. (2017). Reprinted with permission from Springer Nature.

With the developed model, different fluid properties are investigated and their effect on the droplet formation and the ligament breakup. The biggest challenge in this project lies in the limited available information on the physical printhead and its properties, which complicates the creation of a numerical representation of the physical domain. As a consequence of the limited available data, an approximation method for the numerical boundary conditions needs to be developed.

To explore this issue, a literature review will be performed, focusing on ink characteristics, the printing process, numerical modelling, and prior research in fluid simulation. Various models will be examined during the review to assess their relevance and applicability to the process. With experimental cases from literature, first model validations will be conducted, to support the model development. Simultaneously, the real printing process is examined, and the physical model is described (setup, speed, pressure, ink characteristics, etc.). The physical model forms the basis for the numerical simulation and experimental data from the physical model will be used to aid the model creation and for the validation of the numerical process.

The structure of the thesis includes a brief introduction of the background theory that governs the inkjet process. Afterwards, the model development is described, an initial model validation with experimental data from literature is performed, and some brief analysis methods are presented in Chapter 3. Within Chapter 4, the conducted experimental tests with the printhead of interest are described, and a model approximation method together with a calibration strategy is developed. The model is further used to validate different experimental observations and analyse ink parameter influences on the droplet formation. The results from these investigations are presented in Chapter 5. A summary of the gained outcomes and achieved goals is subsequently given in Chapter 6, together with a future outlook. For each significant simulation result presented in this thesis, an overview of the selected model parameters for the corresponding simulation is provided in the appendix.

Theory

Inkjet printing is one of the most widespread applications of microfluidics (Lohse 2022). This technology progressively builds up a 2D image by depositing thousands of individual droplets on a stationary or moving substrate. Each droplet is typically in the range of 1 to 500 pL and moves at a speed of 5-8 m/s when hitting the substrate (Hoath 2016). To simulate this process effectively, a foundational grasp of the underlying mechanisms is necessary. Providing the needed fundamentals is part of this chapter, along with a review of prior research conducted within this domain.

2.1 Fundamentals

This section outlines the fundamental knowledge needed to establish an initial understanding of the inkjet process and its different working principles. Furthermore, it provides a quick overview of key fluid properties and dimensionless groups.

2.1.1 Technical Background

There are several different categories of inkjet print technologies, with the most general division being between continuous inkjet (CIJ) and drop-on-demand (DOD) printers (see Figure 2.1). With a CIJ printer, a continuous jet of liquid is ejected with a constant jetting pressure, which breaks into multiple droplets by an imposed disturbance on the liquid jet (Hoath 2016). The droplets are produced continually and reach well-controlled spacing and size due to the perturbation of the stream and its breakup. This droplet formation is mainly governed by the Rayleigh breakup principle which leads to evenly spaced droplets. In a DOD printer, individual droplets are ejected from separate nozzles through pressure pulses. This leads to a more controlled droplet ejection and much higher resolution and ink efficiency (Hoath 2016). A typical DOD printhead can contain over a thousand nozzle heads that are controlled separately and can fire on demand. The actuation mechanism has a strong influence on the controllability and the process of droplet formation in DOD printers. Several possible mechanisms are available, with the most typical classifications presented in Figure 2.1. Within this thesis, DOD printheads are investigated.

The two most common mechanisms for DOD printers are thermal (or bubble) actuation and piezoelectric actuation (Hoath 2016). The later one uses the piezoelectric effect in order to create actuation waves within the fluid. Piezoelectric elements change shape in the presence of an electric field, which is utilized to transfer energy to the fluid via a pressure change in the ink chamber (Hutchings and Martin 2013).

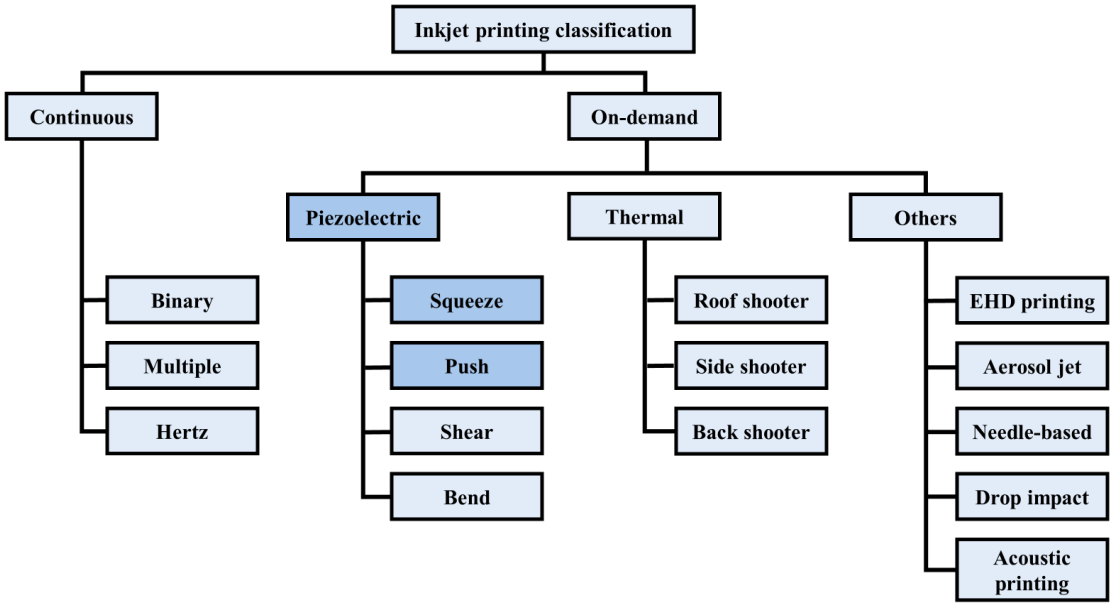

Figure 2.1: Categorization of different printing technologies, based on (Shah, D.-G. Lee, B.-Y. Lee, et al. 2021)

Depending on the arrangement and the orientation of the piezo element, different printhead designs have been developed and are commonly in use (see Figure 2.2). They can be divided into squeeze, push, shear, and bend modes. The designs covered in the remainder of this work include the bend and push constellation.

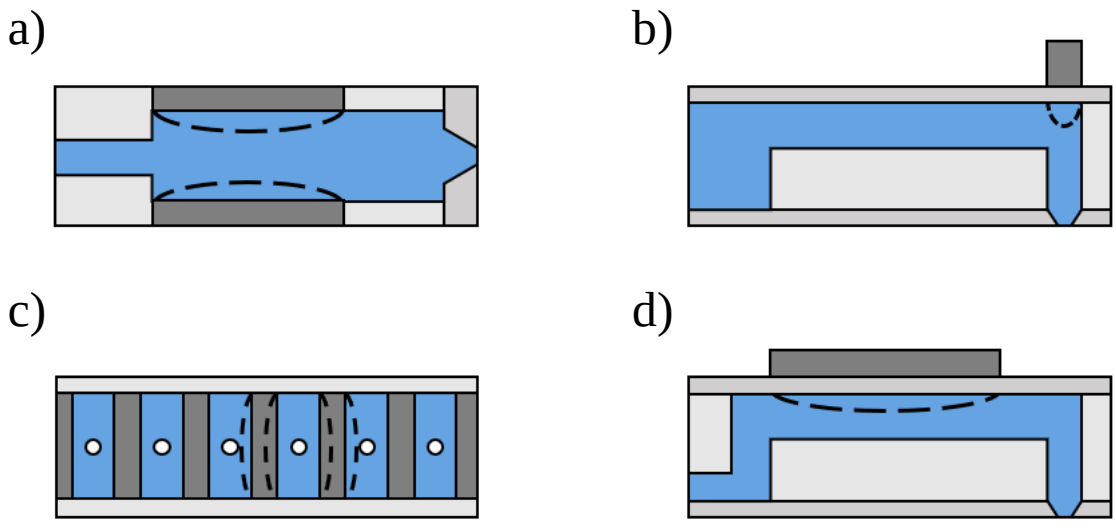

Figure 2.2: Working principle of piezo-driven printheads, based on (Shah, D.-G. Lee, B.-Y. Lee, et al. 2021). a) Squeeze Actuation b) Push Actuation c) Shear Actuation d) Bend Actuation

The way these actuators produce a droplet heavily depends on the electrical signal that is imposed on them. Since the piezo elements are controlled with a voltage

signal, there are generally two principal actuation modes that can be applied. The element can either contract initially and expand afterwards, resulting in a pull-push mode, or vice versa, leading to a push-pull actuation. Considering the delay of the electric signal and mechanical movement, this leads to the most commonly used standard voltage waveform, which is a single trapezoidal pulse. Figure 2.3 shows a schematic representation of a pull-push waveform consisting of a rise, dwell, and fall time. During the rise time, the piezo element expands, causing the ink in the chamber to be drawn in. Conversely, during the fall time, the piezo element contracts, exerting pressure to push the ink out of the nozzle.

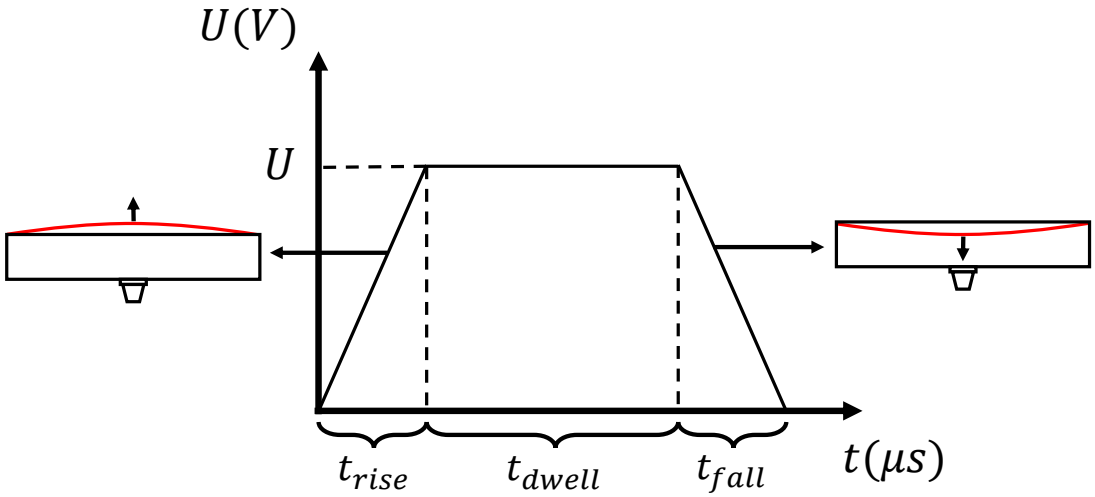

Figure 2.3: Schematic representation of a single unipolar rectangular pulse

Adding together multiple pulses with different amplitudes leads to the formation of more complex actuation methods, which can be classified into the different principles shown in Figure 2.4. Unipolar waveforms only use positive voltage signals, while bipolar mechanisms enable even further manipulations of the piezoelectric actuator. These combinations of pulses allow for possibilities to influence and optimise the jetting behaviour and the droplet formation. Some of the process parameters that can be influenced by the waveform include the velocity, volume, and tail breakup of the droplet. Some pulses can be added in order to influence the droplet behaviour itself, while others might serve the purpose of reloading the ink chamber or dampen residual vibrations at the nozzle. Choosing the correct waveform is, therefore, essential for the application and the chosen ink. The outcome of a waveform isn't consistent for various printheads, ink compositions, or even across individual nozzles. Variations between nozzles stem largely from geometric tolerances and minor irregularities. Thus, it's essential to assess a waveform's effectiveness across multiple nozzles and focus on the general droplet formation. Investigating the effect of waveform characteristics and their impact on droplet formation plays, therefore, a significant role in recent research and will also be a big part of this thesis.

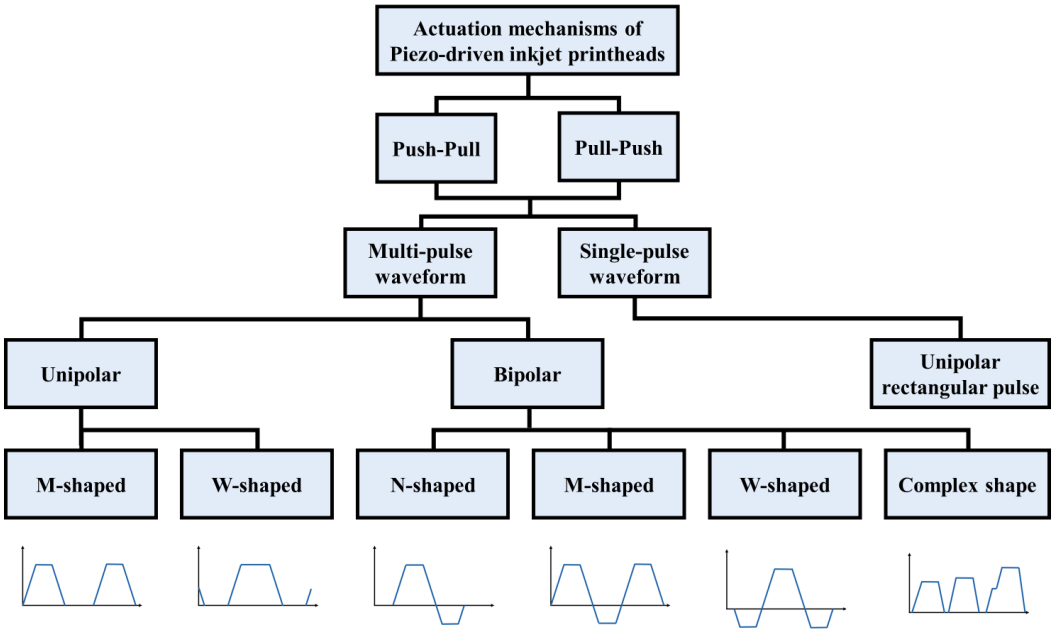

Figure 2.4: Classification of actuation waveforms for piezo-driven printheads, based on (Shah, D.-G. Lee, B.-Y. Lee, et al. 2021)

2.1.2 Fluid Properties

A fluid's behaviour is governed by a multitude of properties that can be used to characterise aspects like thermodynamics, kinematics or dynamics. This section presents the key properties relevant to the application in question: density, viscosity, surface tension, and contact angle.

Density

The first fundamental ink property is its density. Density ρ is defined as mass per unit volume and has the SI unit $[kg/m^3]$. The density of a fluid depends mainly on its components and to a lesser extent on the temperature of the fluid (Hoath 2016). The magnitude of inertial forces on a fluid is influenced by the density, which has an impact on the ink flow characteristics.

Viscosity

The viscosity is one of the critical properties that dominate the fluid behaviour of liquid jets and during the droplet formation in inkjet printing. The variable η describes the dynamic viscosity, while the variable ν refers to the kinematic viscosity. Without further specification, the term "viscosity" will refer to the dynamic viscosity in the following chapters. The SI unit of viscosity is [Pa s], but the unit centipoise [cP = mPa s] is also often used within inkjet applications. Liquids in inkjet printing are typically within a range of 2-50 mPa s (cP) (Hoath 2016).

Viscosity describes a fluid's resistance towards shear or flow deformation and highly depends on the attractive forces between individual molecules. With increasing temperature, the more energetic molecules lead to a rapid reduction of cohesive forces,

which makes viscosity strongly temperature-dependant (Hoath 2016).

For a Newtonian fluid, the viscosity is a constant and independent of the shear velocity. Fluids with a variable viscosity are known as non-Newtonian and can generally be classified as either time-independent, time-dependent, or viscoelastic fluid (Hoath 2016).

Surface Tension

Every fluid tends to form the shape with the lowest total energy. Without any external influence, this shape is a sphere. This behaviour is described by the surface tension γ, which reflects the fact that molecules at a free surface have a higher energy than those inside the bulk (Hoath 2016). This tendency leads to droplet and satellite formation in DOD printers. The SI unit of the surface tension is [N/m]. The unit dyn/cm = mN/m is also often found within ink applications. The typical surface tension range for inks falls within the magnitude of tens of mN/m.

An equivalent description of this property is the surface energy. In theory, a droplet can be formed through a nozzle, when the kinetic energy transferred outwards surpasses the surface energy of the meniscus. Both inertial forces and viscosity act against the contraction of the liquid due to surface tension (Hoath 2016).

Contact Angle

The extent to which a liquid wets a surface can generally be described with its equilibrium contact angle (Θ_{eq}). This angle defines the angle between the liquid phase and the vapour phase at a solid surface. The angle is achieved by the shape of the liquid drop, which aims to minimise the free energy of the system in the absence of gravity.

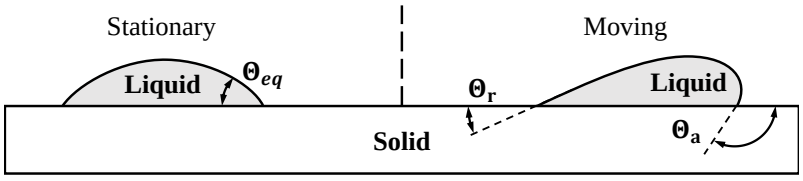

Figure 2.5: Schematic representation of different contact angles. At a stationary state, an equilibrium contact angle Θ_{eq} is defined. For a moving fluid, a receding contact angle Θ_r and advancing contact angle Θ_a govern the behaviour of the interaction.

Depending on the contact angle, different behaviour of the fluid-solid interaction is observed and classified (Hoath 2016). A contact angle below 90 degrees results in a wetting behaviour, while a contact angle above this angle leads to a non-wetting interaction. For a moving fluid, not only the equilibrium contact angle is of importance, but also two other angles. The receding contact angle Θ_r describes the smallest stable angle of a fluid, while the advancing contact angle Θ_a describes the largest stable angle. They can be measured by pushing or pulling a drop over a surface and recording the forming angle.

Polymers in Inkjet Printing

Polymers fulfil many roles in ink formulations and are often found in end-use applications of inkjet fluids (Hoath 2016). They are used as stabilizers to improve image permanence, influence ink-substrate interaction, disperse pigments, and control droplet generation, to name a few examples. Simulating a liquid containing polymers brings, however, a variety of additional challenges (Du, Yu, and Y. Han 2018). One of the biggest challenges is the significant non-Newtonian behaviour of polymer-infused solutions, affecting the droplet formation and the tail breakup. Only a few numerical models are currently in use that can approximate the non-Newtonian behaviour of ink mixtures to a certain degree. Research in this area still needs to be conducted. Commercial software solutions are often not equipped with the necessary fluid models to recreate the non-Newtonian ink effects. Due to this reason, there could not be an investigation on these kinds of fluids within this thesis. Nevertheless, a short overview of the effects of polymers is given in the following section, together with a brief summary of commonly used fluid models.

To describe the viscoelastic properties of low-viscosity inkjet fluids, small-strain oscillatory viscoelastic measurements are commonly used (Hoath 2016). With these techniques, three connected parameters are measured to describe the fluid behaviour: the elastic storage modulus G', the viscous loss modulus G", and the complex viscosity η^*. It is essential to measure these properties at high frequencies because of the low relaxation time of low-viscosity inkjet fluids, which makes special rheometers necessary.

Special fluid models are required to simulate these properties. One of the prominent models is the finite extensible nonlinear elastic (FENE) model. These types of models are specifically created to model polymer solutions and are often referred to as dumbbell models (Alves, Oliveira, and Pinho 2021). These models can represent special properties of polymer solutions that are vital for the simulation process, like fluid elasticity, the orientation of the macromolecules relative to the strain axes, and their finite extensibility. The FENE-CR variation is often used for viscoelastic inkjet applications since it simplifies the model by removing the molecular interpretation and the complications introduced by a shear-thinning viscosity (Alves, Oliveira, and Pinho 2021). These models are mostly unavailable in commercial CFD software packages and are often implemented in open source tools.

The effects of non-Newtonian properties can be seen in a research by Morrison and Harlen (2010). In Figure 2.6, the simulated jetting behaviour of four different viscoelastic inks is presented and compared to a Newtonian fluid. All boundary conditions and density, viscosity, and surface tension are constant among all the simulations. Nevertheless, a substantial difference in the formation process can be observed. This includes phenomena like 'beads-on-a-string', as can be seen in case (b). For their simulations, a FENE-CR fluid model was implemented, with c being the polymer concentration, *De* the Deborah number, and L the extensibility of the polymer. These parameters are directly related to the molecular weight and elastic modulus of the dilute polymer solution.

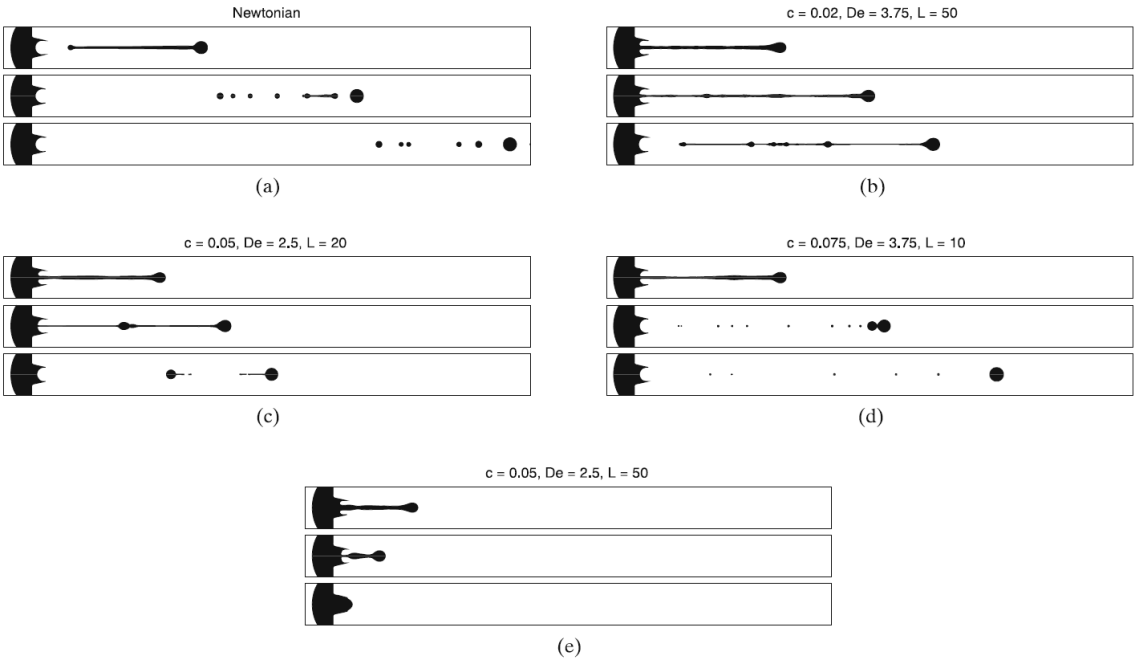

Figure 2.6: Axisymmetric DOD simulations for five viscoelastic fluids, with different polymer contents. All fluids have the same density, viscosity and surface tension. Reprinted from (Morrison and Harlen 2010) with permission of Springer Nature.

The complexity of the jetting mechanisms for non-Newtonian inks has been extensively described by Clasen et al. (2011). Their study investigates the dispensing of different Newtonian and non-Newtonian fluids and defines an operating space called a "map of misery". They show the different problems that can occur when dispensing rheologically complex fluids and how they depend on different properties and flow phenomena.

2.1.3 Dimensionless Groups

Dimensionless numbers are commonly used in fluid dynamics to express the ratio of various forces. This provides a convenient way to analyse and characterize the behaviour of fluids and make different properties comparable. The formation of droplets primarily depends on inertia, viscosity, and surface tension, and four dimensionless numbers, the Reynolds, Weber, capillary, and Ohnesorge number, are key in characterizing their importance (Lohse 2022).

The Reynolds number Re is the ratio of inertial to viscous forces and is defined as:

$$Re = \frac{\rho v d_\infty}{\eta} = \frac{v d}{\nu} \tag{2.1}$$

where ρ is the density, v is the flow speed, d_∞ is the characteristic length, η is the dynamic viscosity, and ν is the kinematic viscosity. The radius of the nozzle is commonly used as the characteristic length for droplet formation processes.
The Weber number We is the ratio of inertial to capillary forces and is defined by:

$$We = \frac{\rho v^2 d_\infty}{\gamma} \tag{2.2}$$

where γ is the surface tension of the fluid.
The capillary number Ca is the ratio of viscous to surface tension forces and is defined as:

$$Ca = \frac{We}{Re} = \frac{\eta v}{\gamma} \tag{2.3}$$

The Ohnesorge number Oh is the ratio of the viscous timescale ($t_{visc} \sim \eta d_\infty / \gamma$) to the capillary timescale ($t_R \sim \sqrt{\rho d_\infty^3 / \gamma}$) and is defined as:

$$Oh = \frac{\sqrt{We}}{Re} = \frac{\sqrt{\rho v^2 d_\infty}}{\sqrt{\gamma}} \cdot \frac{\eta}{\rho v d_\infty} = \frac{\eta}{\sqrt{\gamma \rho d_\infty}} \tag{2.4}$$

With this number, the external dynamics (e.g., the jet velocity) is cancelled out. This results in a fluid description, that only depends on the characteristic length of the drop and its fluid properties.

In inkjet printing, the Ohnesorge number is of high importance to describe the dynamic processes that are controlling the breakup, as well as the shape and size of the ejected droplets (Derby 2010). Together with the Reynolds number, it can be used to create an operation diagram for ink properties (see Figure 2.7). Only an intermediate range of Reynolds and Ohnesorge numbers results in printable ink behaviour. If Oh gets too large, the ink is too viscous to be jetted, while a low Oh will result in a large number of satellite droplets. Likewise, if Re gets too small, the ink is not jettable due to low actuation forces, while a large Re results in splashing on the substrate.

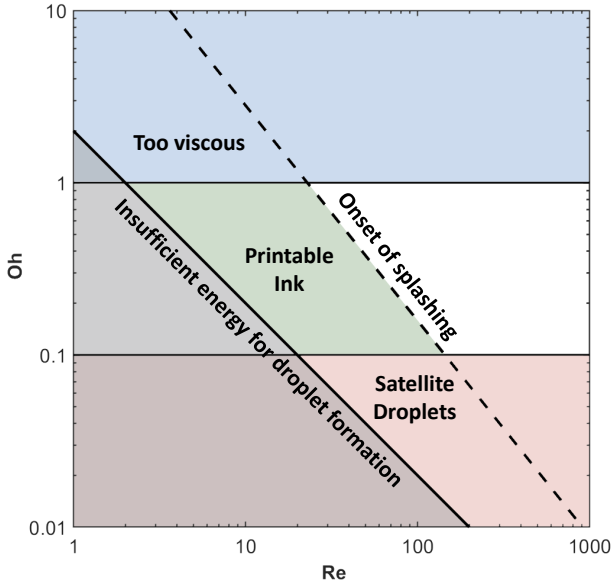

Figure 2.7: A schematic diagram, showing the operating regime for stable operation of drop-on-demand inkjet printing. The Figure is adapted from Derby (2010).

The inverse of the Ohnesorge number (Z=1/Oh) is sometimes used in literature to define the range in which liquids can be printed. The printable range that is proposed through numerical studies by Reis and Derby (2000) is defined from 10>Z>1. Tai et al. (2008), on the other hand, define a range of 50>Z>0.67 and successfully prove jetting of droplets within this range, stating that Oh is not sufficient to define a printable ink. Other factors like dwell time, driving voltage and waveform play a crucial role in the droplet formation as well. Other researchers also report ranges like 14>Z>4 for stable drop formation (Jang, D. Kim, and Moon 2009).

2.2 Drop Formation in Inkjet Printing

A comprehensive understanding of the droplet formation is essential to investigate and understand the behaviour of ejected liquid. In Figure 2.8, the DOD droplet formation process is schematically represented and divided into six steps. Initially, the liquid within the nozzle is in an equilibrium state with zero velocity (A). After an actuation is induced, the liquid is pushed out of the nozzle (B). When a certain amount of fluid is pushed through the nozzle, the head droplet starts forming, and the necking of the fluid begins due to surface tension (C). The liquid continues to move out of the nozzle and forms an extending ligament of fluid, which attaches the head droplet to the meniscus (D). The surface tension forces lead to the pinch-off of the liquid ligament and the formation of a tail droplet (E). Afterwards, the liquid tail begins to catch up with the main droplet and ideally condenses into it (F).

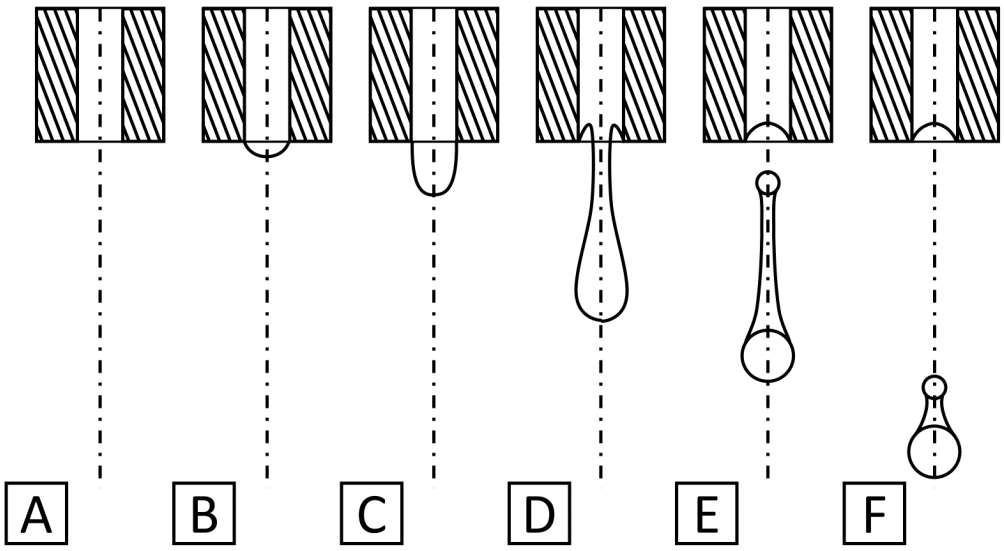

Figure 2.8: Six stages of the droplet formation process, based on (Hutchings and Martin 2013). A: Equilibrium state B: Beginning of actuation C: Moment before necking D: Tail formation E: Tail droplet formation F: Recombining of tail and head droplet

This general division leads to different aspects of the process that influence the final droplet. Those aspects include the head droplet formation, the pinch-off, the tail behaviour and the satellite formation. In the next section a detailed description of these individual parts will be provided.

2.2.1 Actuation Mechanism

Before looking at the droplet formation itself, the actuation mechanism has to be further specified. A simplified geometry of an inkjet device is used in Figure 2.9 to explain the actuation process, according to Hoath (2016). A single unipolar rectangular pulse, as presented in Figure 2.3, is applied to the piezoelectric element on the side of the ink chamber. The first ramp leads to an enlargement of the ink channel, which results in a negative pressure wave. During the dwell time, this pressure wave splits and travels through the ink chamber. At the reservoir, this wave is reflected and becomes a positive pressure wave based on the propagation theory and reflection rules of acoustic waves. The negative pressure wave at the nozzle leads to the pull motion of the ink. The reflected positive pressure wave is amplified by the second slope of the actuation waveform, resulting in a large positive pressure peak. Once it reaches the nozzle, this superimposed wave leads to the jetting of a droplet.

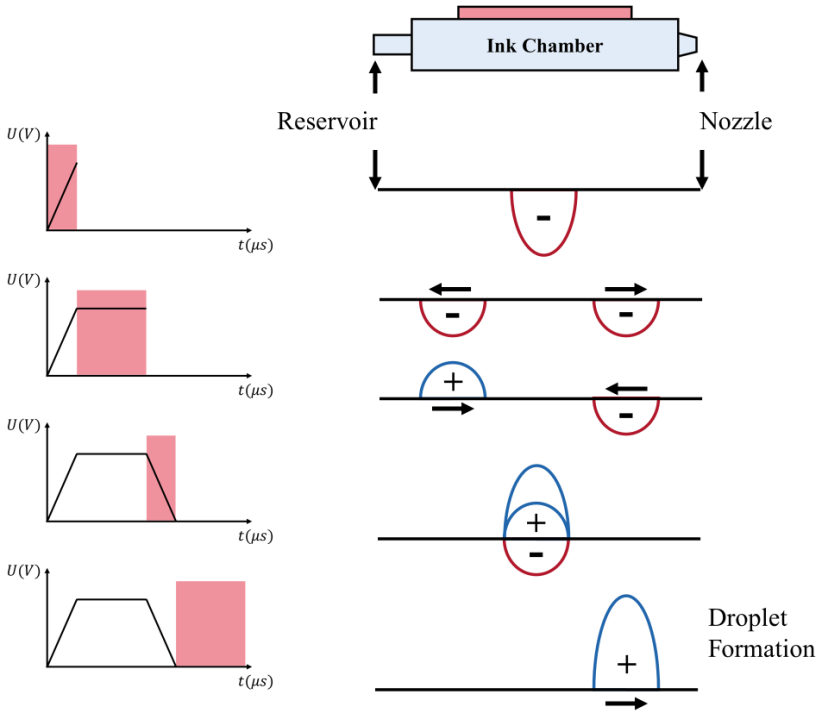

Figure 2.9: Schematic representation of the actuation principle. A negative pressure pulse is induced during t_{rise}, which travels through the ink chamber and reflects at the reservoir during t_{dwell}. The pulse is superimposed with a positive pressure pulse during t_{fall}. This positive interference leads to a high pulse that results in the droplet jetting at the meniscus. Diagram based on Hoath (2016).

Every nozzle within the printhead is actuated by a separate piezoelectric actuator. Due to the close proximity of the nozzles, this can also result in crosstalk between different nozzles. This challenge has been subject of research and is discussed by many articles (Wijshoff 2008). Possible preventive measurements are dampening modules between different nozzles or reducing residual vibrations with complex waveforms.

2.2.2 Head Drop Formation

The head drop formation marks the first step in the droplet ejection process. During this part, the size and velocity of the final head drop are established (Hoath 2016). The process is dominated by hydrostatic pressure, viscosity forces, fluid inertia and surface tension force.

When the pressure wave reaches the nozzle, the fluid starts to flow outwards with an increasing speed, forming a liquid cylinder with the same cross-sectional dimensions as the nozzle (Hutchings and Martin 2013). While the fluid is leaving the nozzle, additional free surface is created, which leads to an increase in surface energy. The velocity of the liquid column increases until the capillary forces lead to the necking of the liquid jet. The condition for a successful droplet formation is reached when the kinetic energy conveyed by the fluid matches the kinetic energy of the droplet and the additional extra free surface energy (Hutchings and Martin 2013). The amount by which this relation exceeds unity directly influences the final droplet velocity. This velocity should be high enough to overcome any decelerating action of the ambient air, establishing the jetting threshold. According to a model by Feng (2002), the final speed of an ejected droplet is between one and two-thirds of the maximum average velocity of the fluid within the nozzle during actuation.

Controlling the volume and velocity of the head droplet is one of the most important aspects of DOD printing. Along with ink properties, the chosen actuation waveform is the primary tool for fine-tuning these parameters. Different researches have shown that the velocity and volume of the droplets are linearly dependent on the amplitude of the driving signal for a simple rectangular input pulse with a constant pulse width (Technote 1999, Hamad, Salman, and Mian 2020, Seerden et al. 2001). This can be explained by the linear correlation between the volume change of the piezoelectric actuator and the applied voltage (Erqiang 2010). Regarding the pulse width, on the other hand, a maximum for both velocity and volume can be observed at a specific pulse width. The correlation between these properties and pulse width exhibits an almost quadratic trend. While the pulse width corresponding to maximum velocity remains consistent across varying input amplitudes, it shifts in response to changes in fluid properties (Seerden et al. 2001). Both effects are shown in Figure 2.10 and Figure 2.11. The presented results have been collected experimentally by Technote (1999).

A multi-pulse ejection method can be applied to further influence the droplet volume. This method uses multiple pulses in quick succession to increase the droplet volume significantly. Another possible use is the suppression of satellite droplets, as has been shown experimentally by (Oktavianty et al. 2019). Figure 2.12 schematically shows the stacking of 5 head droplets into a single drop through the use of five pulses in quick succession. With this method a wide range of droplet volumes (5-28 pL) can be achieved while maintaining a similar velocity.

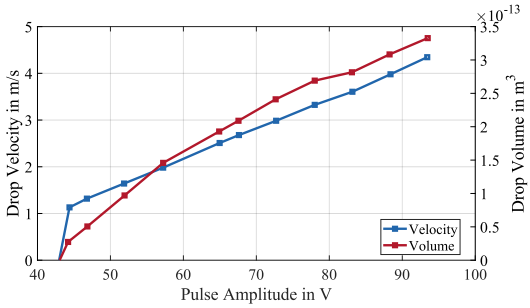

Figure 2.10: Velocity and volume change of the ejected droplet with varying pulse amplitudes and constant pulse width, recreated with data from (Technote 1999).

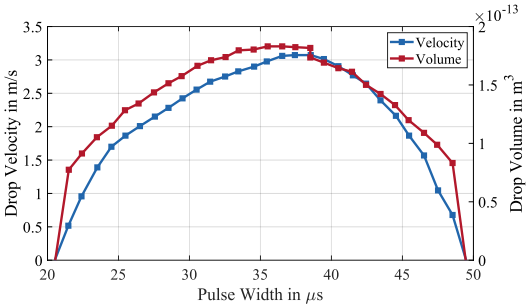

Figure 2.11: Velocity and volume change of the ejected droplet with varying pulse widths and constant pulse amplitude, recreated with data from (Technote 1999).

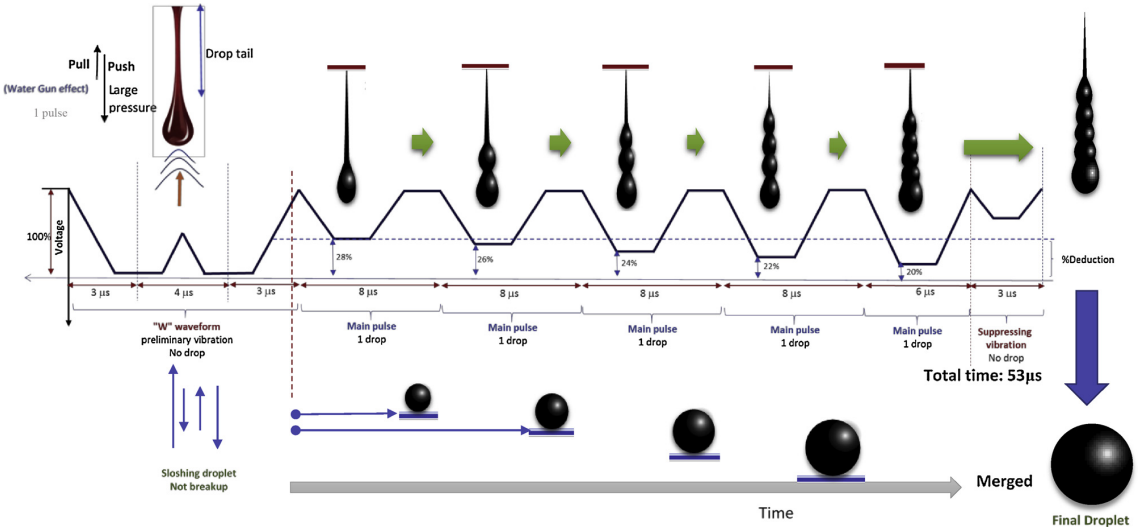

Figure 2.12: Conceptual sketch of a multi-drop ejection, by Oktavianty et al. (2019). Reprinted with permission from Elsevier.

2.2.3 Pinch-Off and Tail Breakup

Pinch-off and tail breakup are the primary processes in droplet formation, ultimately resulting in the creation of the final droplet. These mechanisms are also responsible for the occurrence of unwanted satellite droplets. Depending on their speed, these additional droplets can recombine with the primary drop or remain separated. Figure 2.13 shows two exemplary droplet formations as sequences of stroboscopic pictures (Hoath 2016). On the left, a low actuation amplitude is chosen, which results in a slow droplet. The tail remains stable after pinch-off and recombines with the head droplet. On the right, a 25% higher amplitude was induced, which results in a faster drop speed. The tail can not merge with the head droplet before it breaks down into multiple satellite droplets due to capillary instabilities. Generally, the most forward droplet in the process is called the head droplet or primary droplet, while all droplets that emerge from the tail are considered satellite droplets (Zhao et al. 2021). The satellite droplets typically have a volume that is an order of magnitude smaller than the main droplet (Zhang et al. 2022). In this example,

the satellites recombine with the head droplet after a certain time. This shows the complex challenges of producing satellite-free droplets at high speed. Some of the essential breakup mechanisms are shortly presented in this section.

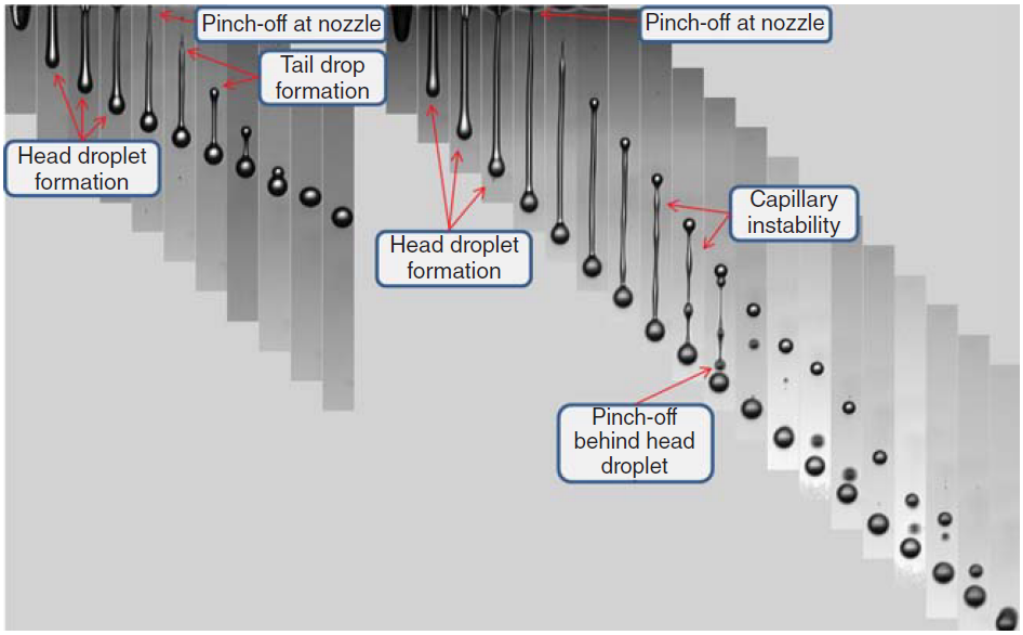

Figure 2.13: Two examples of a possible droplet formation. Left: slow head droplet with a stable recombining tail. Right: fast head droplet with a longer tail that breaks down into multiple satellite droplets. Reprinted from (Hoath 2016) with permission from John Wiley and Sons.

The first mechanism that occurs, is the pinch-off. During this process, a liquid ligament gradually thins until it breaks apart due to surface tension. The general procedure of pinch-off in DOD application can be summarized as follows. Once the ink is ejected from the nozzle exit, a liquid ligament starts to form behind the head droplet. As the pressure in the ink chamber decreases, no more ink is jetted out of the nozzle, leading to a thinning of the ligament between the primary droplet and the meniscus. Pinch-off occurs when this ligament detaches from the meniscus. A tail droplet is formed at the end of the ligament because of capillary tension, as can be seen in Figure 2.13. Surface tension causes the tail droplet to accelerate toward the primary droplet. As it moves, the tail droplet decelerates while gathering ink from the tail, thereby increasing in volume. Depending on the initial length and velocity of the tail, it can either recombine with the primary droplet, or break up into satellite droplets, as seen in the example on the right.

The process of pinch-off is influenced by many effects and is often caused by instabilities, which makes the prediction of its characteristics a complicated task (Hoath 2016). In a DOD printer, the droplet formation is governed by a oscillation of the ink within the nozzle. This oscillation leads to an unclear pinch-off, since the meniscus can retract and be pushed out multiple times before the ligament detaches. An advancing meniscus consumes parts of the tail, while a retracting meniscus pulls parts of the ink with it, leading to a local thinning (Hoath 2016). This results in a so-called secondary tail formation, which is much smaller than the primary ligament.

Resolving this secondary tail experimentally or numerically can be challenging. Experiments by Fraters et al. (2020) could show a diameter on the order of 1 μm for secondary tails and could even show the existence of tertiary and quaternary tails. This makes it challenging to calculate or determine the exact moment of pinch-off. However, this moment is crucial for the subsequent development and breakup behaviour of the ligament. The longer the main droplet remains connected to the meniscus or tail, the more it decelerates (Hutchings and Martin 2013). This effect is particularly pronounced for larger droplets or high-viscosity inks. The timing of the pinch-off and breakup also influences the tail droplet's velocity, affecting its ability to catch up to the main droplet (Hoath 2016).

Additionally, the wettability of the nozzle significantly influences the pinch-off of the droplet tail and the formation of satellite droplets. Figure 2.14 shows how different wall treatments influence the droplet formation behaviour. An investigation by Yang et al. (2017) showed how different ink-phobic or ink-philic nozzle properties can reduce or increase the probability of satellites. By using a superhydrophobic nozzle, the pinch-off of the ink could be accelerated, resulting in a shorter ligament and, thus, a lower probability of satellite droplets. Also, an impact on the droplet size could be observed depending on the wettability.

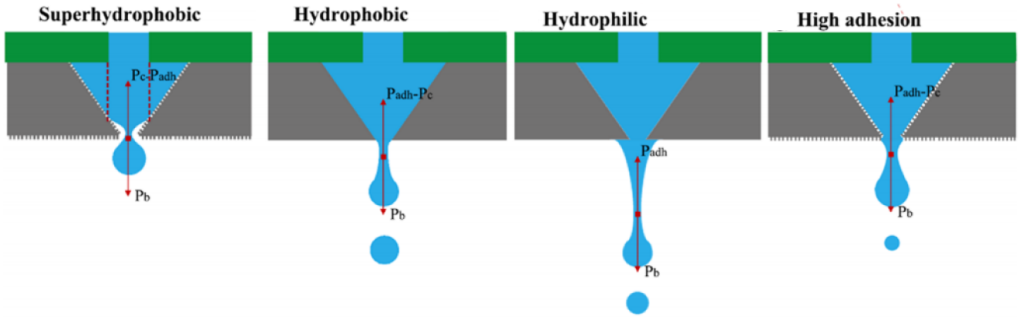

Figure 2.14: Effect of different wettability characteristics of the nozzle regarding the pinch-off. Reprinted from (Zhang et al. 2022) with permission from MDPI.

Besides the effect on the direct droplet formation, there are multiple other effects and risks that are related to the wettability of the nozzle. A surrounding nozzle film formed from a hydrophilic nozzle can for example lead to the transportation of dirt particles towards the meniscus or influence the droplet formation by drying ink remainders (Lohse 2022). The remaining ink at the meniscus can also influence the droplet formation of multiple sequentially fired droplets.
The second important breakup mechanism is the Rayleigh-Plateau breakup, due to instabilities. This mechanism mostly occurs for viscous and long filaments ($Oh \geq 0.1$) and is extensively described by Conto (2019). According to the theory, sinusoidal perturbations with a time dependent amplitude are assumed to act on a liquid interface. The perturbation grows linearly over time, until the fastest growing instability reaches the value of the unperturbed jet radius. This leads to the breakup of a ligament jet into multiple evenly spaced droplets. The wavelength of the most rapidly growing disturbance is roughly 4.5 times the diameter of the liquid jet (Hoath 2016). While this breakup is essential for CIJ applications, it is mostly unwanted in DOD printers and leads to satellite droplets. The instability is not induced by DOD print-

heads; instead, it occurs naturally and unpredictably in long filament tails (Hoath 2016).

The different breakup mechanisms are illustrated in Figure 2.15 for a detached ligament jet with an initially constant cross section. The top scenario illustrates a ligament contracting fully into a single droplet without any breakup, the middle scenario displays the formation of multiple droplets along the ligament due to Rayleigh-Plateau instability, and the bottom scenario displays pinch-off due to capillary tension at the ends of the ligament.

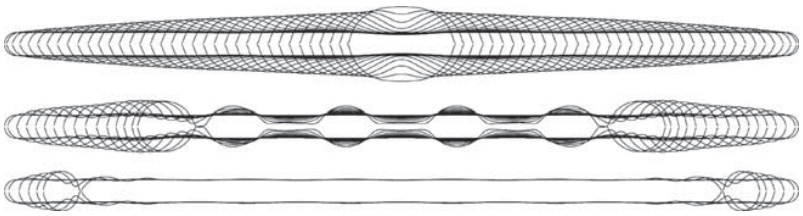

Figure 2.15: Schematic representation of different ligament breakup mechanisms. Top: Recombining of the ligament into a single droplet. Middle: Breakup of the ligament due to Rayleigh-Plateau instability. Bottom: Pinch-off at the ends of the ligament. Reprinted from (Driessen et al. 2013) with permission from AIP Publishing.

2.3 Jetting Simulation

The simulation of the DOD process has to deal with a number of challenges that originate in the complexity of the process. In the following section some commonly used simulation methods and strategies are discussed.

For the droplet formation process, axisymmetric and three-dimensional models are common choices when simulating the jetting behaviour. Since the flow of the liquid can be assumed to be mainly extensional, an axisymmetric model can be suitable to simulate the droplet and satellite formation. Many aspects of the process can be represented in this simplified approach while at the same time reducing the necessary computing time. A research by Castrejon-Pita et al. (2011) compared experimental data and axisymmetric simulations of a large scale DOD model. The inlet velocity of the nozzle was measured using laser anemometry. The findings indicate that the axisymmetric model closely aligns with observed behaviours. Another study by Wijshoff (2008) similarly demonstrated strong agreement between an axisymmetric model and experimental data. In his model, Wijshoff used acoustic wave propagation and a narrow channel model to simulate the pressure waves within the nozzle head. However, an axisymmetric model assumes cylindrical symmetry of the nozzle and the jet, which can be too restrictive in order to analyse certain characteristics of interest. Possible applications for a three-dimensional model include simulating nozzle defects, droplet deflection due to air flow, and droplets hooking onto the nozzle side (Meulen 2015).

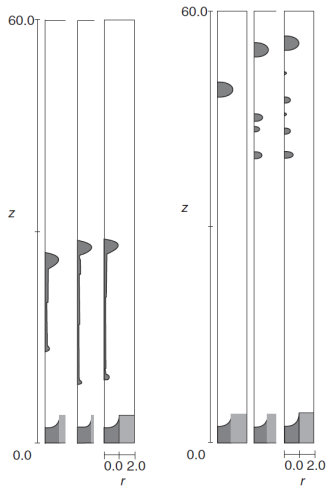

Figure 2.16: Qualitative comparison of the simulation results with different mesh refinements. Reprinted from (Hoath 2016) with permission from John Wiley and Sons.

When adopting a simulation model, many properties influence the behaviour of the droplet formation (Hoath 2016). As stated in Hoath (2016), commercial software packages often lack access to all the necessary adjustments to describe the droplet formation process fully, especially when considering non-Newtonian fluid behaviour. Furthermore, reaching mesh-convergence within an acceptable tolerance can be a challenge. As shown by the qualitative comparison in Figure 2.16, three different levels of mesh refinement with otherwise equal settings and parameters can lead to clear differences between the observed results. A coarse mesh predicts a smaller tail with no satellite formation, while the two finer mesh resolutions predict slightly different satellite formation. Depending on the requirements, these differences might be considered negligible. Similar mesh convergence problems have been observed and described by multiple researchers (Lei, J. Han, and H. Liu 2022, Coşar et al. 2023). A recommended convergence test by Hoath (2016) consists of the comparison with experimental results and adjusting the mesh and the satellite prediction accordingly.

An approximation of the inlet boundary conditions is essential for the successful simulation of a DOD system. Furthermore, the simulation method needs to be able to simulate a multiphase flow to resolve the fluid, which is dispersed in air. Both aspects are briefly presented in the following sections.

2.3.1 Actuation Waveform

The actuation waveform is the main driver of the droplet formation and, therefore, the most sensitive part of the simulation (Hoath 2016). Typically, the process within the printhead is a coupled multiphysics problem that involves the transportation of energy across different physical domains. An electric signal is coupled to the mechanical deformation of the piezoelectric element, which results in an acoustic energy transportation in the fluid and concludes as kinetic energy within the ejected droplet (Figure 2.17). For the numerical investigation of this thesis, only the creation of a stand-alone nozzle model is considered. This is due to the limited information on

the printhead itself, its characteristics and its dimensions.

Predicting the waveform at the boundary of a stand-alone nozzle model is a challenge, since the flow within the nozzle chamber is not always well known. Therefore, approximations of the waveform may be used that require some form of calibration with experimental data to provide relevant results.

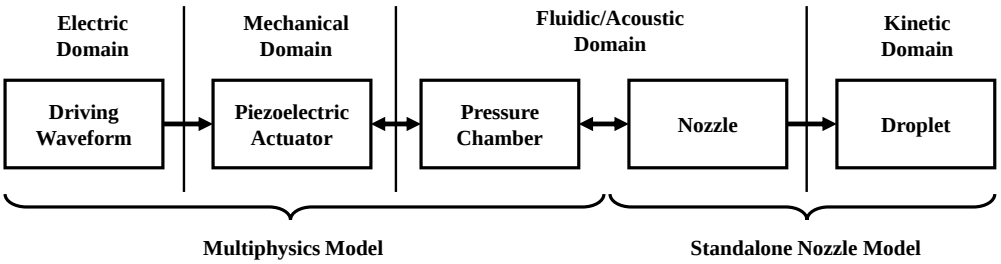

Figure 2.17: Schematic representation of the different physical domains involved into the inkjet process.

A simple approach to predict the input signal is to translate the general trapezoidal electrical input signal, that serves as the input to the piezoelectric actuator, to a roughly sinusoidal oscillation with a decaying amplitude (Hoath 2016).

In Figure 2.18, an example of a possible velocity waveform is presented which results from a trapezoidal voltage signal to the piezoelectric actuator. The initial pull-phase leads to an inwards flow of the ink. The following push-phase produces the droplet by accelerating the flow out of the nozzle. The last pull-phase results in the pinch-off of the liquid, after which the driving waveform has no longer any influence on the ejected droplet. Following waveform oscillations can, therefore, be neglected within the simulation of a single droplet (Hoath 2016). They play, however, a role if a series of multiple droplets is to be simulated, since remaining meniscus oscillations can influence the formation of following droplets.
Deviations from this simplification require either specific measurements or advanced methods that include the analytical or numerical simulation of the waveform propagation through the printhead. These methods need a great understanding of the physical properties and dimensions within the printhead itself. Methods that have been used in other researches include FEM analysis, Narrow-Channel models, or Lumped-Element models. The FEM method allows for a simple numerical investigation of the actuation waveform, but has a high demand on computational power. The analytical methods allow an approximation of the inlet condition within seconds but need more time in the calibration process. In most cases, these analytical models also involve FEM simulations to derive all the needed parameters. For the potential use in future investigations, a short overview over these methods will be presented in the appendix.

2.3.2 Fluid Simulation Models

When simulating a droplet formation process, a multiphase simulation has to be considered. These simulation models include multiple phases, that interact with

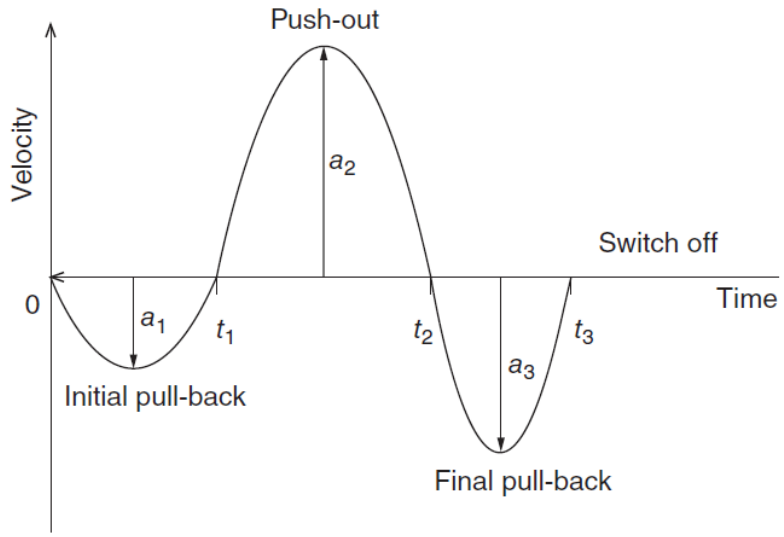

Figure 2.18: Simple waveform approximation. Reprinted from (Hoath 2016) with permission from John Wiley and Sons.

each other. The resolving of the surface between two different phases is thereby especially crucial.
Many different methods are commonly used for this task, with the most popular being the Volume of Fluid (VOF) and the Level Set Methods (Hoath 2016). The VOF method is an Eulerian-based interface tracking technique that defines the free surface through a mass fraction in each cell. The Level Set method specifies an interface contour and a smoothly differentiable field to describe the free surface. For this thesis, a VOF method is chosen since it is the prominent model to use for two immiscible fluids within the chosen software (Siemens 2024).

Numerical Modelling Approach

The goal of this thesis is to numerically recreate the droplet formation process from a commercial inkjet printhead. The software Star-CCM+ (Version 18.06.007 with double-precision) is used for the model creation process.

Creating a virtual model that yields meaningful results presents numerous challenges. The complexity of the droplet formation process coupled with the dimensions of the printhead itself, bring many difficulties when describing and trying to recreate the process numerically. Experimental investigations require expensive equipment and many phenomena, like the flow within the printhead, are inaccessible for measurements. It is therefore important to specify clear objectives before embarking on the computational investigation of the process and consider the limitations: What experiments can be performed? What simplifications can be made? How can the model be validated? What are the desired outcomes of the simulation?

Within this chapter the numerical model is described, beginning with the assumptions that have been made to simplify the process. Afterwards, the used methods and governing equations are presented and a first validation approach is conducted.

3.1 Assumptions

To simplify the numerical approach, several assumptions can be made about the process to reduce computational cost. Some assumptions are based on a balance between accuracy, and runtime and others are based on the inaccessibility of more accurate descriptions.

The air properties are set as constant for all simulations and taken at 15°C. Air density is set as 1.225 kg/m^3 and dynamic viscosity as 1.8E-5 Pas (Tofan et al. 2022).

Within the simulated length and time scale, the effect of gravity can be assumed to be negligible (Wijshoff 2008). This can be justified with the Bond number, which represents the ratio between gravity force and surface tension force (see equation 3.1). Given the small scale of the process, the Bond number is always smaller than 10^{-4}, making surface tension the dominant force in the droplet formation process. The timescale of the jetting itself is in the region of $0.1\ ms$, making the acceleration of the droplet due to gravity also negligible.

$$Bo = \frac{\Delta \rho g r^2}{\sigma} \tag{3.1}$$

The speed of sound in ink is around 1250 m/s but varies depending on the ink formulation (Wijshoff 2008). The speed of sound has an important influence on the acoustic wave propagation within the ink channel (Hoath 2016). For the droplet formation itself, the dimensions are, however, small enough to neglect the speed of sound according to Wijshoff (2008) and consider the fluid to be incompressible.

The process is considered to be at a constant temperature. Therefore, no energy equations are included in the simulation itself.

All liquids and jetting speeds that are considered in the operating regime of different inks (Figure 2.7) are below a Reynolds number of Re=200. The flow is, therefore, assumed to be laminar for all conducted simulations.

The prediction of the actuation waveform plays a special role in the successful simulation of the jetting process. As stated in Chapter 2.3.1, there are multiple possible methods throughout literature that can be used to describe the coupling between acoustical and fluidic domains. Initially, a simple sinusoidal waveform is used, based on the chosen validation case. In the later part of this thesis, a more advanced method for a waveform approximation is created in combination with experimental data.

3.2 Numerical Model

As stated previously, there are many different possible options to select a fitting numerical model for the simulation of multiphase flow. For simulations in this project, the VOF model was selected since it is designed to capture the interface between several immiscible fluids. Resolving the free surface is essential to capture the droplet formation process.

3.2.1 Volume of Fluid

The Volume of Fluid method (VOF) is an Eularian-based interface tracking technique and is featured in the selected software (Siemens 2024). This method allows the simulation of fluid dynamics of two immiscible fluids with a fluid-fluid interface (free surface). A fixed mesh is used, and the free surface moves through the mesh. At each point in space, a volume fraction α_i is defined (see Figure 3.1). If the volume fraction is 1, the point is occupied by a liquid, and if it is 0, it is not. The volume fraction along the free surface indicates how much of the cell is occupied by liquid. The material properties in a cell with $0 < \alpha_i < 1$ depend on the material properties of the constituent phases. The fluid within these cells is treated as a mixture:

$$\rho = \Sigma_i \rho_i \alpha_i \tag{3.2}$$

$$\eta = \Sigma_i \eta_i \alpha_i \tag{3.3}$$

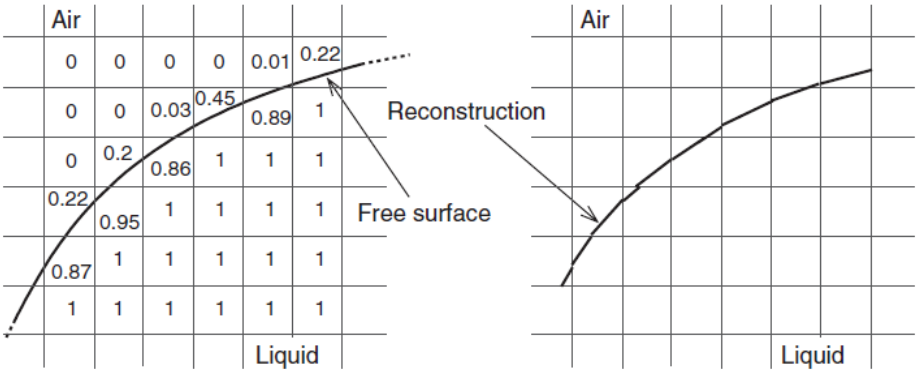

Figure 3.1: Volume of Fluid representation of the free surface in a fixed mesh. Reprinted from (Hoath 2016) with permission from John Wiley and Sons.

The distribution of phase i is driven by the phase mass conservation equation:

$$\frac{\partial}{\partial t}\int_V \alpha_i dV + \oint_A \alpha_i \mathbf{v}\cdot d\mathbf{a} = \int_V \left(S_{\alpha_i} - \frac{\alpha_i}{\rho_i}\frac{D\rho_i}{Dt}\right) dV - \int_V \frac{1}{\rho_i}\nabla\cdot(\alpha_i\rho_i\mathbf{v}_{d,i})\, dV \quad (3.4)$$

where $\mathbf{a}$ is the surface area vector, $\mathbf{v}$ is the mixture (mass-average) velocity, $\mathbf{v}_{d,i}$ is the diffusion velocity, S_{α_i} is a source term of phase i, and $\frac{D\rho_i}{Dt}$ is the material derivation of the phase density ρ_i. For a flow with two phases, the equation is only solved for the primary phase, which in this case is the liquid.

To properly simulate two immiscible phases, a sharp interface between the two phases is essential. Star-CCM+ uses the High-Resolution Interface Capturing (HRIC) scheme for this purpose. The HRIC scheme is based on the normalized variable diagram (NVD). Within this method, every face value ξ_f for each cell is calculated as:

$$\xi_f = F(\theta)\xi_f^{Compressive} + (1 - F(\theta))\xi_f^{Blend} \quad (3.5)$$

where $\xi_f^{Compressive}$ is the normalized compressive face value, ξ_f^{Blend} is the normalized blending face value, and $F(\theta)$ is the blending function. This function is depending on the angle between the normal to the interface n_i and the cell-face surface vector a_f (see Figure 3.2).
The compressive and blended face values depend on the normalized cell values for each cell, which are computed as:

$$\xi_C = \frac{\alpha_C - \alpha_U}{\alpha_D - \alpha_U} \quad (3.6)$$

for a central cell, upwind of the acceptor cell, where α_U is the upwind nodal variable value, and α_D is the downwind value. The HRIC can implement an additional smoothing function called HRIC gradient smoothing. This allows for a less mesh-dependant extrapolation of the upwind value α_U and, therefore, a more stable behaviour of the HRIC scheme for anisotropic meshes. The extrapolation of α_U is defined as:

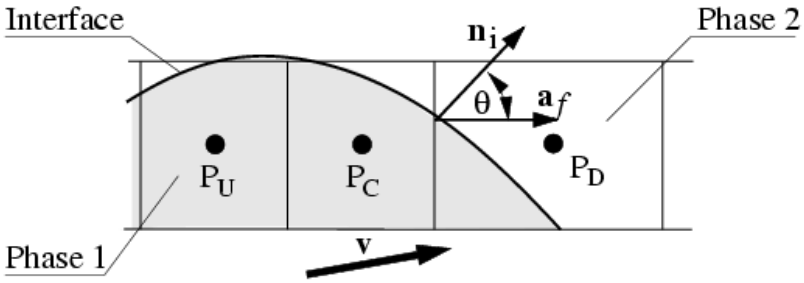

Figure 3.2: Representation of the interface reconstruction between two fluids, based on the HRIC scheme (Siemens 2024).

$$\alpha_U = \alpha_{f,D} - 2d\mathbf{x} \cdot \nabla\alpha_{f,U} \tag{3.7}$$

where $\nabla\alpha_{f,U}$ is the volume fraction gradient, which is replaced by a smoothed version.
Recent versions of the VOF model include the surface tension via the 'continuum surface force' (CSF) approach. This approach includes surface tension effects as a source term in the Navier-Stokes equations. This source term is defined within Star-CCM+ as:

$$f_\gamma = f_{\gamma,n} + f_{\gamma,t} = \gamma\kappa\mathbf{n} + \frac{\partial\gamma}{\partial t}\mathbf{t} \tag{3.8}$$

where $\mathbf{n}$ is the normal vector to the free surface, $\mathbf{t}$ is the vector tangential to the free surface, γ is the surface tension coefficient, and κ is the mean curvature of the free surface.

To enhance the stability of the surface tension simulation on moving flows, a semi-implicit surface tension approach is recommended, especially in cases where surface tension is one of the dominant physical mechanisms. This replacement leads to the addition of a temporal linearisation, which is defined as:

$$(\kappa\mathbf{n})^{n+1} \approx \underline{\Delta}\mathbf{x}^n + \Delta t\underline{\Delta}\mathbf{v}^{n+1} \tag{3.9}$$

where $\underline{\Delta}$ is the Laplace-Beltrami operator, $\mathbf{x}$ is the identity mapping the free surface, and $\mathbf{v}$ is the velocity vector.

3.2.2 Governing Equations

The other governing equations include mass conservation and momentum equation. Both are influenced by the selected VOF model and presented in the following section.
The total mass conservation for all phases is given by:

$$\frac{\partial}{\partial t}\left(\int_V \rho dV\right) + \oint_A \rho\mathbf{v} \cdot d\mathbf{a} = \int_V S dV \tag{3.10}$$

where S is the mass source term, which is defined as:

$$S = \sum_i S_{\alpha_i} \cdot \rho_i \tag{3.11}$$

This total mass conservation is related to the phase mass conversion (Eq. 3.4) and includes the fluid mixture through the density.
The momentum equation is defined as:

$$\frac{\partial}{\partial t}\left(\int_V \rho \mathbf{v} dV\right) + \oint_A \rho \mathbf{v} \otimes \mathbf{v} \cdot d\mathbf{a} = -\oint_A p\mathbf{I} \cdot d\mathbf{a} + \oint_A \mathbf{T} \cdot d\mathbf{a} + \int_V \mathbf{f}_b dV - \sum_i \int_A \alpha_i \rho_i \mathbf{v}_{d,i} \otimes \mathbf{v}_{d,i} \cdot d\mathbf{a} \tag{3.12}$$

where p is the pressure, I is the unity tensor, T is the stress tensor and f_b is the vector of body forces.

3.3 Computational Domain

During all simulations conducted in this research, the same axisymmetric computational domain has been chosen. Only slight differences in the dimensions and the nozzle shape have been implemented depending on the compared experimental data. In the following, the domain is presented, as well as boundary conditions and first simulations.

The simulation domain of the stand-alone jetting model includes parts of the pressure channel, the nozzle, and an air section (see Figure 3.3). The pressure channel has a radius of r_P and a length of l_P. The nozzle is formed into the nozzle plate with a thickness of l_N and has a nozzle radius of r_N. The air section has a length of l_A and a radius of r_A. The dimensions of the air section must be sufficiently large to prevent any backflow and boundary condition effects to affect the droplet simulation. Moreover, the air domain should be large enough to capture the crucial aspects of droplet ejection. Both the pressure channel and nozzle are filled with liquid at the start of each simulation.

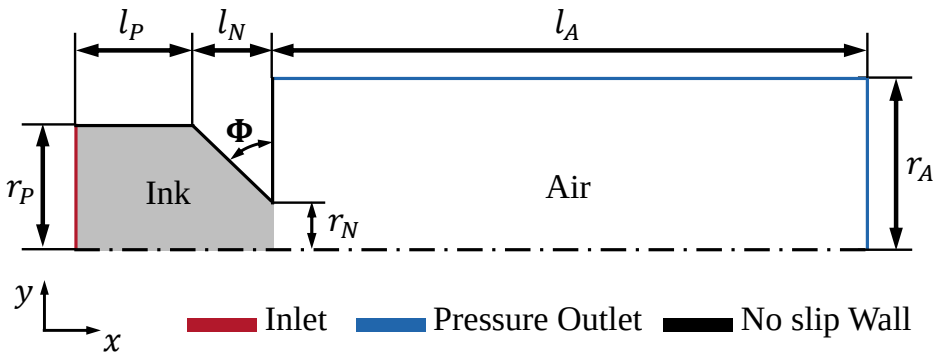

Figure 3.3: Generalized domain of the axisymmetric model.

With the described domain, the first simulations can be conducted. To investigate the mesh dependency and numerical model parameters, a simple velocity waveform is used on the inlet (Figure 3.4). The waveform is based on the simplifications in Chapter 2.3.1 (see Figure 2.18). A pull time of 1 μs and a push time of 2 μs was chosen. The printhead in the simulation has a nozzle diameter of 32 μm. For the initial simulation a general time-step of 2e-7 seconds was selected with an adaptive time-step based on the CFL number of the free surface. The CFL limit was set at a maximum condition value of 0.4 and the implicit solver SIMPLE was selected. The arbitrary fluid parameters are $\rho = 1050\ kg/m^3$, $\eta = 7\ cP$, and $\gamma = 72\ mN/m$, resulting in a Ohnesorge number of 0.201. With this value, a satellite-free droplet formation should be achievable, according to Figure 2.7. As seen in Figure 3.5, a droplet formation can be simulated with the initial parameters and selected models. The Figure shows the development of a single droplet in 2 μs steps. Similar plots, as shown in Figure 3.5, will be used throughout the thesis and always represent sequential images of the same simulation at defined time-steps, if not otherwise specified.

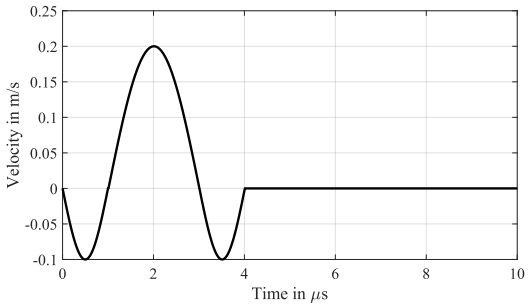

Figure 3.4: Simple arbitrary velocity waveform based on Hoath (2016).

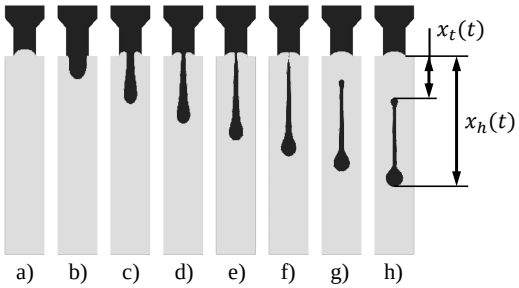

Figure 3.5: Droplet simulation results at 1, 3, .., 15 μs after actuation for an arbitrary fluid.

To extract data from the simulation and evaluate the results, several post-processing steps are implemented. Essential values to compare between experiments and simulations are the droplet position and velocity. The position of the head droplet is measured from the tip of the droplet to the nozzle plate ($x_h(t)$), see Figure 3.5. The velocity of the droplet $\dot{x}_h(t)$) is defined as the derivative of $x_h(t)$ in the jetting direction. By extracting this data during the simulation, a visualisation of the droplet movement can be derived (see Figure 3.6). The tail velocity and position can also be defined to investigate the tail speed and visualise the contraction of the tail into the main droplet. The presented Figure shows a graphical overlay of the droplet simulation at the given time-steps. In Figure 3.7 the velocities of the head and tail droplet are presented, showing the higher tail velocity that leads to the catch-up of the ligament.

The results show a satellite-free droplet ejection with a final droplet speed around 7 m/s with a maximum jetting speed of 22 m/s. Every stage of the droplet formation is represented in the simulation and according to the schematic presented in Figure 2.8. After a successful initial simulation of a droplet formation, further investigations

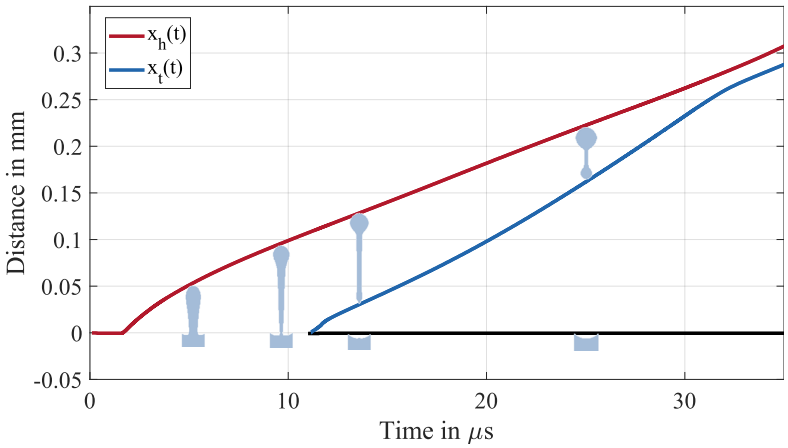

Figure 3.6: Distance of the head droplet $x_h(t)$ and the tail droplet $x_t(t)$ from the nozzle plate during the actuation.

regarding mesh sensitivity and parameter effects can be conducted, as well as first validation attempts.

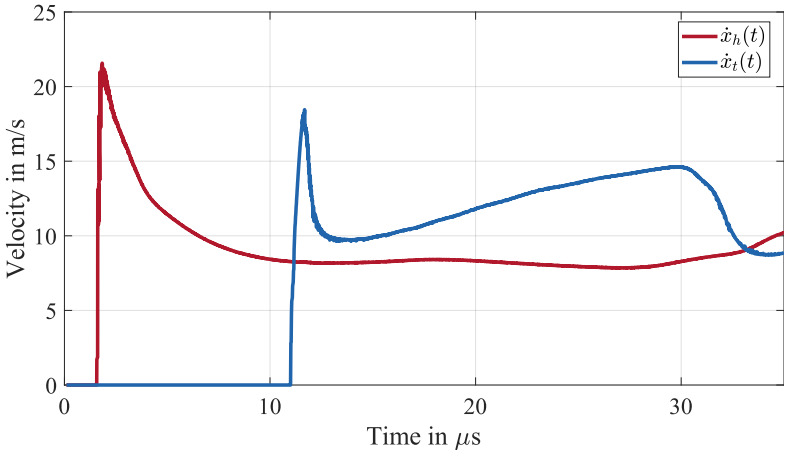

Figure 3.7: Velocity of the head droplet $\dot{x}_h(t)$ and the tail droplet $\dot{x}_t(t)$ from the nozzle plate during the actuation.

3.4 Mesh Sensitivity

The investigation of different mesh types and mesh resolutions is essential to find a compromise between accuracy and simulation time. Both structured and unstructured meshes can be considered and provide different benefits and disadvantages. In order to evaluate the optimal mesh type and resolution, several simulations are performed. The aim is to achieve a reasonable mesh-convergence regarding final velocity and tail breakup.
Some considerations can be made when evaluating the mesh resolution. A general guideline is to aim for 10 grid cells for an accurate simulation of the spatial details

(Wijshoff 2008). For the droplet formation the smallest lengthscale is the viscous length scale L_η:

$$L_\eta = \frac{\eta^2}{\rho\gamma} \tag{3.13}$$

This length scale varies depending on the used liquid but is considered to be around 1-5 μm with typical values for the fluid properties. This would result in a minimal element size of 0.1-0.5 μm to resolve all flow characteristics. Similar assumptions can be made when considering the secondary tail formation during the jetting process as the smallest desired spatial detail. A secondary tail is observed to have a dimension on the order of 1 μm (Fraters et al. 2020). An element size of 0.1 μm can therefore be considered as sufficient, but also computationally expensive with several hundred elements across the nozzle diameter. The following sections evaluate the effect of lower mesh resolution on the results. All simulations use the inlet waveform presented in Figure 3.4.

3.4.1 Structured Mesh

First, a structured mesh was investigated. The "Trimmed" mesher within Star-CCM+ was used to generate the mesh, which is displayed in Figure 3.8 with a minimal element size of 0.8 μm. The minimal element size was set within a refinement zone to increase the resolution of the droplet formation process while simultaneously reducing the computational cost by employing a coarser mesh further away from the flow. The minimal element size variation was chosen with the values 1.6 μm, 0.8 μm, 0.4 μm, and 0.266 μm. The refinement zones are marked in the top half of the scene in Figure 3.8 and were chosen to both capture the meniscus motion within the nozzle and the droplet formation. As a base element size in the coarse zones, a value of 5 μm was chosen. A slow growth rate was selected to create a smooth transition between the refinement zone and the coarser mesh area. Different metrics were used to check the generated mesh quality (see Table 3.1). These are the percentage of elements with a volume change below 0.1, the face validity, and the maximum boundary skewness angle. Elements with a volume change below 0.01 are considered critical, as well as elements with a maximum boundary skewness angle above 85 degrees (Siemens 2024).

Table 3.1: Mesh quality statistics for the different structured meshes.

Smallest Element Size in μm	Number of Cells	Volume Change < 0.1 in %	Maximum Boundary Skewness Angle in deg.	Face Validity in %
1.6	36183	0.028	31	100
0.8	128850	0.015	19.2	100
0.4	487714	0.008	21.8	100
0.266	1883613	0.004	38.7	100

The air domain was scaled to a sufficient size to prevent any boundary effects from impacting the droplet formation. This was tested in multiple simulations by evaluating the pressure and velocity fields within the domain.

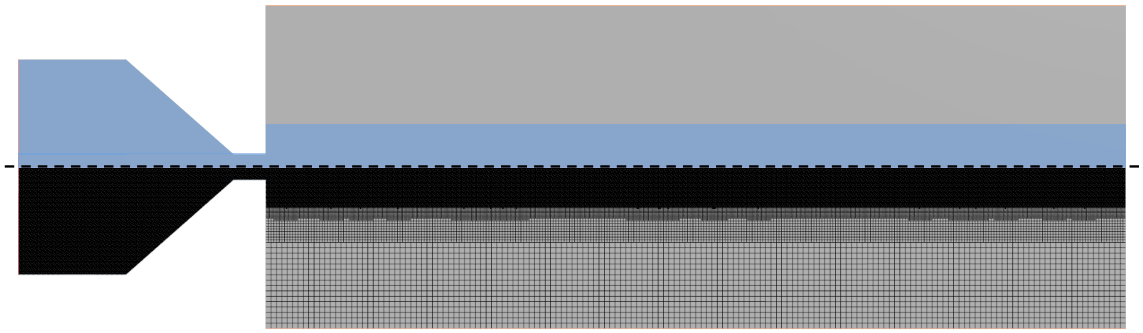

Figure 3.8: Structured Mesh of the axisymmetric model. Top: Visualisation of the refinement zone. Bottom: Example Mesh with the smallest element size of 0.8 μm.

The results of the simulation with different mesh sizes are shown in Figure 3.9. The scenes display the droplet at 5, 10, 15 and 20 μs, respectively. At the lowest resolution (a), a blurry free surface can be observed, and the tail clearly behaves differently compared to the higher resolutions. With an increase in mesh resolution, the free surface becomes sharper.

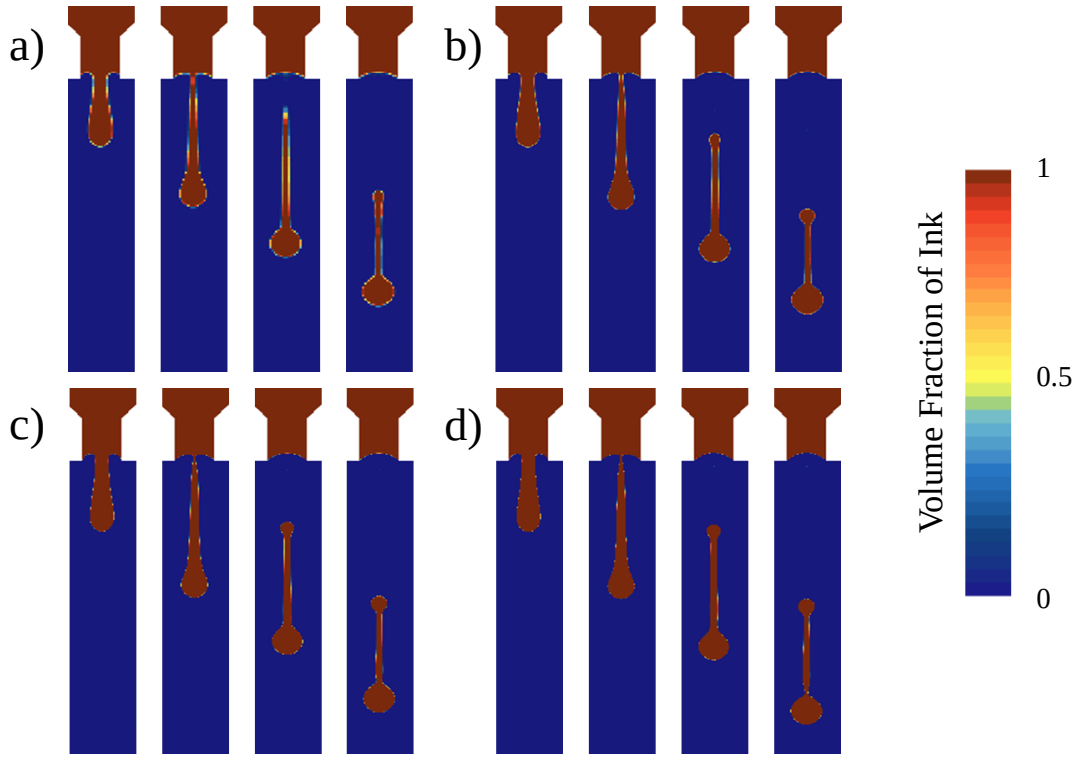

Figure 3.9: Simulation of the droplet formation at different mesh resolutions with a structured mesh at 5, 10, 15, and 20 μs, respectively. Smallest element size: a) 1.6 μm b) 0.8 μm c) 0.4 μm d) 0.266 μm.

However, a different behaviour in the droplet speed and, therefore, position can be observed in the simulations. Figure 3.10 and 3.11 show the clear inconsistency of the droplet behaviour with different mesh resolutions. A lower mesh size leads to an increase in the final droplet velocity. A mesh-convergence could not be reached with regard to these parameters.

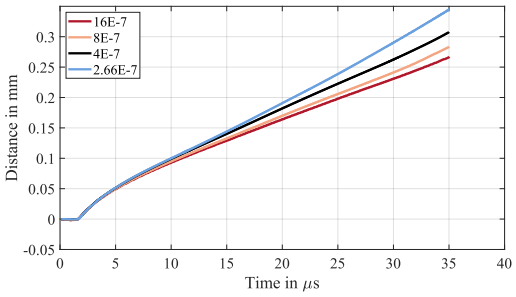

Figure 3.10: Distance (x_h) of the head droplet over time at different mesh resolutions with a structured mesh.

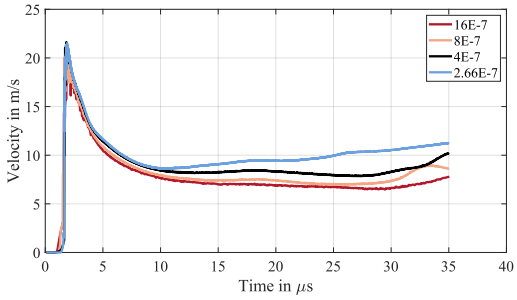

Figure 3.11: Velocity ($\dot{x}_h$) of the head droplet over time at different mesh resolutions with a structured mesh.

3.4.2 Unstructured Mesh

Another option to generate a mesh for the simulation is to use unstructured mesh types. For this case, a polyhedral mesher was chosen. An example mesh with the smallest element size of 0.8 μm is shown in Figure 3.12. The same refinement zones and base mesh sizes as in the structured mesh were chosen to allow a comparison between the two different mesh types. The boundary region was again examined for any influence on the simulation itself, and the quality of the mesh was checked (see Table 3.2). Again, a minimum element size in the refinement zones of 1.6, 0.8, 0.4, and 0.266 μm was chosen.

Table 3.2: Mesh quality statistics for the different polyhedral meshes.

Smallest Element Size in μm	Number of Cells	Volume Change < 0.1 in %	Maximum Boundary Skewness Angle in deg.	Face Validity in %
1.6	44066	0.703	89	100
0.8	167543	0.347	69	100
0.4	660514	0.171	62	100
0.266	1438979	0.104	64	100

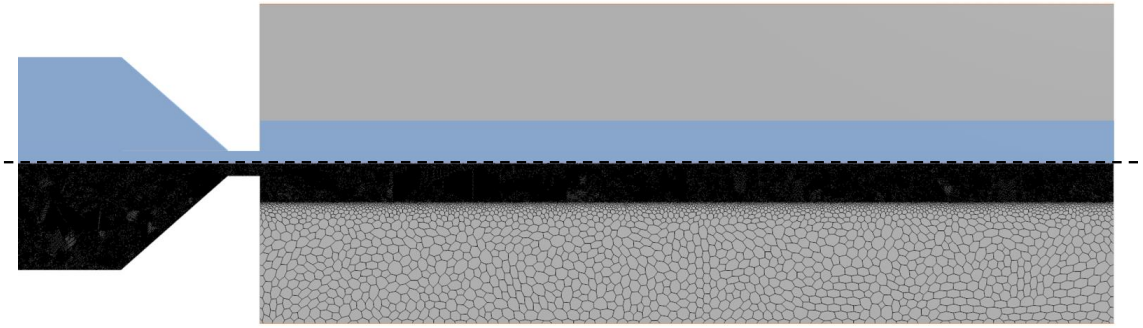

Figure 3.12: Unstructured Mesh of the axisymmetric model. Top: Visualisation of the refinement zone. Bottom: Example Mesh with a smallest element size of 0.8 μm.

The results of the simulations are presented in Figure 3.13, which shows the volume fraction of liquid within the domain. A clear difference can be observed in the tail breakup and the free surface interface between mesh (a) and the rest of the simulations. Mesh (c) and (d) show a sharp free surface interface and a similar droplet behaviour.

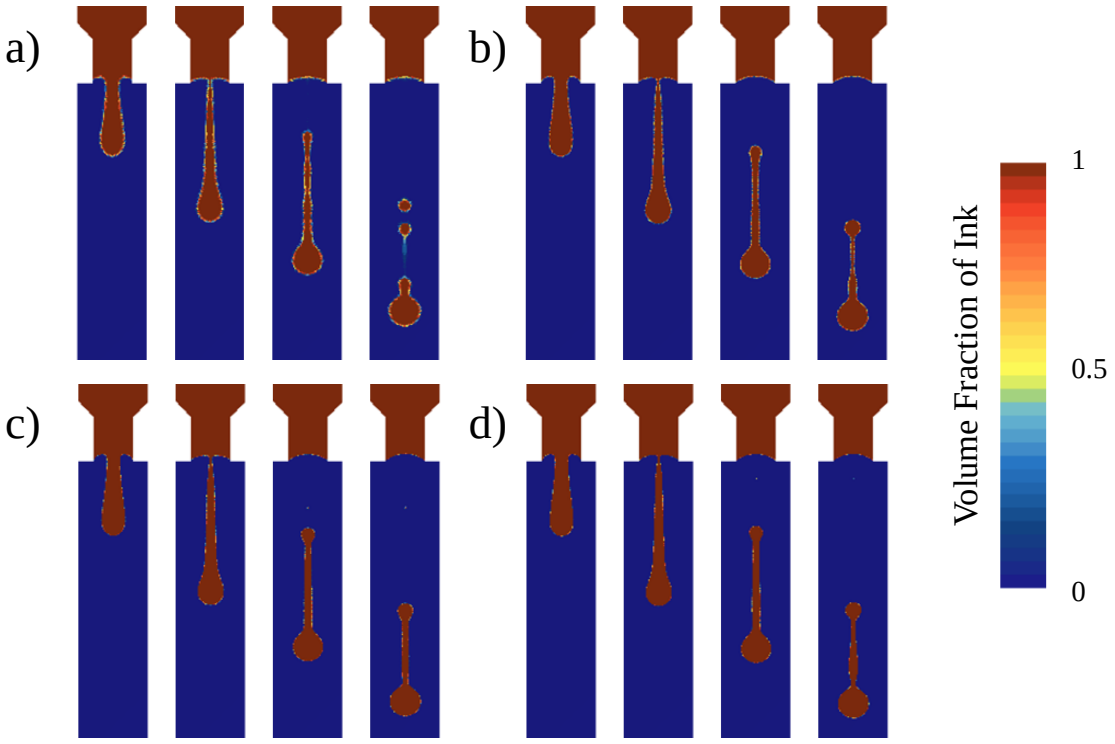

Figure 3.13: Simulation of the droplet formation at different mesh resolutions with a unstructured mesh at 5, 10, 15 and 20 μs, respectively. Smallest element size: a) 1.6 μm b) 0.8 μm c) 0.4 μm d) 0.266 μm.

When comparing the position (Figure 3.14) and the velocity (Figure 3.15), a more stable outcome can be observed than for the structured mesh. The droplet movement is more consistent between different mesh resolutions and does not significantly change with a finer mesh. Also, the velocities show a consistent trend with different mesh resolutions. The noise in the velocity plot is due to the unstructured mesh and a higher inconsistency of the position of the tip of the droplet when moving through the mesh.

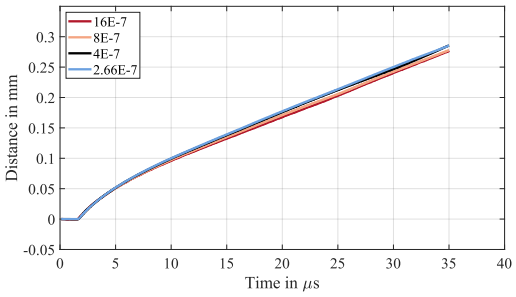

Figure 3.14: Distance (x_h) of the head droplet over time at different mesh resolutions with a unstructured mesh.

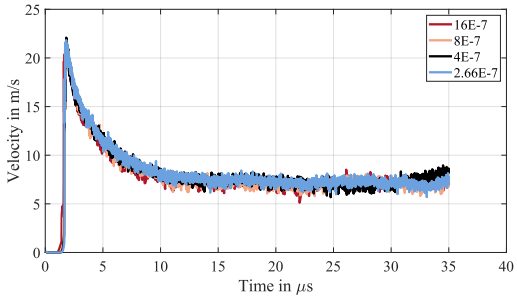

Figure 3.15: Velocity ($\dot{x}_h$) of the head droplet over time at different mesh resolutions with a unstructured mesh.

3.4.3 Mesh Selection

As seen in previous studies (see Chapter 2.3), finding a mesh-convergence of the solution can be a challenge. This problem has been observed in this thesis and shown in the previous sections. Small fluctuations in the mesh lead to changes in the tail formation and breakup, which is largely influenced by instabilities. Choosing a fitting mesh is therefore not a trivial task in this application.

A comparison between the average velocities of the droplets after pinch-off (Figure 3.16) shows that the polyhedral meshes are more stable regarding the droplet velocity. The structured mesh shows an exponential increase in droplet velocity with a reduction in element size. Regarding the needed simulation time, the polyhedral mesh needs, however, more computational power, which can be seen in Figure 3.17.

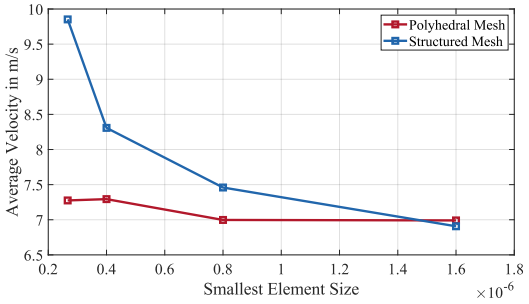

Figure 3.16: Comparison of the average droplet velocity between 20 and 35 μs for structured and unstructured meshes with different resolutions.

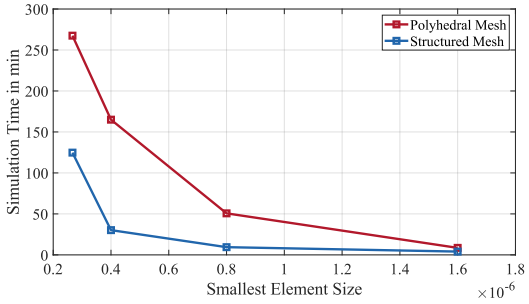

Figure 3.17: Comparison of the simulation time for different resolutions of structured and unstructured meshes.

The better stability of the polyhedral mesh regarding droplet velocity leads to the selection of this mesh type. Since a mesh resolution of 0.4 μm showed a sharp free surface interface with a stable droplet formation, this mesh resolution was selected for further investigations. This builds a compromise between simulation time and resolution since a further increase in mesh resolution does not provide any apparent benefits at this point. It can moreover be concluded that the selection of a fixed mesh is essential, and mesh changes during different investigations should be avoided.

3.5 Validation

For the initial validation of the numerical model, a comparison with experimental investigations of Wijshoff (2008) was conducted. In his work, Wijshoff describes the inkjet droplet physics in detail. He conducted several experiments and provides details about both numerical as well as experimental approaches. For the coupling between acoustic and fluid dynamic domains, he used the narrow channel theory method.

The experiment used for the validation of the model shows the basic droplet and tail formation of a single drop ejection. The printhead has a nozzle diameter of 32 μm in a 50 μm electroformed nickel nozzle plate. A pull-push action or fill-before-fire action was performed by Wijshoff with an initial negative pressure wave. The chosen fluid has a density of $\rho = 1000\ kg/m^3$, a viscosity of $\eta = 0.01\ Pas$, and a surface tension of $\gamma = 0.03\ N/m$. For a numerical simulation of the process, a pressure wave is used as an inlet condition at the beginning of a 300 μm long connection channel in front of the nozzle plate. In his work, he uses a direct connection between his narrow channel model and the stand-alone droplet formation model. The concrete pressure input is not provided by the paper. The pressure wave that is used for the validation in this thesis is shown in Figure 3.18 and taken from investigations by Dannenberg (2022), who validates a numerical model with the same experimental case. For the nozzle-ink interaction a contact angle of 20 degrees is defined, based on the investigations of Wijshoff.

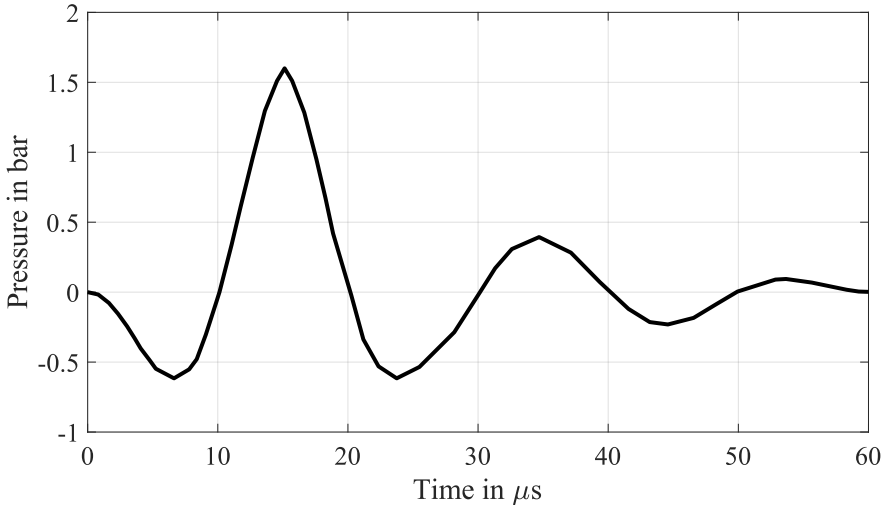

Figure 3.18: Time dependent pressure boundary condition. Based on Wijshoff (2008).

The experimental results of Wijshoff (2008) and the numerical simulation from this thesis are presented in Figure 3.19. The visualization showcases droplets captured in sequential intervals of 10 μs, starting from 10 μs. For the numerical simulations, all assumptions from Section 3.1 were applied. A grid size of 0.4 μm was chosen for the simulation, based on the previous mesh sensitivity study.

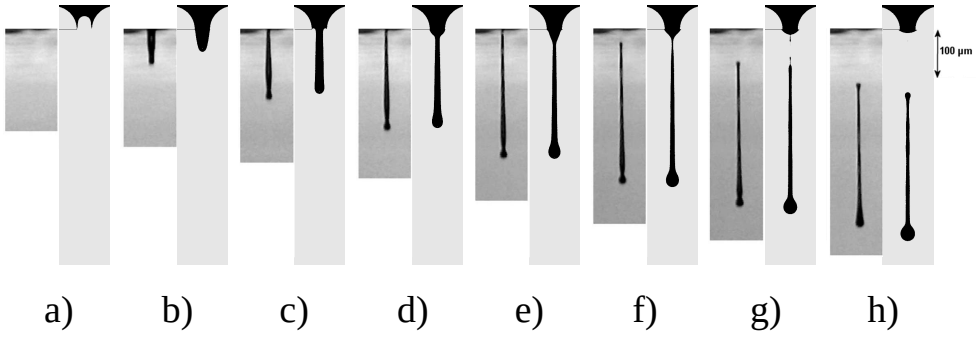

Figure 3.19: Comparison between experimental droplet formation by Wijshoff (2008) and simulated droplet formation at 10, 20, ..., 80 μs after the start of the actuation.

A comparison between experimental and numerical results is presented in Table 3.3. The experimental droplet speed was reported to have an initial maximum meniscus speed of 20 m/s and a final droplet speed of 7 m/s. With the simulation conducted in this report, an initial droplet speed of 19.4 m/s and a final droplet speed of 5 m/s could be achieved. The experimental droplet volume is 32 pl compared to the simulated droplet volume of 33 pl.

Table 3.3: Comparison between selected experimental and numerical results.

Comparison	Droplet Volume in pL	Maximum $\dot{x}_h$ in m/s	Final droplet speed in m/s	Maximum retraction speed in m/s
Experiment (Wijshoff, 2008)	32	20	~7	-7
Simulation	33	19.4	~5	-6

With the simulation, a the time-dependent velocity development can be provided, which also includes information about the retracting meniscus. In Figure 3.20, the velocity profile and the distance to the nozzle plate for the conducted simulation are presented. At the beginning of the simulation, the meniscus retracts with a maximum speed of -6 m/s, compared to the -7 m/s reported by Wijshoff.

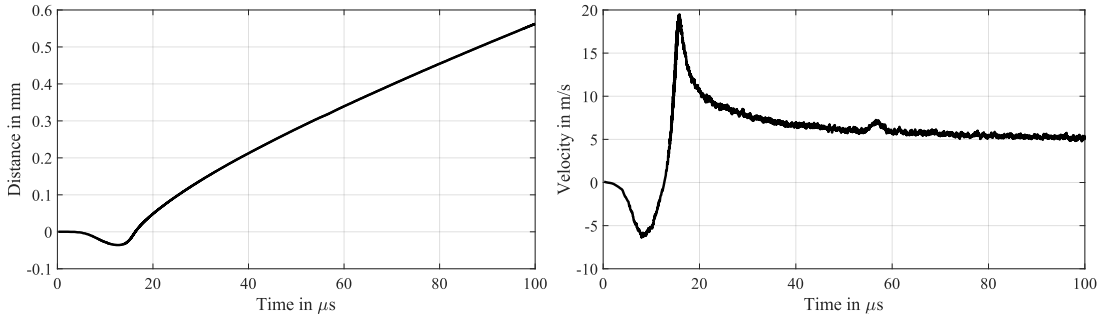

Figure 3.20: Left: Distance (x_h) of the head droplet over time. Right: Velocity ($\dot{x}_h$) of the head droplet over time.

In general, a good agreement between the experimental data provided by Wijshoff (2008) and the numerical model could be achieved. The tail and head droplet

formation shows the same trend as in the experiments. Velocity and droplet volume are close to the experimental values, given the assumptions that have been made, when choosing the inlet pressure. Similar simulation results are achieved by Wijshoff (2008), where the final droplet speed is between 5 and 7 m/s. As stated by him, the maximum velocity is about 2 to 3 times higher than the final drop speed, which can be observed in the simulation. The model is, therefore, seen as accurate enough to conduct first investigations.

3.6 Initial Investigations

With the current model setup, some initial investigations have been conducted. They include post-processing possibilities, model parameters within Star-CCM+, fluid properties and simple waveform variations. With these, an initial model comprehension and first analysis options can be explored before adapting the model to match the characteristics of the actual printhead.

3.6.1 Post-Processing

The post-processing of simulation results is essential to analyse, interpret, and utilise the gained information. Several aspects of the droplet formation process might be of interest to investigate later. Therefore, several post-processing functions are implemented to ease the handling of the simulation results. They are also essential to examine potential boundary influences. An overview of the most important plots is provided within this section.

The pressure and velocity fields are displayed for the entire domain and provide information about boundary influences and the actuation development (see Figure 3.21). The airflow around the droplet can be observed. The domain is also large enough to neglect any boundary condition influences in the air domain. This can be observed with the velocity vector field presented in Figure A.5, in the appendix.

In addition to a comprehensive view of the entire domain, Figure 3.22 offers a specific focus on the droplet tail. This focused observation allows for a detailed analysis of internal flow characteristics, like the breakup dynamics and fluid movement within the tail. The pressure field in plot (a) shows the local pressure increase at the pinch-off zone. The velocity field in plot (b) describes the relative velocity of each cell to a local coordinate system of the head droplet. The velocity is coloured based on the magnitude of each vector and displayed as a line integral convolution. This method allows the observation of fluid movement in the tail relative to the main droplet. In the shown example, two flow separations close to the head droplet can be observed, which suggests a thinning of the tail at this point.

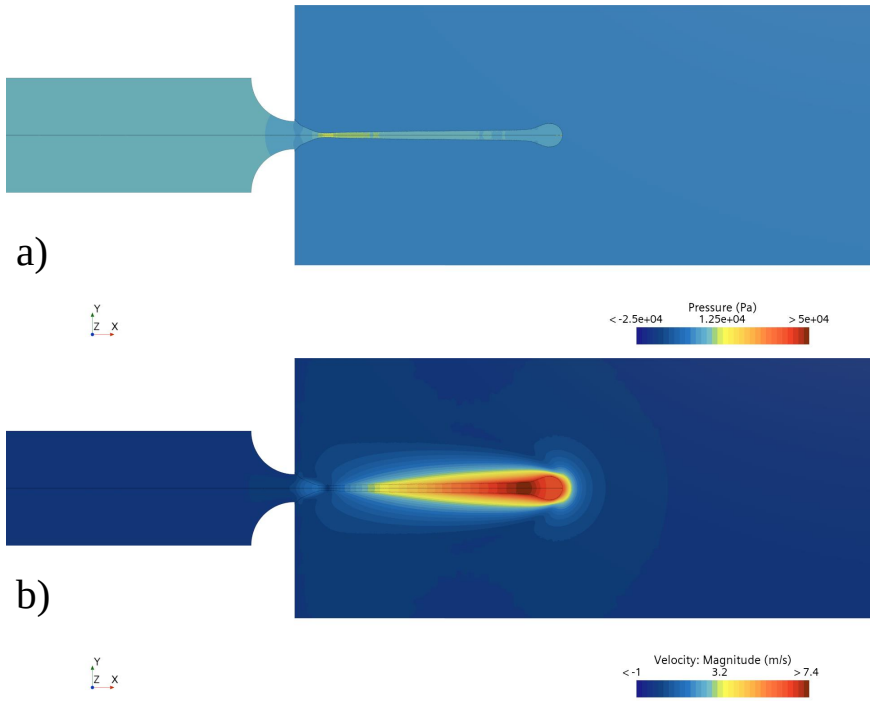

Figure 3.21: Post-processing of the entire flow domain regarding a) pressure b) velocity.

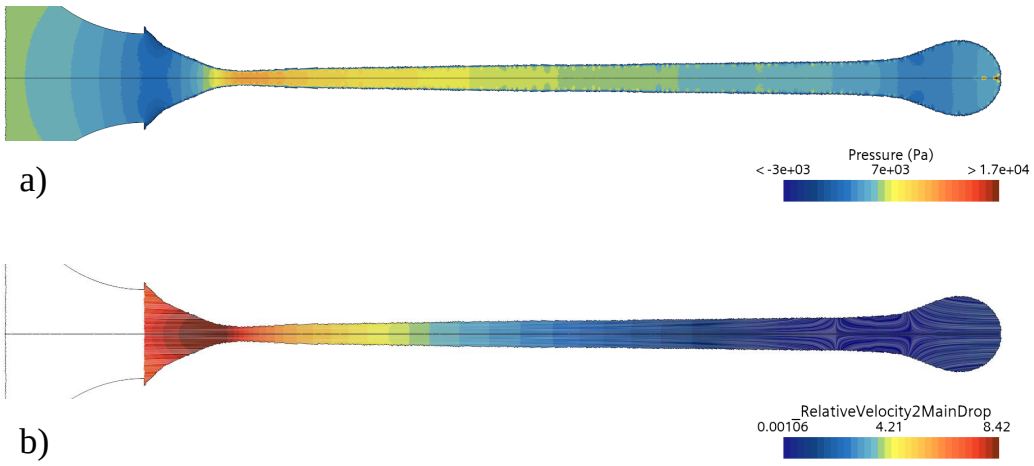

Figure 3.22: Post-processing possibilities of the tail, showing the internal pressure in the tail (a) and the relative velocity of the liquid within the tail (b).

Examining the pinch-off more closely can provide insights into the internal flow characteristics within the ink chamber and during the droplet's separation from the meniscus. Figure 3.23 shows a closer representation of the meniscus and pinch-off zone. The velocity is based on the total velocity, showing the separation of the droplet-based on the global coordinate system. Flow circulation within the nozzle can also be observed.

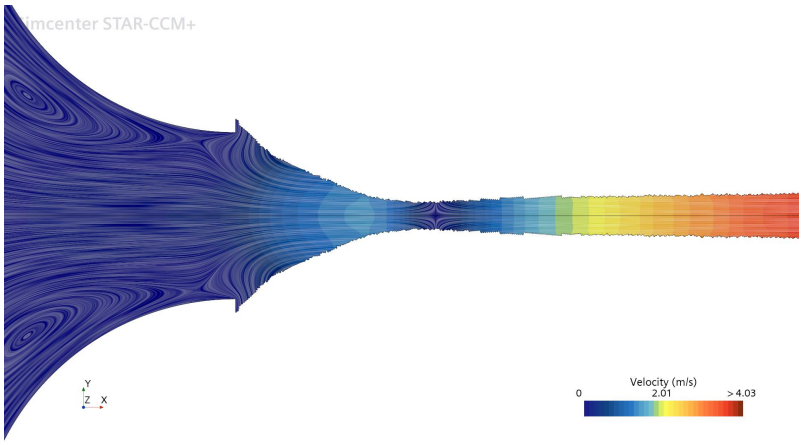

Figure 3.23: Closer look at the velocity vectors at the pinch-off zone, showing the separation of droplet and meniscus as well as internal flow circulations.

Another useful tool for the analysis of each droplet formation is the distance plot introduced in Figure 3.6. Through the addition of the tip and end of each individual satellite droplet within an axisymmetric domain, the separation and potential reconnection of each droplet or satellite droplet can be visualized in a single plot. Figure 3.24 shows an example in which the droplet tail separates into multiple satellite droplets, which recombine with the head droplet after a short time. A graphic representation of the droplet simulation is shown as an overlay to visualize the meaning of each line. From this plot, the velocity, speed, and oscillation of each droplet and satellite can be derived.

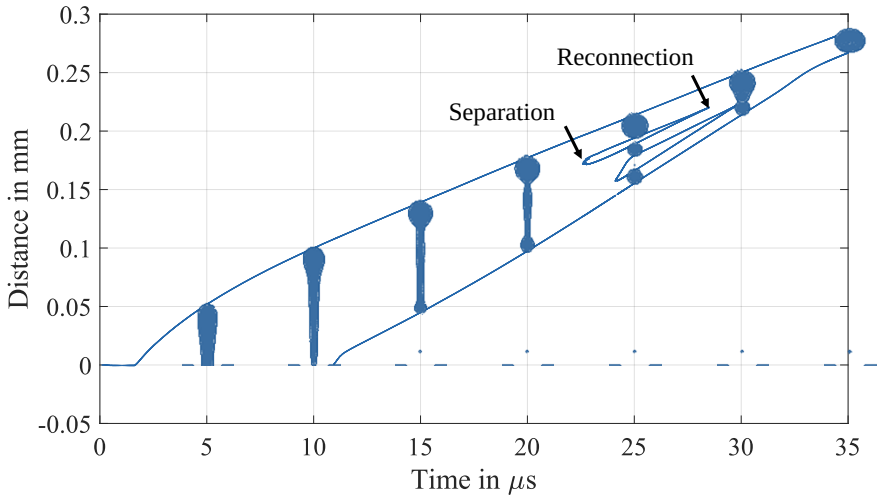

Figure 3.24: Distance of the head droplet, the tail droplet, and any satellites from the nozzle plate during the actuation.

Besides the velocities, pressure fields and position of the different droplets, a special importance lays also on the volume of the produced droplet. For the calculation of volume within the axisymmetric model, the blob detection model of Star-CCM+,

in combination with separate derived parts for each droplet, is utilized. The volume can be calculated by:

$$V_{droplet,total} = 2\pi \Sigma_i V_{doplet,i} \tag{3.14}$$

where $V_{doplet,i}$ is the volume of every cell i belonging to the droplet threshold. The equation results from the fact that Star-CCM+ calculates the volume of an element within the axisymmetric model as a slice of one radiant based on the symmetry axis (Siemens 2024).

The displayed post-processing methods are used for individual investigations throughout the analysis process and provide the possibility for a quick assessment of the gained simulation results.

3.6.2 Model Parameters

When implementing the VOF model, several possible settings are available to adjust the behaviour and accuracy of the results (Siemens 2024). Those include solver settings, VOF options, and the order of different discretization schemes. For the initial simulations, suggested settings from previous projects and current support cases are chosen. These include the use of an implicit multistep scheme for the VOF solver and no artificial gradient smoothing. The selection is based on the requirement of a sharp free surface interface. The effect of different settings is nevertheless briefly investigated in this section. Since there is a significant variety of different model settings and no benchmark case is available, only a short selection of model parameters will be presented. A deeper investigation regarding the effect of different options is part of future investigations.

Several possible settings of the VOF solver are available and could be considered for the simulation. The VOF model allows for a 1st-order or 2nd-order face density reconstruction. The solver of the VOF model includes different solution strategies, like a single-step approach and an explicit or implicit multistep approach. These multistep approaches take over the temporal discretization for the volume fraction transport equation by dividing every physical time-step into smaller sections for the VOF solver. This methodology is supposed to keep the interface between the phases sharp throughout the simulation.

Within the VOF model, the HRIC method is used to maintain a sharp interface between the two phases and for the spatial discretization. The HRIC method allows for additional gradient smoothing to reduce spurious oscillations that can appear in the volume fraction field.

For the time discretization first order and second order schemes are available, which require a target CFL number of <0.7 and <0.5, respectively. Increasing the temporal discretization to a second-order scheme can improve the accuracy of the model, by enhancing the resolution of temporal dynamics and reducing numerical errors associated with time-stepping. Especially in fast-paced dynamics, this can help to achieve better results. However, when using a second-order time discretization, a

VOF single-step solver has to be used.

Choosing the right settings proves to be challenging, as different effects and trade-offs have to be considered. The different options have, therefore, been briefly investigated by changing the model settings and comparing the results. As a comparison case, the previously conducted validation study is chosen with both first-order face density reconstruction and time discretization. In Figure 3.25 the different droplet simulations at a time-step of 100 μs are displayed with just the listed setting change. The base case uses first-order schemes. It can be noted, that there is no significant change between different orders of discretization schemes regarding the droplet formation. Only slight changes in the position of the second-order time scheme are noticeable. The main effect is accomplished by utilising the HRIC gradient smoothing.

Figure 3.25: Comparison of the effect of different model parameters on the simulation results. A base case was chosen with first order discretization schemes and compared to both second order spatial and temporal schemes. Additionally a comparison with HRIC gradient smoothing was conducted, using first order discretization schemes.

The time step size for all cases throughout the simulation is very similar and is in average around 9.26 ns. A graphical comparison can be found in the appendix (see Figure A.4). All simulations reach a sharp interface resolution of only one cell. Exemplary, the free surface for the first order time scheme is shown in Figure 3.26. Within this first investigation, no significant effect on the simulation results could be observed. Due to the lack of precise data for the inlet boundary condition and since neither of the results match the experimental outcome better than the others, it is currently impossible to determine which model setting is most suitable for the application and yields the most accurate results. At the given stage, the following model parameters are chosen based on previous simulations: first-order time discretization, an implicit multistep solver for the VOF model, and no HRIC gradient smoothing. Together with experimental data, a more precise selection can be conducted later on.

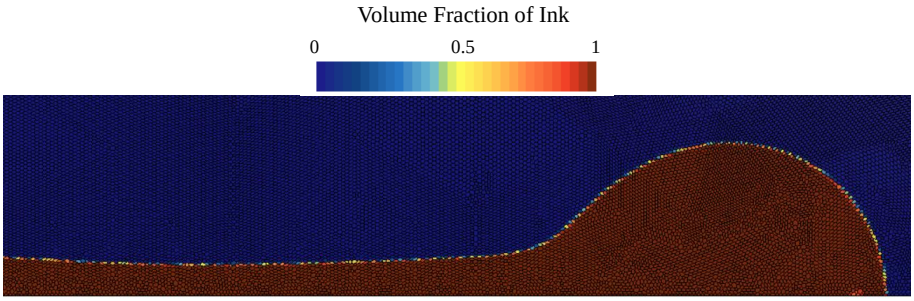

Figure 3.26: Close-up of the free surface for a single droplet.

3.6.3 Fluid Properties

The ink properties play a crucial role in the droplet formation process. One of the possible analyses that can be conducted with a numerical model is the effect of different mixtures and properties on the droplet behaviour. As stated previously, a common practice is the use of the Ohnesorge diagram to classify inks into printable and not-printable (see Figure 2.7). Ink properties resulting in an Oh of around 0.1 to 10 can be printed within certain velocity ranges according to this assumption, even though other ranges have been shown by other researchers.

To see if the model can simulate the difference between a fluid in the printable and non-printable range, a selection of three fluids with different characteristics has been chosen. The fluid properties are displayed in Table 3.4 and result in a classification of the liquid within, on the border, and outside of the printable region.

Table 3.4: Fluid properties for three different mixtures of Ethylene Glycol and water. The data has been taken from (Y. Liu and Brian Derby 2019).

Percentage Ethylene Glycol	Density in kg/m^3	Viscosity in $mPas$	Surface Tension in mN/m	Ohnesorge number
10 %	994	1.47	68.9	0.0314
50 %	1048	4.39	60.3	0.0976
85 %	1093	10.5	50.2	0.2506

The simulation of these fluids was performed with the same printhead and actuation waveform as the validation case. In Figure 3.27, the droplet formation process is displayed as four sequential images of the transient simulation. The time-step between each image is 20 μs, starting at 20 μs. The simulation shows a clear impact of the fluid properties on the droplet speed and the tail breakup. The speed and the ejected volume increase for a liquid with lower viscosity. The model predicts a satellite formation for the two liquids with an Oh value below 0.1 and a satellite-free ejection for the mixture with 85 % ethylene glycol. This is in agreement

with the previously made assumptions based on the Ohnesorge diagram. Further investigations on the properties are conducted with the final model for the printhead dimensions of interest.

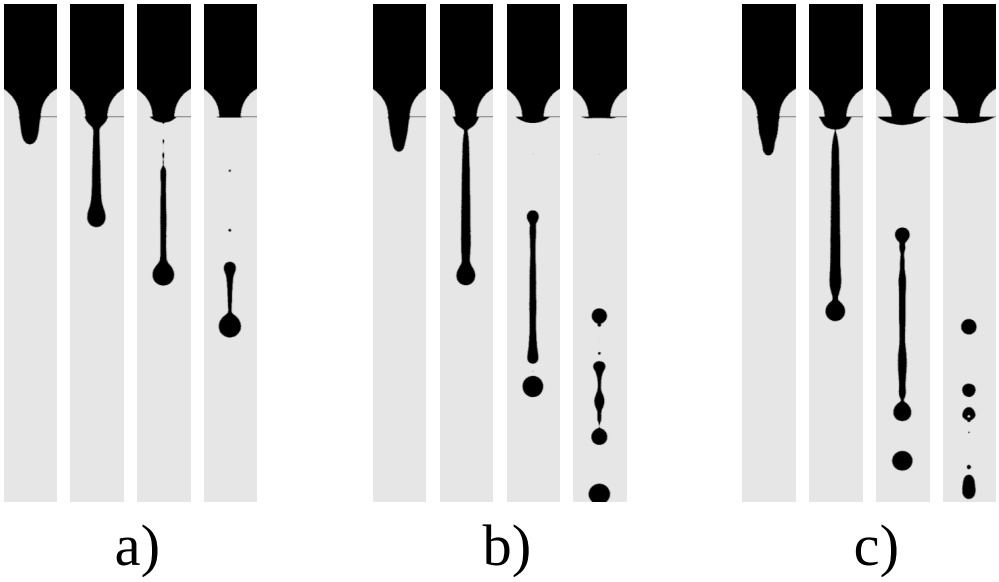

Figure 3.27: Simulation results for three different liquids at the time-steps 20, 40, 60, 80 μs. a) 85 % Ethylene Glycol b) 50 % Ethylene Glycol c) 10 % Ethylene Glycol.

In Figure 3.28 a representation of the simulated fluids within the Ohnesorge plot is presented. The fluids are marked within the schematic based on their ethylene glycol (EG) content.

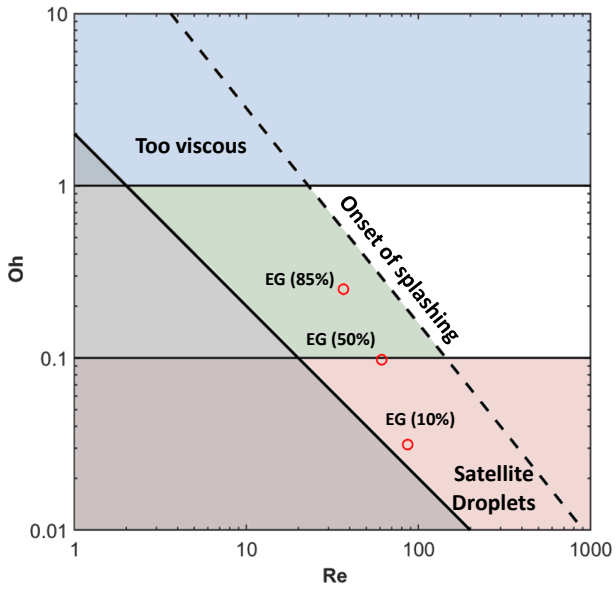

Figure 3.28: Representation of the different fluids within the Ohnesorge plot with the given properties and simulated velocity.

3.6.4 Waveform Properties

Another possible investigation includes the effect of changes in the actuation waveform. In the validation case, a simple sinusoidal oscillation is chosen for the pressure input signal. The oscillation depends on the fluid and printhead characteristics, as well as the actuation strength of the piezoelectric element. Changes in the waveform have a significant effect on the produced droplet, as explained in Chapter 2.2.2. First investigations should provide some initial assumptions of the waveform and possible aspects for future research areas.

To simulate different waveforms and their effect on the droplet formation, the initial waveform from the validation case is altered regarding certain aspects. The amplitude of the waveform is increased by a factor of 0.6, 0.8, and 1.2, respectively. The same factors are used to amplify the period of the oscillation, which stretches the waveform laterally. These two aspects are chosen as a first simple variation of a waveform, showing the effect of higher amplitude and slower oscillation. The waveforms are displayed in Figure 3.29.

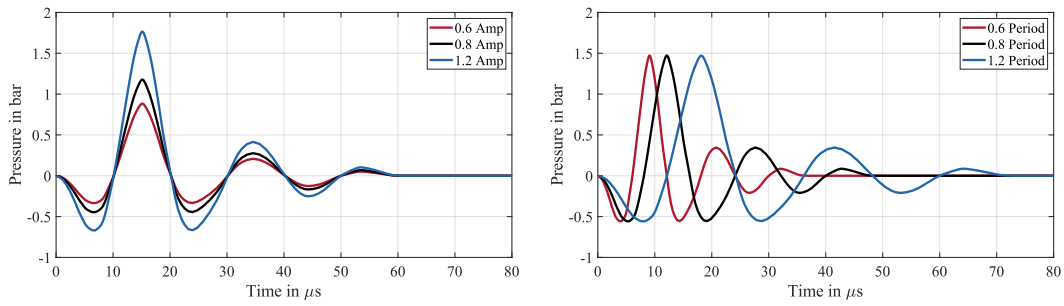

Figure 3.29: Waveform variations of an initial investigation. Left: waveforms with three different amplitudes Right: waveforms with three different oscillation periods.

The simulation of a waveform with increased amplitude leads to an increase in the velocity of the final droplet, which can be seen in Figure 3.30. All waveforms that have the same oscillation period show the same general behaviour of the meniscus movement, extruding from the nozzle plate at effectively the same time. Only the velocity is influenced by the higher amplitude, which results in vastly different jetting results. The change in the oscillation period also results in a velocity change of the final droplet. It can be observed that a percentage increase in the amplitude and a percentage increase in the oscillation wavelength both result in a similar velocity increase of the final droplet. Additionally to the velocity increase, the timing of the liquid leaving the nozzle plate is affected by the oscillation period. A longer period leads to a delay in the droplet jetting, while a shorter period has the opposite effect.

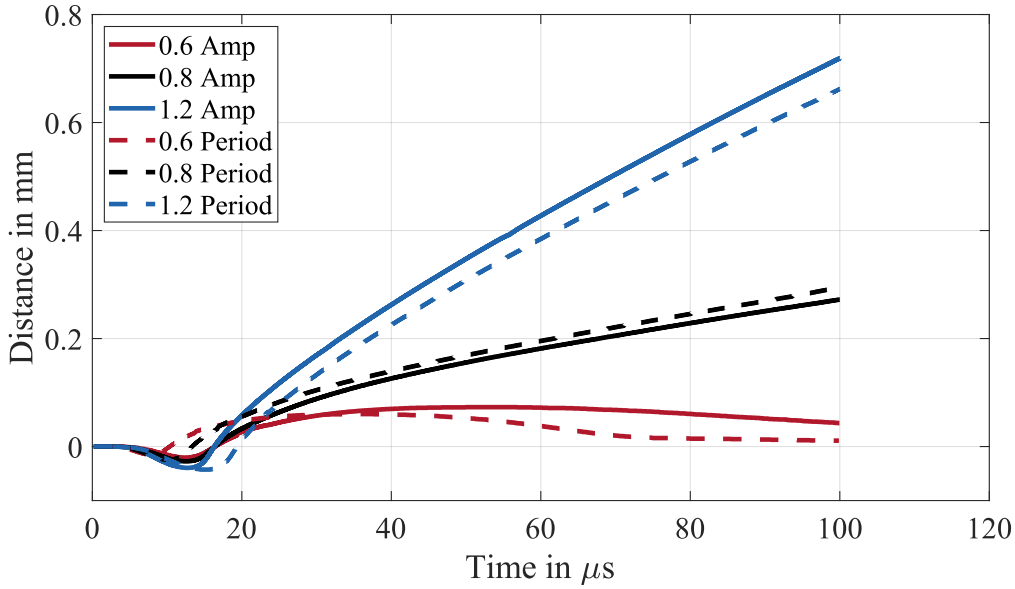

Figure 3.30: Distance (x_h) evolution over time of the head droplet for different actuation amplitudes and oscillation periods.

Experimental Investigation and Model Calibration

In order to adapt the previously created numerical model to a specific print head, experimental tests were carried out in the course of this thesis. These tests enable the adaptation and validation of the model directly to extracted data, with a better control of different boundary conditions. In the following sections, the experimental setup and the derived data is presented. Additionally, an analytical approximation method for the inlet boundary condition is derived, and a model calibration method is presented.

4.1 Conducted Experiments

Experimental studies were conducted to explore the formation of droplets using a printhead of the dimensions that are of interest for the final model. To simplify the needed numerical complexity of the model, a newtonian fluid was selected for the experiments. This allows for a clear description of the fluid properties without the need for complex fluid models. By reducing the complexity of the fluid, a special focus can be set on the interaction between the different domains involved in the droplet formation. A mixture of 1.2 propandiol and water was chosen for this purpose. To investigate the influence of different fluid properties, two mixtures were investigated. The mixtures were based on mass fractions, and the desired composition was mixed in laboratory glass vessels using a commercial scale. The two mixtures have a 1.2 propandiol content of 50% and 25%, respectively. They are referred to as mixture M_{50} and M_{25} in the following sections, respectively. Direct measurements of the fluid properties could not be performed on site, and were derived based on literature values.

The studies were performed with a Samba printhead from Fujifilm Dimatix. This printhead produces a native droplet size of roughly 3 pL and supports fluids with a viscosity range of 4-9 cP. Figure 4.1 shows a three-dimensional model of the printhead. A single printhead holds 2048 individual nozzles that are each controlled by separate Silicon MEMS (micro-electromechanical system) technology. A schematic representation of each nozzle is shown in Figure 4.2. Every nozzle is connected to a common fill channel that supplies the ink chamber with a constant flow of ink and is pressurized. The ink flows through the chamber and leaves the printhead in a combined recirculation channel. A piezoelectric actuator on top of the ink chamber can induce the necessary actuation waveform to produce a droplet at the nozzle.

Figure 4.1: Three dimensional model of a Samba Dimatix printhead (FUJIFILM 2024).

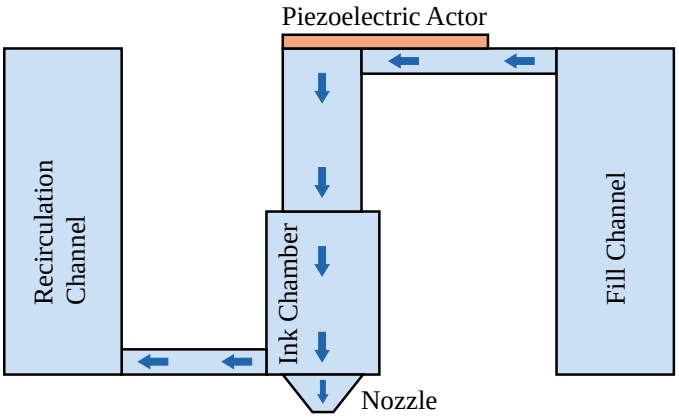

Figure 4.2: Schematic representation of a single nozzle within the printhead.

The experiments conducted for this thesis mainly consist of different unipolar waveform settings. A sweep across multiple voltage amplitudes and pulse widths for single trapezoidal input waveforms was conducted. Additionally, some multi-pulse actuations were performed consisting of an M-shaped and a more complex three-pulse signal. All experiments were conducted for both mixtures. The temperature of the fluid was recorded during the experiments by built-in thermistors of the printheads.

4.1.1 Experimental Setup

The experimental setup consists of the Samba printhead, which is installed into a JetXpert dropwatcher. The dropwatcher is directly connected to a JetXpert measurement software, which shows images of the droplet formation and provides multiple analysis tools. The printhead itself is controlled via the Fujifilm Dimatix DevKit Pro software package (v1.0.36.0). Figure 4.3 shows the setup of the experiments. The dropwatcher of JetXpert consists of three parts: the printhead with a custom mounting plate, a high-speed LED strobe light, and the high-resolution camera system. All three components are synchronised so that the printhead fires a droplet, the strobe light flashes, and the camera records the droplet in flight at a specific delay. The resolution of the camera is half a micron, and it has an 8 million fps-equivalent exposure time. The printhead can be moved laterally to focus the camera on a single nozzle. The fluid is supplied and recirculated by a heated pipe system. The measurement software allows for an image capture of individual droplets in flight. By combining multiple stroboscopic recordings of the droplets from a single nozzle at different time delays, a visualization and description of the droplet formation and tail breakup can be performed. Figure 4.4 shows an example of the gained stroboscopic recording. Each column depicts an image captured of an individual droplet, with varying delay times between the actuation of the printhead and the camera. The delay time is increased by 5 μs starting at a delay of 10 μs. With these stroboscopic image sequences, a calculation of the position, velocity and volume can be performed.

A variety of boundary conditions were defined or have been recorded throughout the experiments. All experiments use an actuation frequency of 20 kHz, which

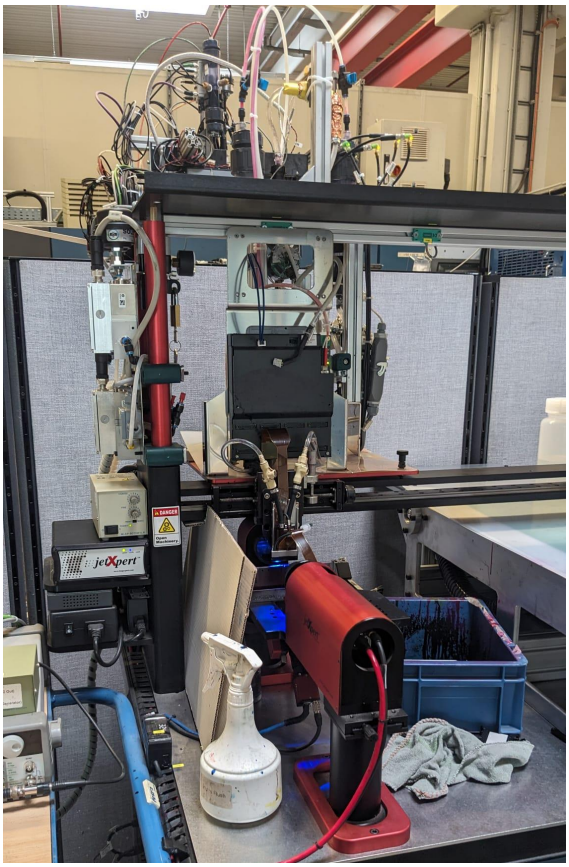

Figure 4.3: Picture of the experimental setup, showing the dropwatcher installation.

results in a droplet formation every 50 μs. The temperature was recorded for every experiment and stayed between 30° and 28°C. The amplitude and pulse width of every waveform was documented. For every experiment, a recording of an image sequence was performed, according to the example in Figure 4.4.

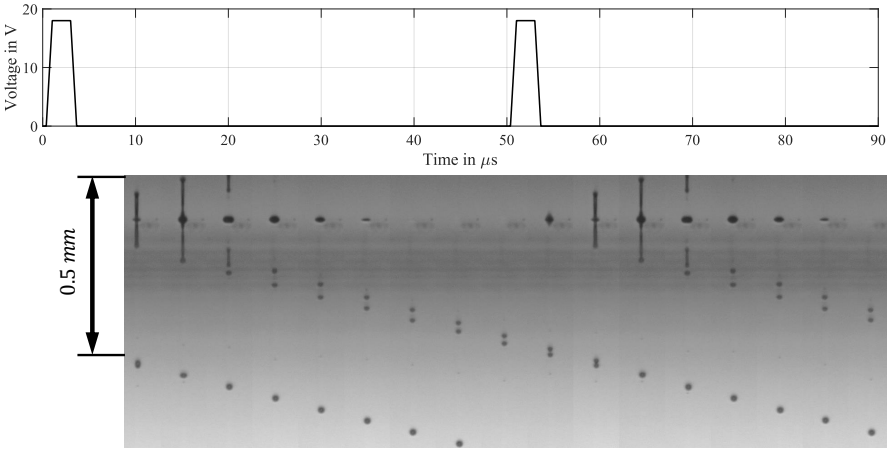

Figure 4.4: Sequential images of the droplet formation process, together with a schematic representation of the actuation waveform and the time delays.

4.1.2 Experimental Data

The extracted data consists of image sequences from the JetXpert measurement software which have been used to calculate the velocity and position of the droplets at different time-steps. A selection of experimental results will be shown within this section.

When examining different pulse widths of a single trapezoidal actuation waveform, the droplet velocity varies in a near quadratic relationship with the pulse width (see Chapter 2.2.2). This is based on the interference of different acoustic waves within the fluid. To reach a maximum droplet velocity, the pulse width needs to be adjusted to the resonance of the fluid and printhead to be able to move the fluid back and forth with a good rhythm.

For the experimental investigation, five different pulse widths (t_{dwell}) with an amplitude of 18 V have been selected: 1.65, 1.97, 2.294, 2.55, 2.87 μs. Not all experiments lead to the successful formation of droplets. Especially with the M_{25} mixture, stable droplet formation was not always achieved. Figure 4.5 shows the extracted data from both experimental runs. Shown is the the dimensionless distance of the droplet from the nozzle plate for the different mixtures and pulse widths. To exclude the travelled distance, the position was divided by the maximum distance from each run. The data was extracted at the same timestep of 50 μs. A shift can be observed between the two fluids, which fits the theory presented in Chapter 2.2.2.

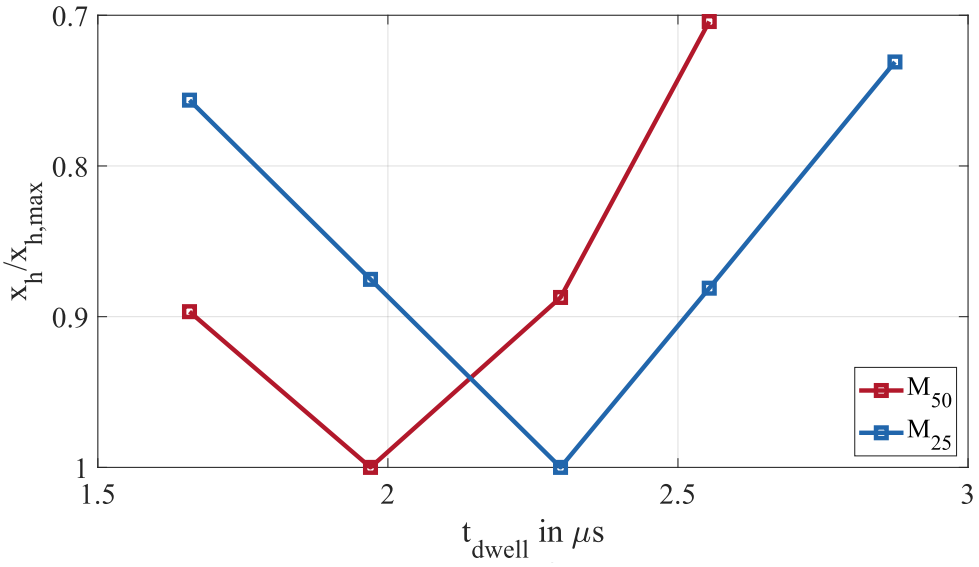

Figure 4.5: Experimental results of the relative droplet distance resulting from different pulse widths and fluid mixtures.

When examining the effect of different amplitudes for a single trapezoidal actuation waveform, the droplet velocity increases almost linearly with an increase in amplitude (see Chapter 2.2.2). This is based on the fact that a higher amplitude creates an increased displacement of the piezoelectric actuator, which results in a higher energy transfer to the fluid. When the velocity of the droplet increases, satellite

formation can occur after a certain velocity threshold.

Several different amplitudes at a constant pulse width of 1.97 μs were tested for the experimental investigations. It could be seen that the velocity changes strongly with an increase in amplitude but follows a clear linear trend. In Figure 4.6, the extracted relationship between velocity and voltage amplitude is presented. At higher amplitudes, the nozzles started to malfunction, which is why only these data points are available for further examination. The 25% mixture reaches higher velocities at the same voltage amplitude as the 50% mixture.

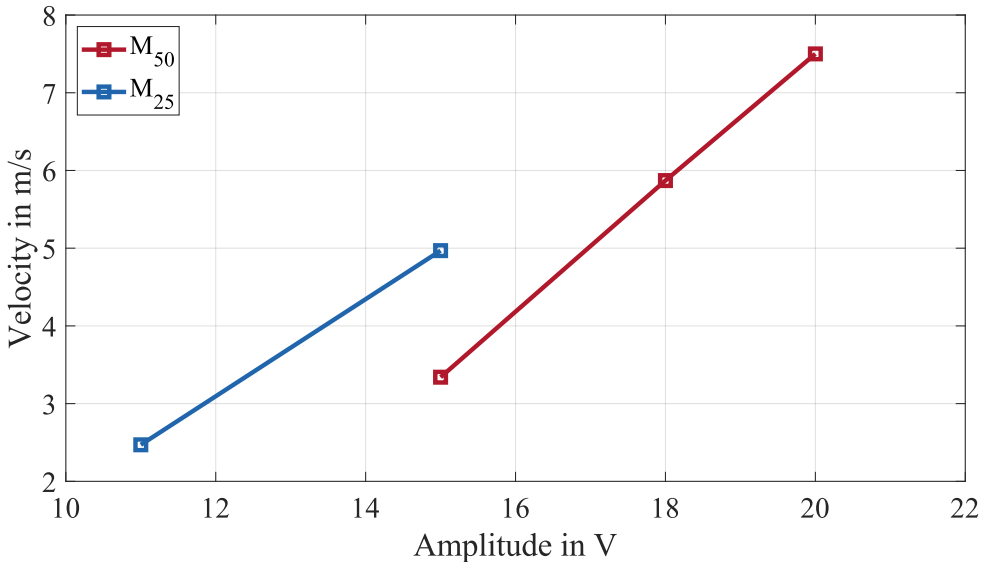

Figure 4.6: Experimental results of the average final droplet velocity ($\dot{x}_h$) resulting from different amplitudes and fluid mixtures.

Additionally to the single-pulse actuation, multi-pulse waveforms have been tested. Two waveforms are presented in Figure 4.7 together with the recorded droplet formation. For both investigations, the mixture M_{50} was selected. The first waveform (a) consists of two individual trapezoidal pulses with the same amplitude. A clear second push of fluid towards the head droplet can be observed, which leads to a higher droplet volume. The second waveform (b) consists of three individual pulses with changing amplitudes. The first two pulses are mainly increasing the volume of the droplet, while the additional task of the final pulse is the collection of the tail. It can be observed that the produced droplet from this waveform has an even higher volume and no remaining satellite droplets in comparison to the two-pulse waveform.

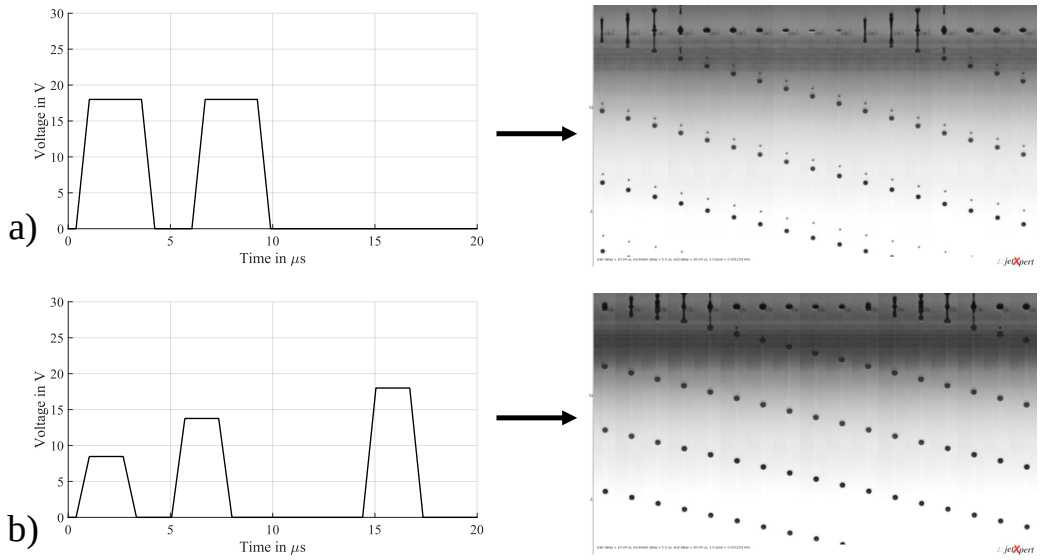

Figure 4.7: Display of the used multi-pulse waveforms together with the experimental recordings. a) Unipolar M-shaped pulse b) Complex pulse with 3 unipolar pulses.

4.1.3 Challenges

Certain challenges have made the experimental investigation and parts of the gained results not usable for this thesis or need to be considered when using the extracted data.

Ensuring consistent focus on the same nozzle proved challenging due to misalignments and occasional nozzle clogging during the experiments. After each printhead cleaning, realignment of the camera was necessary, making it difficult to maintain focus on the previously observed nozzle. As a result, minor discrepancies between results may arise, as every nozzle shows slight differences in their behaviour. Hence, it's important not to regard the experimental outcomes of a single nozzle as definitive; rather, they should be viewed as an indication of the overall droplet behaviour. For future investigations, an average across multiple nozzles for the same setup should be considered. Furthermore, the temperature could not be held constant during the experiments. Slight changes in the fluid temperature can have significant effects on the viscosity of the fluid and, therefore, its flow characteristics. The temperature was recorded, but still leaves some uncertainties when deriving combined results out of multiple experiments, as seen in the previous chapter. Another point is the occasional air clogging of the pipe system which slowed down the experiments and sometimes resulted in clogged nozzles or pressure fluctuations within the printhead. Even after running the setup for a while, the complete removal of air could not be guaranteed. This could be one of the reasons that certain nozzles behaved differently over time with the same settings. A restart of the system sometimes resulted in a different droplet behaviour. The clear difference in the results led to the exclusion of certain experiments that seemed faulty.

In addition to the setup challenges encountered during data collection, achieving consistent droplet formation with the M_{25} mixture posed its own difficulties. This can be connected to the low-viscosity of this mixture. During the experiments with the M_{25} mixture, some special cases regarding the droplet formation could be observed. Figure 4.8.a shows an example of a fast head droplet detachment. The original head droplet detaches early on from the ligament and leaves a larger droplet behind, which can be considered the new main droplet. The fast droplet recombines with the previously fired droplet after a certain time. In case b) a slow second droplet is formed from the tail, which stays behind the main droplet. It is recaptured by the next actuation and creates a larger droplet, which leads to a significant volume increase. These cases were reached with a voltage amplitude of 15 V and 18 V, respectively. Both cases use a single pulse with a pulse width of 1.97 μs.

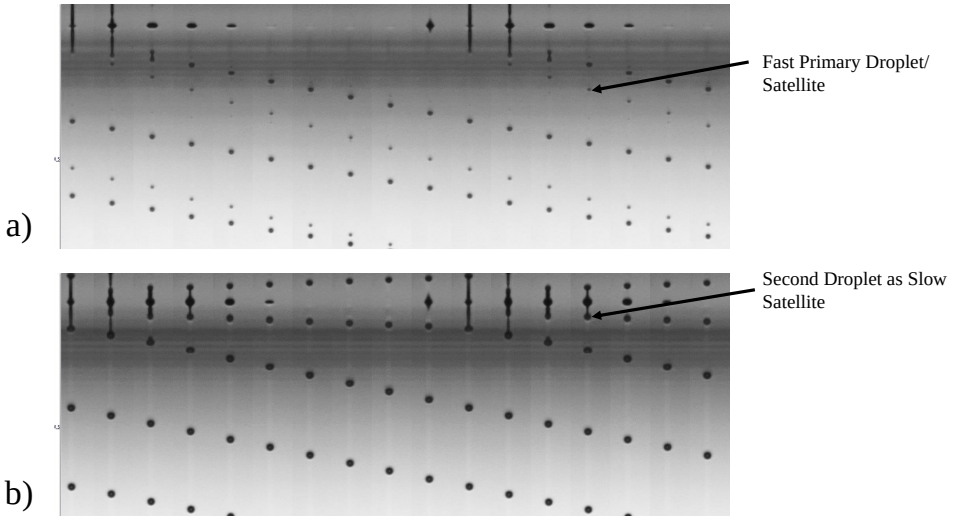

Figure 4.8: Two observed special cases. a) A fast head droplet detachment leads to a significantly bigger tail droplet. b) The oscillation of the meniscus leads to a second droplet, that stays behind. The second droplet reconnects with the primary droplet of the following actuation.

Parts of the presented data will be used in order to validate and test the numerical model. The limited data about the printhead dimensions and resonant frequencies within the ink chamber, create some challenges in the accurate recreation of the observed formation processes.

4.2 Model Calibration

The available data regarding the printhead itself is very limited. Exact dimensions of the internal ink chambers are not available, as well as detailed properties of the actuator and flow characteristics. In order to simulate the experimental observations, an approximation of the inlet boundary condition is essential. Since the available data is limited, none of the previously mentioned methods can be used. Therefore, a new approximation method needs to be developed that enables a rough descrip-

tion of the flow within the nozzle. Only with an inlet condition, the model can be validated and further investigations can be performed.

The goal of the following part is to describe the development process of this model and a corresponding calibration method. The simple approximation should manages to capture the general droplet behaviours that have been observed in the experimental investigations.

4.2.1 Simplifications and Assumptions

Since the exact dimensions of the printhead shown in Figure 4.1 are not available, assumptions need to be made in order to create a numerical model of the process. These assumptions are based on rough measurements made with a 3D Laser Scanning Microscope by Keyence. The nozzle diameter is roughly 17 μm and manufactured into a nozzle plate with an angle of 45°. The dimensions of the ink chamber are based on recordings of previous measurements. The reduced domain of the numerical model of the printhead is shown in Figure 4.9. Even though the real printhead and nozzle have a rectangular shape, an axisymmetric approach is chosen. This is due to the constrained time available, which doesn't allow for the consideration of a three-dimensional model. Given that the printhead dimensions are based on assumptions rather than representing the exact printhead, this simplification is deemed acceptable for initial simulations and will be assessed based on the results obtained. As a contact angle between the nozzle surface and the fluid, a value of 20 degrees is chosen based on the previous simulations.

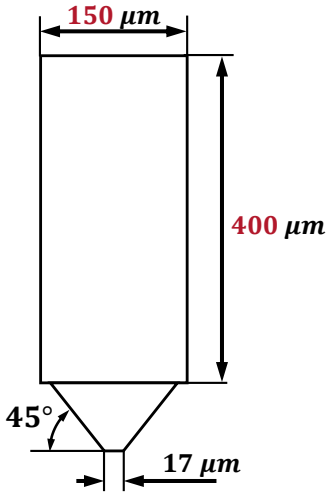

Figure 4.9: Schematic printhead domain with rough dimensions.

In addition to the printhead dimensions, the primary uncertainty in the model lies in the actuation waveform. As seen in the previous chapters, the actuation waveform has the biggest influence on the droplet formation process. Getting good assumptions for the waveform is, therefore, essential to generate useful numerical results. Previously mentioned methods involve FSI simulations, equivalent circuits or narrow channel theory models. All these techniques require a more detailed analysis of the printhead itself, which is why they can not be used in this thesis. A different

method is therefore derived that builds on the assumption that the jetting system can be simplified as a resonant circuit.

As stated in Chapter 2.2.1, the movement of the piezoelectric element leads to acoustic wave propagation in the ink chamber. This acoustic wave can essentially be seen as a pressure change in the ink chamber. Since the timescale is short and the travel times are fast, it is assumed that the pressure within the chamber is approximately the same everywhere. At the beginning of an actuation signal, the system is in an equilibrium state. When the piezoelectric actuator expands due to a voltage signal, it creates a lower pressure in the ink chamber (see Figure 4.10). This low pressure is equalled out over time and falls back to the previous pressure level of the system. Two factors can be seen as responsible for the pressure to go back into its state of equilibrium: the retraction of the meniscus and the fluid flow through the recirculation and re-fill channel. When the piezoelectric element falls back into its non-actuated state, it creates a pressure increase in the ink chamber. This pressure increase is equalled out by the movement of the meniscus, optimally resulting in the formation of a droplet.

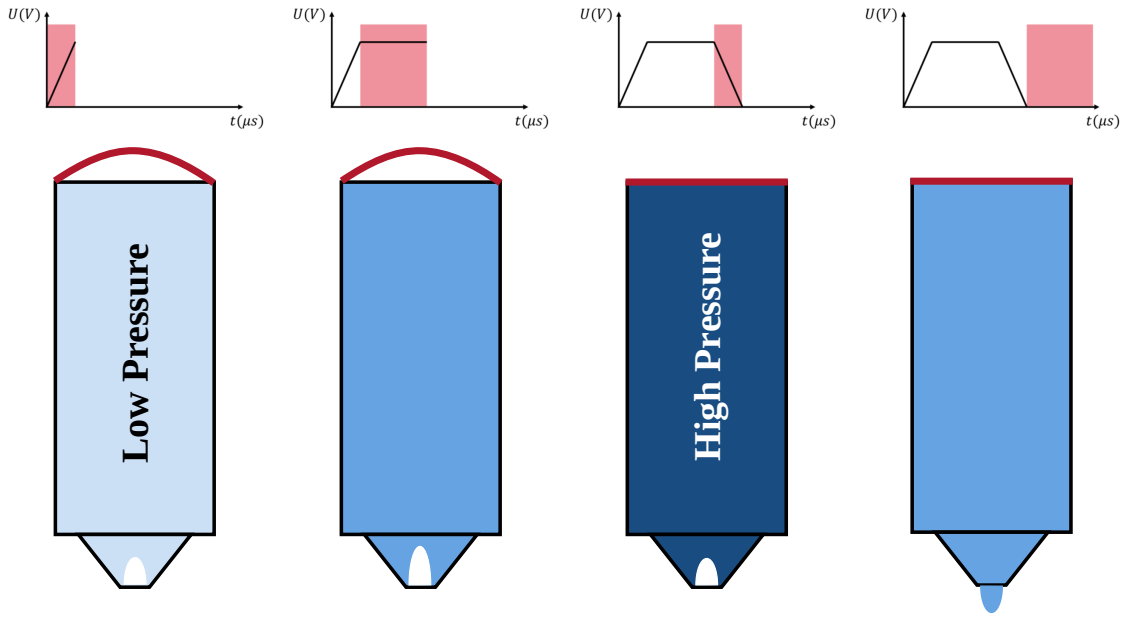

Figure 4.10: Schematic representation of the pressure changes in the ink chamber during the application of a driving waveform.

Using this simplified approach, the system is streamlined into two resonant circuits aimed at harmonizing the pressure fluctuations within the ink chamber (see Figure 4.11). The jetting circuit is considered as the main driver of the droplet formation process. A similar simplification has been presented by Fujifilm Dimatix at the Inkjet Conference 2019, where the refill resonance was assumed to be around 1/10 of the jetting resonance. For the modelling approach of the jetting itself, only the jetting resonance is considered since the refill circuit is not modelled in the axisymmetric model (see Figure 4.9).

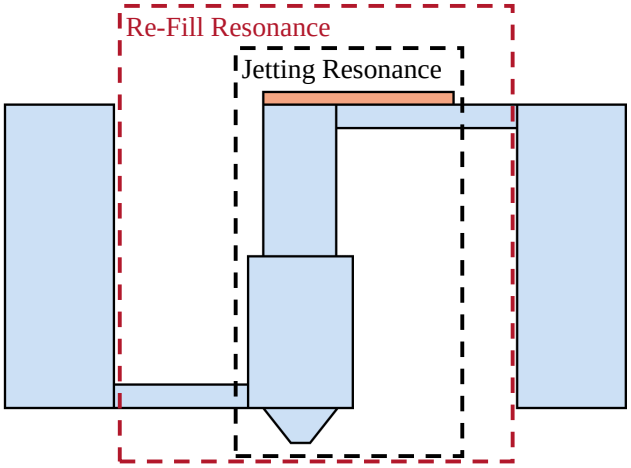

Figure 4.11: Reduction of the printhead system into two resonance circuits.

4.2.2 Fluid Properties

The properties of the fluid play a crucial role in the droplet formation process. In order to simulate the droplet ejection and compare the simulation with the experimental data, values for the properties of the different mixtures are needed. Since they could not be measured directly during the experiments, they were approximated based on literature about the used fluids.
An analytical and experimental study by Khattab et al. (2017) presents measured and calculated values for the dynamic viscosity, density, and surface tension of water and propylene glycol mixtures. They provide data for different mole fractions and at different temperatures. Based on their findings, the values that are presented in Table 4.1 are interpolated for mixture M_{50} and M_{25} at a temperature of 28.5°C. This corresponds to the experimental conditions during the tests.

Table 4.1: Fluid properties for M_{50} and M_{25} at 28.5°C, based on (Khattab et al. 2017).

Mass fraction of $C_3H_8O_2$	Density in kg/m^3	Viscosity in $mPas$	Surface Tension in mN/m	Ohnesorge number
50 %	1030	3.7	48.11	0.180
25 %	1013	1.7	54.62	0.078

The interpolated properties are used in the following simulations to recreate and calibrate the experimental findings. For the initial calibration, the M_{50} mixture is chosen since more valuable data could be gained in the experimental tests.

4.2.3 Waveform approximation

The simplification of the printhead to a resonance circuit builds the basis to transform an electrical input signal into a pressure wave input. The assumption is made that the jetting resonance circuit reacts to the volume change with the natural response of an electric resonance circuit. This assumption is based on the Lumped element model approach, which makes the analogy that the electric current (i) and

the voltage (V) are equivalent to the volumetric flow rate (Q) and pressure difference (ΔP), respectively. The natural response of an LCR circuit is displayed in Figure 4.12. In the resonance case, the LCR system reacts to a change of state with an exponentially damped sinusoid function (Plonus 2020).

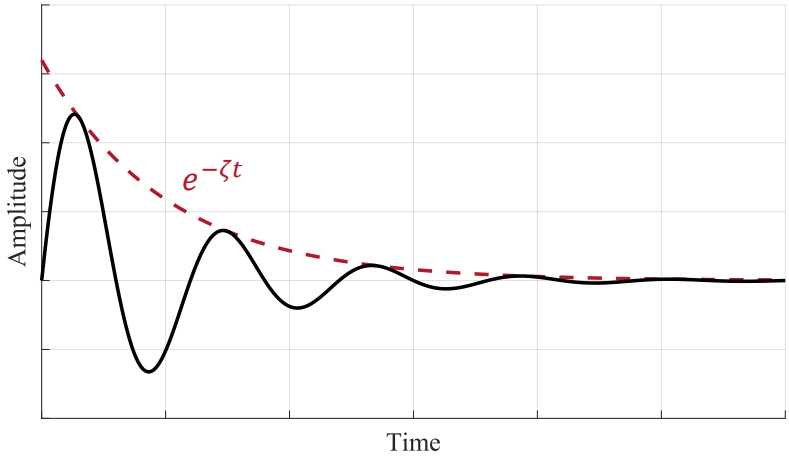

Figure 4.12: Generalized natural response of an LCR circuit.

The function of the response can be written as:

$$V = Ae^{\zeta t} \sin\left(\frac{2\pi}{\omega} t\right) \tag{4.1}$$

where A represents the amplitude of the oscillation, ζ the damping factor, and ω the wave period. This equation describes a classical damped oscillation. In this analogy, the voltage represents the pressure difference and the amplitude of the oscillation depends on the amount of change from the equilibrium state.

$$\Delta P = A_p e^{\zeta t} \sin\left(\frac{2\pi}{\omega} t\right) \tag{4.2}$$

$$A_p = \beta A_V \tag{4.3}$$

where A_p is the amplitude in Pa, A_V is the amplitude in V, and β is a constant with the unit Pa/V. This approach only considers an analytical approximation of a possible waveform. The response is, therefore, only considered as a natural response regarding a change of state. Further investigations, like the consideration of the response to a ramp function are not considered. The volume change that is induced by the piezoelectric element is, therefore, assumed to be instantaneous. A more detailed representation of a resonance circuit could be the aim for further investigations but was not considered for the simple approximation method since it would introduce more parameters that require data fitting.

The final approximation method for the pressure wave within this thesis can be described as follows. The voltage signal to the piezoelectric actuator leads to an expansion and contraction of the actuator. This movement leads to a decrease and

increase in pressure within the ink chamber. The pressure increase is considered to be the same everywhere, and the actuation is considered instantaneous. This results in two natural responses of the resonance circuit, which are induced at the beginning of each actuation (t_1,t_3). A schematic representation of the two responses is shown in Figure 4.13. The pull motion of the actuator leads to a negative pulse, while the push motion results in a positive pulse. Both responses are superimposed to create the final pressure waveform, which is used as the inlet condition for the numerical model. The amplitude of the response is directly coupled to the amplitude of the voltage signal with the constant β.

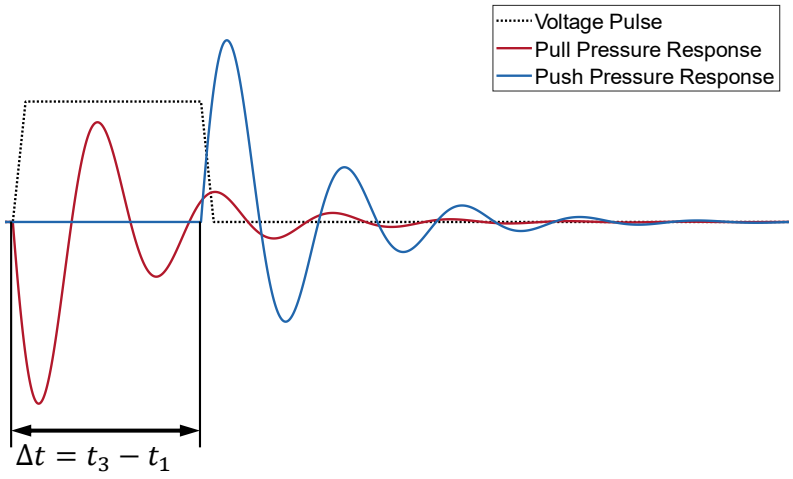

Figure 4.13: Schematic representation of two pressure wave responses, in relation to a voltage signal.

The final equation for a single voltage pulse response as a pressure waveform depends on the time of the responses and the previous parameters. It can be written as:

$$\begin{aligned}
\Delta P(t) &= 0 && (t < t_1) \\
\Delta P(t) &= A_p e^{\zeta(t-t_1)} sin\left(\frac{2\pi}{\omega}(t-t_1)+\pi\right) && (t < t_3) \\
\Delta P(t) &= A_p e^{\zeta(t-t_1)} sin\left(\frac{2\pi}{\omega}(t-t_1)+\pi\right) \\
&\quad + A_p e^{\zeta(t-t_3)} sin\left(\frac{2\pi}{\omega}(t-t_3)\right) && (t >= t_3)
\end{aligned} \tag{4.4}$$

where t_1 is the time of the first response, and t_3 is the timing of the second response. This function can be implemented as a field function within StarCCM+ and provides a basis for data fitting with the experimental data. This method represents a very simplified approach to a problem with very limited available data. If this method can simulate the droplet formation to a sufficient degree will be tested after the model calibration.

Wave Period

The first step of the calibration process is to select a fitting wave period ω. As seen in the experimental results, a sweep across multiple pulse widths results in

a near quadratic relationship to the droplet velocity and, therefore, position over time. This effect is based on the superimposing waveforms of the push pulse and the residual vibration of the pull pulse. At an optimal interference, the pressure peak results in a maximum velocity of the resulting droplet. In order to recreate this effect, different pulse widths have been simulated, using an amplitude of $A_p = 1.6$ bar, a period of $\omega = 5.2\ \mu s$ and a dampening factor of $\zeta = 250000$. The value Δt was varied in intervals of $\pm 10\%$ starting from $\Delta t = \omega/2$, by changing t_3 in equation 4.4. The superimposed pressure waveforms that result from this are presented in Figure 4.14.

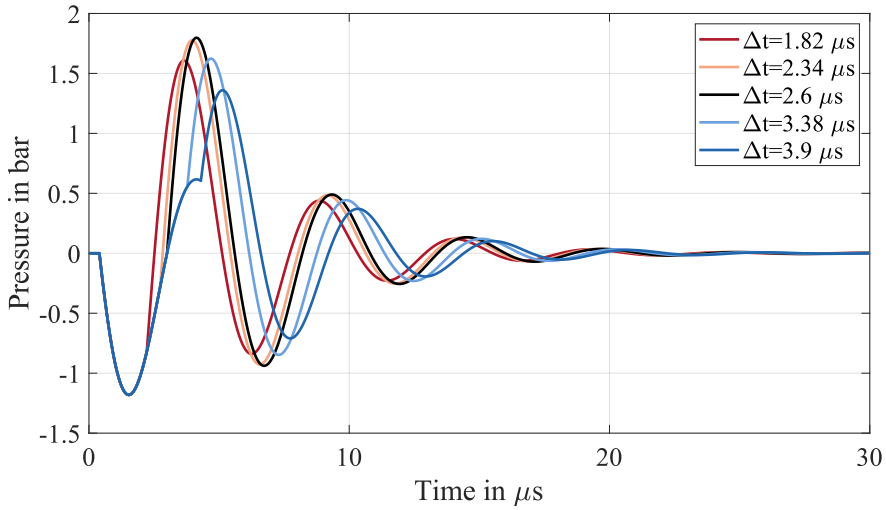

Figure 4.14: Pressure waveforms for different pulse widths.

The resulting droplets are presented in Figure 4.15. A clear near quadratic relationship of the droplet velocity can be seen based on the position of the droplets at the same time-step. The quadratic relationship enables assumptions on the period of the resonance since a clear optimum can be observed. Matching the optimum between the experimental results shown in Figure 4.5 and the simulation results can give an approximation of the resonance frequency within the printhead.

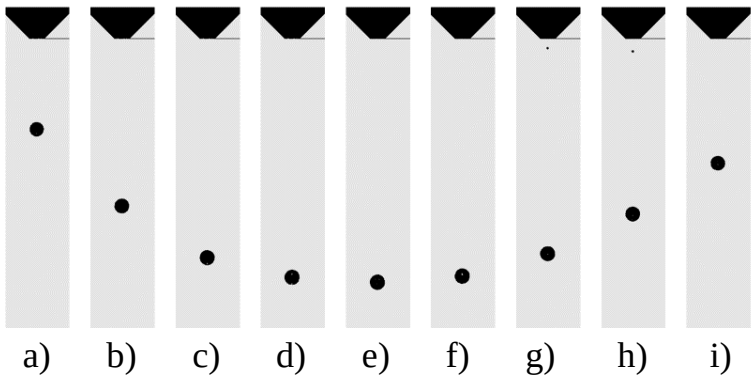

Figure 4.15: Simulated droplets at 50 μs for different pulse widths Δt: a) 1.82 μs b) 2.08 μs c) 2.34 μs d) 2.6 μs e) 3.12 μs f) 3.38 μs g) 3.64 μs h) 3.9 μs

To test the connection between the resonance frequency and optimal pulse width, the same simulations have been repeated for multiple values of ω. In Figure 4.16, the resulting relative droplet position for different pulse widths and values of ω are presented. It can be seen that a change in resonance period corresponds to a shift in the distribution. This supports the assumption that the optimal droplet ejection is achieved when the pulse width is aligned with the resonance period, which changes with material properties. The slopes of the different distributions are affected by the velocity of the droplet and time when the data is extracted. It is therefore important to focus on the position of the maximum.

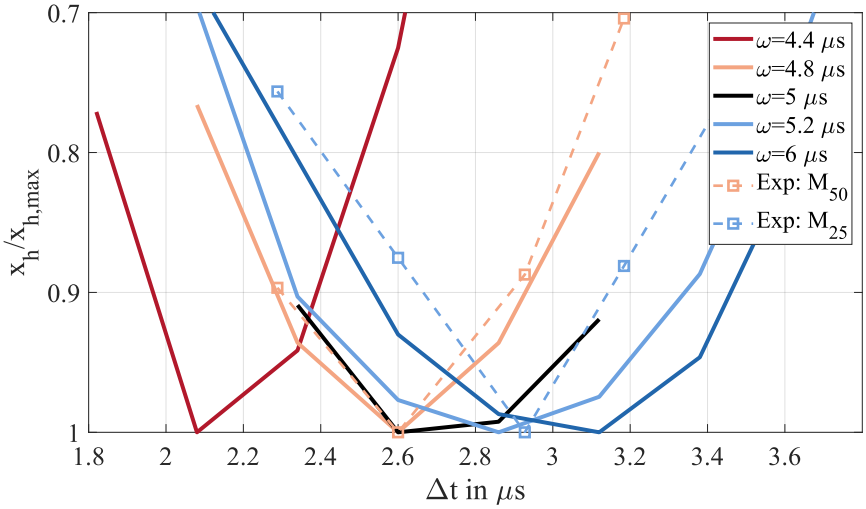

Figure 4.16: Simulation results of the relative droplet distance resulting from different pulse widths and resonance frequencies. All distances are derived at the same timestep of 50 μs.

In order to calibrate the model to the experimental results, a resonance period needs to be chosen that closely matches the point of maximum velocity measured during the experiments. Since the resonance period is mainly determined by the printhead geometry and the fluid properties, it needs to be matched with experimental investigations for each different fluid. For the limited data extracted from the experiments, presented in Figure 4.5, a resonance frequency of $\omega = 4.8\ \mu s$ is selected for mixture M_{50} and $\omega = 5.2\ \mu s$ for mixture M_{25}.

Amplitude

After specifying the resonance period, the amplitude of the resonance can be calibrated. To do so, different values of A_p have been selected and simulated. The investigated waveforms with different values for A_p are shown in Figure 4.17. The dampening factor is again set at $\zeta = 250000$, and the resonance frequency is selected based on the previous calibration step to $\omega = 4.8\ \mu s$ for mixture M_{50}.

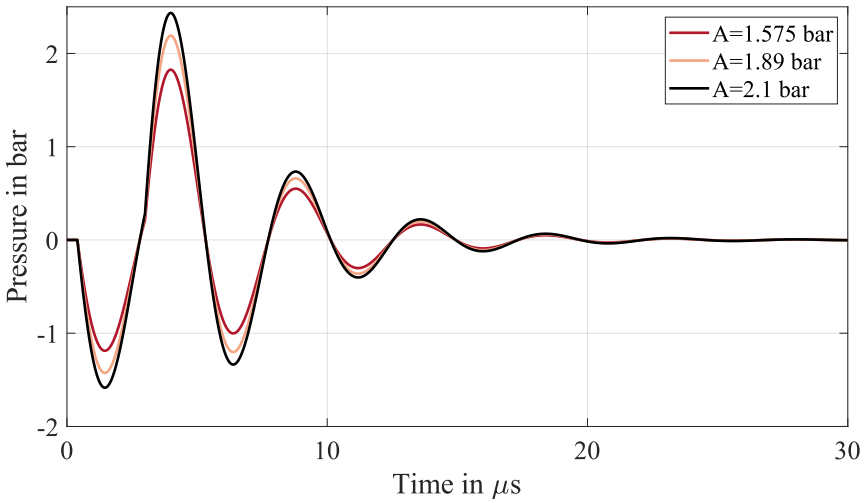

Figure 4.17: Pressure waveforms for different amplitudes.

When comparing the average velocity between 40 and 60 μs, a nearly linear increase in velocity with increasing A_p can be observed (see Figure 4.18). These results match the previous expectations from the initial investigations in Chapter 3.6.4.

In order to convert the linear correlation between voltage and velocity into a linear correlation between pressure and velocity, the transformation coefficient denoted as β is employed.

$$A_P = \beta A_V \tag{4.5}$$

For mixture M_{50} a coefficient of $\beta = 10500\ Pa/V$ is determined, leading to a close match between the resulting velocities from different voltage amplitudes A_V and pressure amplitudes A_p. In Figure 4.18 the experimental velocities for mixture M_{50} are displayed, after transforming the amplitude.

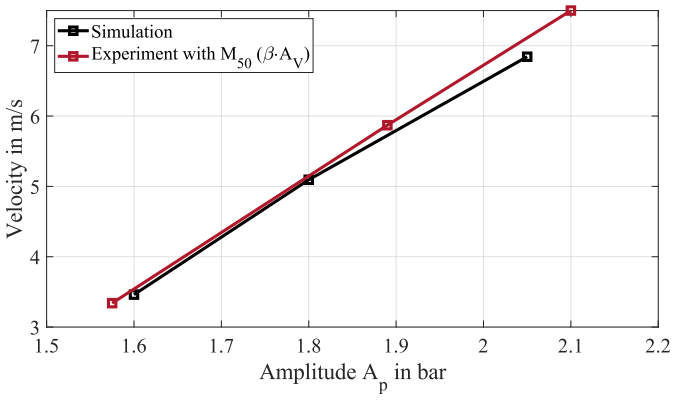

Figure 4.18: Simulation results and transformed experimental results, showing the average droplet velocity at different amplitudes.

Dampening

Choosing the dampening factor with the available data is a more challenging task. The dampening of the resonance influences the amplitude of the oscillation, which in return influences the superimposed responses. In Figure 4.19, the superimposed pressure waves for multiple dampening factors are shown. It becomes clear that the dampening affects not only the residual vibration of the fluid within the chamber but also the maximum peak of the waveform. This results in a different droplet velocity for different dampening factors. It is, therefore, necessary to recalibrate β depending on the chosen dampening.

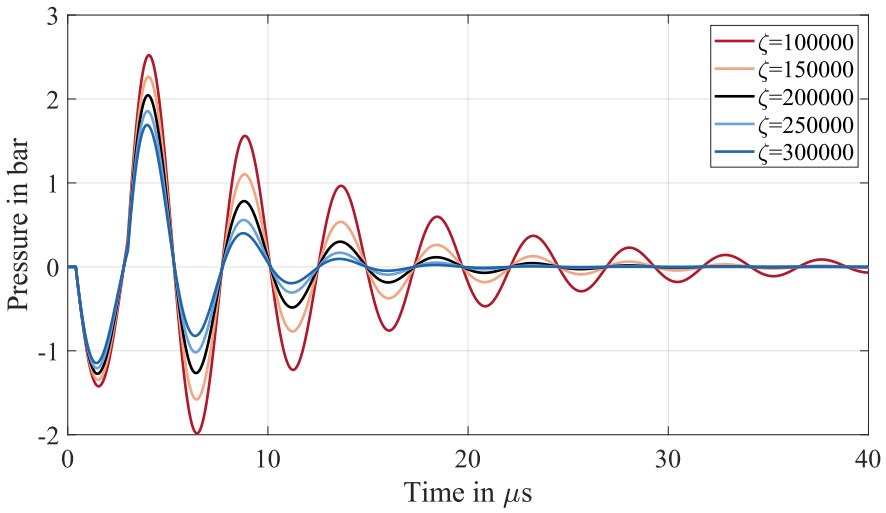

Figure 4.19: Pressure waveforms for different dampening factors.

Not only does the dampening influence the velocity of the droplet but also the tail breakup due to the residual vibration of the meniscus. In Figure 4.20, the droplet formation for three different dampening factors is presented. The simulations are conducted with a dampening factor of 100000, 200000, and 300000, respectively. The higher dampening leads to a slower droplet speed and volume while slowing down the meniscus movement. The low dampening value leads to a strong oscillation in the meniscus, which results in the formation of a second droplet, similar to special case b, presented in Figure 4.8. To investigate a possible calibration of the transformation function regarding the dampening property of the printhead-fluid combination, a comparison between several cases with equalized droplet velocities can be conducted.

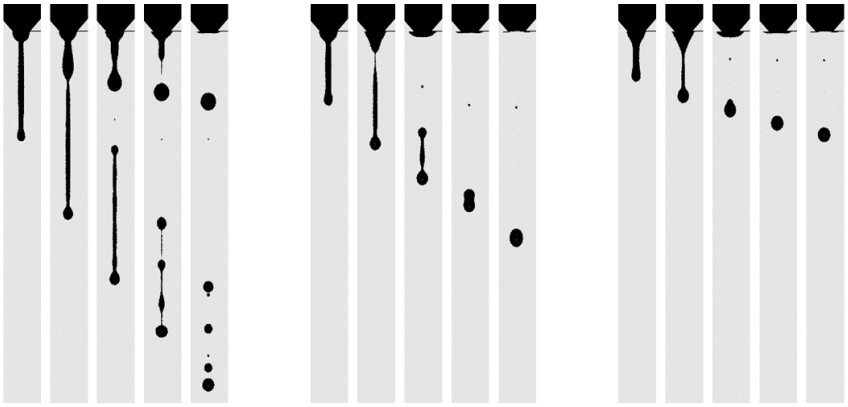

Figure 4.20: Simulation results showing the droplet formation for different dampening factors at sequential timesteps 10, 15, 20, 25, 30 μs. The dampening factor equals a) 100000 b) 200000 c) 300000

To assess the change in velocity, a recalibration according to the previous calibration step can be performed for different values of ζ. The results of these calibrations are shown in Figure 4.21. It becomes clear that an increase in dampening requires an increase in β to match the experimental velocities. This is in line with the assumption that a system with higher dampening properties requires a stronger pulse to perform a successful droplet ejection.

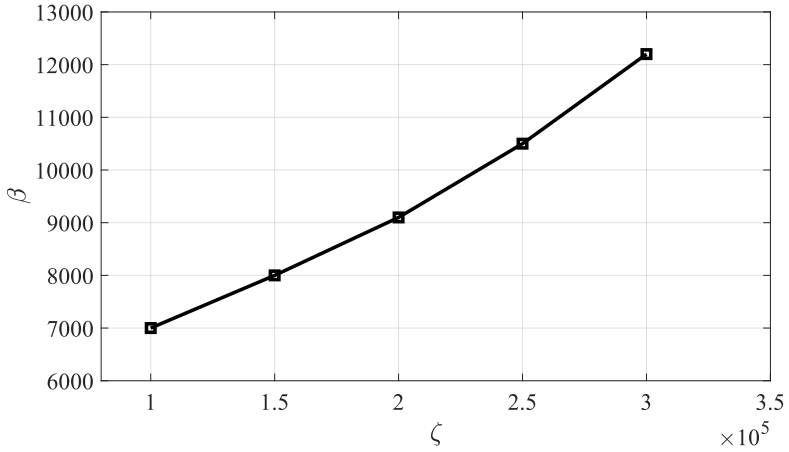

Figure 4.21: Relationship between the dampening factor ζ and β resulting in an approximately equal velocity transformation between voltage and pressure waveform.

At this stage, a value of $\zeta = 250000$ was selected since it provides a reasonable droplet formation that closely resembles the experimentally achieved results. Further investigations at this point with multiple experiments could improve the model performance regarding the tail breakup. These investigations can include a more

detailed sweep across multiple pulse widths and a closer look at the meniscus oscillation. In a few simulations, a sight connection between the slope of the quadratic relation and the chosen dampening factor could be observed. This can be explained by the increase or decrease of the effect of residual vibrations on the second response.

Results and Discussion

In this chapter, the developed numerical model is tested for its capabilities to recreate the experimental results of the Samba printhead. After the investigation of the model's capabilities in recreating experimental outcomes, different fluid properties are tested and their effect on the droplet formation process. This includes the effects of density, viscosity, surface tension, and the combined effect when switching the model from the previously calibrated M_{50} mixture to the M_{25} mixture.

5.1 Experimental Validation

After the initial calibration, the analytical response based on equation 4.4 and the parameters $\omega = 4.8\ \mu s$, $\beta = 10500\ Pa/V$, and $\zeta = 250000$ for the mixture M_{50} is selected. In order to test this calibration, several experiments are investigated. First, single-pulse waveforms are tested, followed by more challenging multi-pulse waveforms. Afterwards, the applicability of the model to different Newtonian fluids is examined.

5.1.1 One Pulse Waveform

The simplest form of actuation in the experimental setup is the single pulse waveform. According to the designed model, this waveform results in two superimposed pressure wave responses according to equation 4.4. To investigate the capabilities of the model to match the experimentally observed outcome, the previously determined parameters are chosen and applied to the voltage amplitude and the pulse width recorded in the experiments. The simulations are afterwards compared to their experimental counterpart. The most important properties are the satellite droplet formation and, therefore, the tail breakup. But also the general droplet trajectory, velocity, and volume play an important role in the modelling of the process.

The first simulations investigate the model at different voltage amplitudes. The chosen experiments have a voltage amplitude of 15, 18, and 20 V, respectively. The time Δt between push and pull response is 2.6 μs, and the mixture is M_{50}.

In Figure 5.1, the comparison between the experimental results of a droplet formation with a voltage amplitude of 15 V and the corresponding simulation with the numerical model is presented. The images are taken at intervals of 5 μs beginning at 10 μs. A very close resemblance between the experimental droplet formation and

the simulation can be observed. The tail breakup is correctly predicted and shows a small satellite that reconnects to the primary droplet.

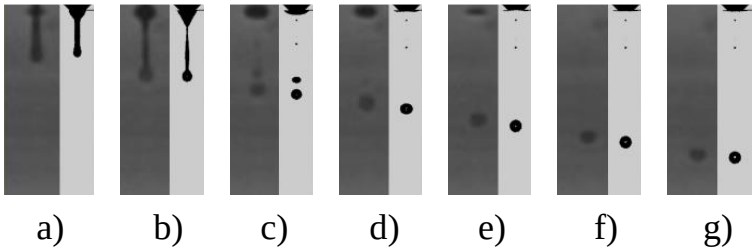

Figure 5.1: Comparison between experimental results of a droplet formation with an actuation amplitude of 15 V and the simulation with the calibrated model. The images are taken at 10, 15, .., 40 μs, respectively.

Figure 5.2 shows the same comparison for a voltage amplitude of 18 V. Again, the pictures are taken every 5 μs beginning at 10 μs. The tail behaviour in the simulation is again very similar to the experimental results. However, the tail does not experience a front pinch-off at time-step (c), resulting in the contraction of the tail into the head droplet instead of forming a satellite. The general behaviour can be seen as adequately matched and a front pinch-off could possibly be achieved with further calibration.

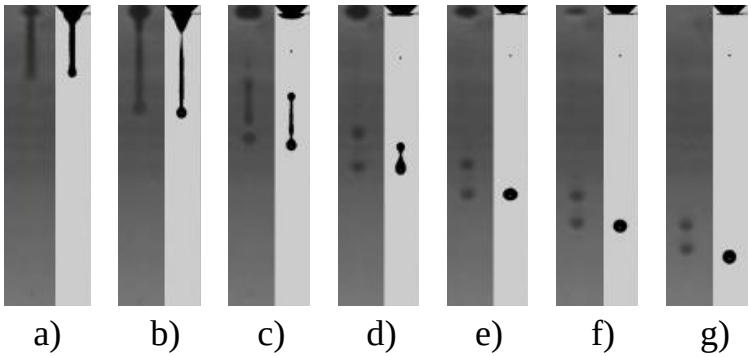

Figure 5.2: Comparison between experimental results of a droplet formation with an actuation amplitude of 18 V and the simulation with the calibrated model. The images are taken at 10, 15, .., 40 μs, respectively.

In Figure 5.3 the results for a voltage amplitude of 20 V are shown. A close match between the simulation and the experimental data could be achieved. This case also shows an example of a satellite droplet that is formed during the tail breakup and does not catch up to the main droplet. Both experimental case and simulation show the same outcome in that regard. The model, therefore, successfully manages to capture the limit, after which satellite droplet occurs.

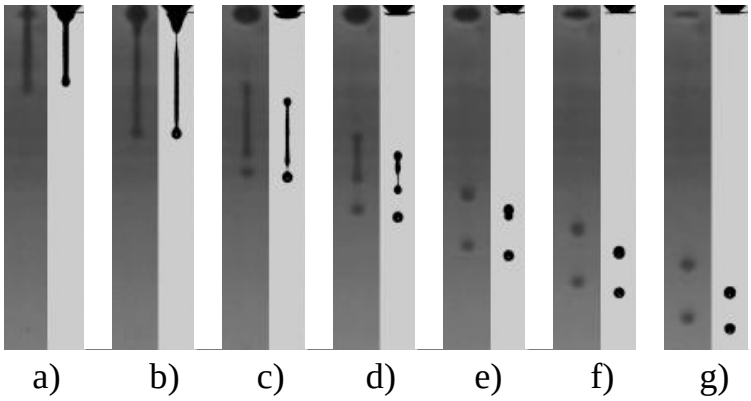

Figure 5.3: Comparison between experimental results of a droplet formation with an actuation amplitude of 20 V and the simulation with the calibrated model. The images are taken at 10, 15, .., 40 μs, respectively.

A comparison between the trajectory of the droplets in the experiments and the simulated droplets is presented in Figure 5.4. The simulation effectively captures the trajectory in all cases to an adequate extent.

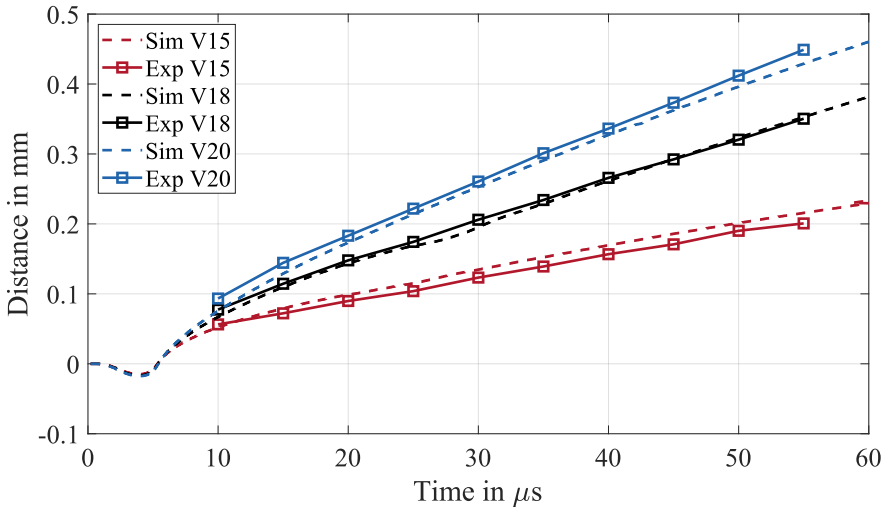

Figure 5.4: Trajectory comparison between experimental droplets and simulated droplets at different amplitudes showing the distance (x_h) of the head droplet.

In the simulation presented in Figure 5.2, the biggest difference in tail behaviour could be observed between the shown comparisons. A second investigation regarding the model parameters was therefore conducted to investigate the possible effects of the model parameters presented in Chapter 3.6.2. Both the second-order time discretization and the HRIC gradient smoothing option resulted in a satellite droplet formation that resembles the experimental observation to a better extent. Additionally, no notable need was observed for a more refined resolution of the free surface. Therefore, it is advisable to prioritize higher-order time discretization over the implicit multi-step solvers. This also leads to a reduction in simulation time. For

the mentioned case, the simulation time is reduced by 15 %. The results with a second-order time discretization are shown in Figure 5.5.

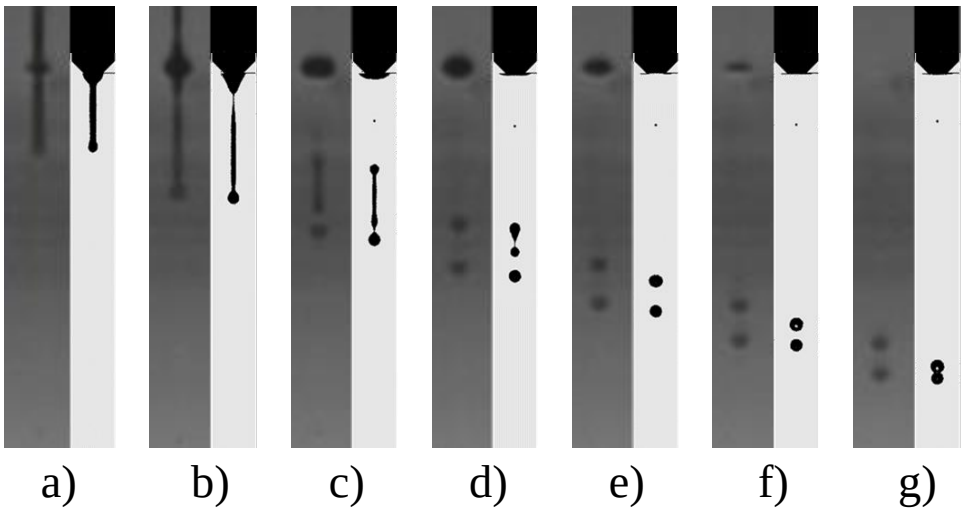

Figure 5.5: Comparison between experimental results of a droplet formation with an actuation amplitude of 18 V and a second order time discretization scheme.

The time-step size was not significantly changed by the different order of temporal discretization, as can be seen in Figure 5.6.

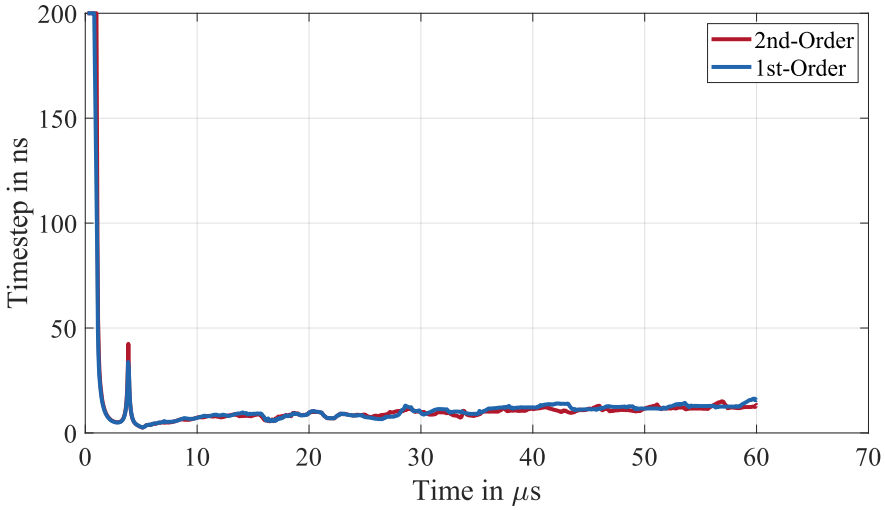

Figure 5.6: Comparison of the time-step size between simulations with first- and second-order temporal discretization.

5.1.2 Multi-Pulse Waveform

A multi-pulse waveform consists of more than one pulse. There are multiple different possible pulse combinations that have been explained previously. They often aim to increase the volume of the droplet or to cancel the residual vibrations in the fluid. To explore these actuation methods, the two waveforms investigated in the

experiments (see Figure 4.7) are simulated in the model.

To perform a simulation for more than one trapezoidal voltage pulse, the pressure waveform equation 4.4 needs to be extended by two additional responses for every added voltage pulse. By superimposing all responses, a combined pressure waveform can be approximated. The waveforms for both actuations are displayed in Figure 5.7. A detailed representation of the individual waveforms that are combined for the final input signal can be found in the Appendix. A second-order time discretization was chosen for these simulations.

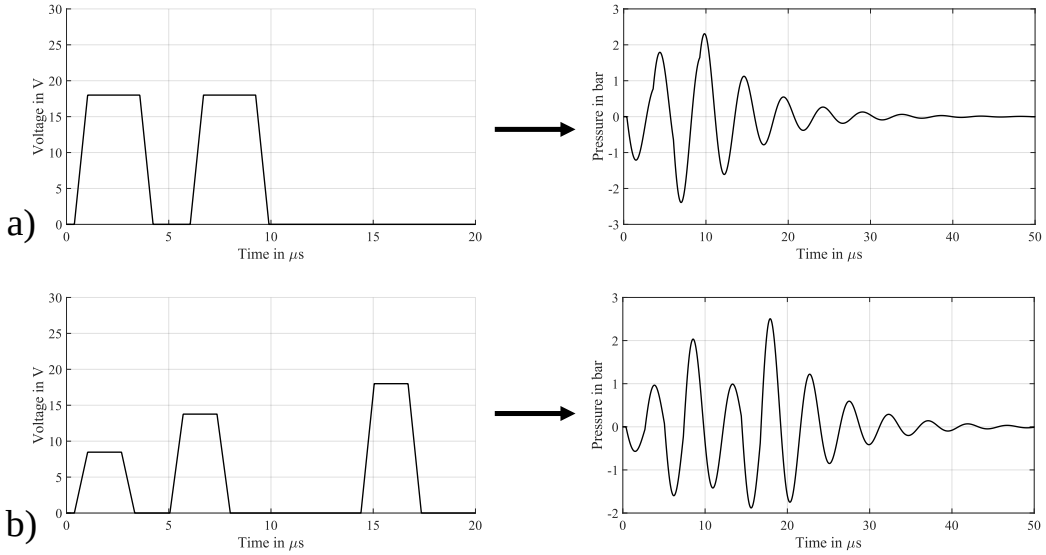

Figure 5.7: Resulting pressure waveform for the multi-pulse actuation. a) M-shaped waveform b) complex waveform.

The results of the M-shaped waveform simulation are shown in Figure 5.8. A good approximation of the general droplet formation can be achieved. The flow behaviour of both pulses is visible in the simulation and the experimental observation. After an initial actuation, the second pulse leads to an increase in droplet volume. The final droplet in the experiments consists of a single droplet with a smaller satellite. The same result was predicted with the simulation. Nevertheless, a difference in final velocity and flow behaviour can be observed. A further calibration of the model parameters could potentially increase the accuracy. Since multiple pulses interact with each other to create the final droplet, the residual vibration of each pulse has a strong impact on the following pulses. Changing the dampening factor, therefore, has an strong impact on the received results. However, the superimposing of multiple pulses leaves room for many uncertainties. One uncertainty is the neglected refill resonance which has an effect on the pressure vibration as well.

When comparing the simulations of the three-pulse waveform with the experimental observations (see Figure 5.9) a close resemblance of the droplet formation can again be achieved. Two smaller initial pulses lead to the increase in volume, while the last pulse collects the tail and leads to a satellite-free droplet. The entire process could

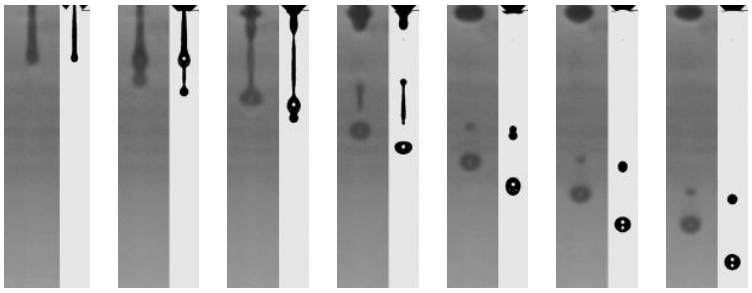

Figure 5.8: Comparison between experimental results of the M-shaped waveform with amplitude of 18 V and the simulation with the calibrated model. The images are taken at 10, 15, .., 40 μs, respectively.

be recreated in the simulation and all steps are visible. However, the final velocity still defers from the observed experiments.

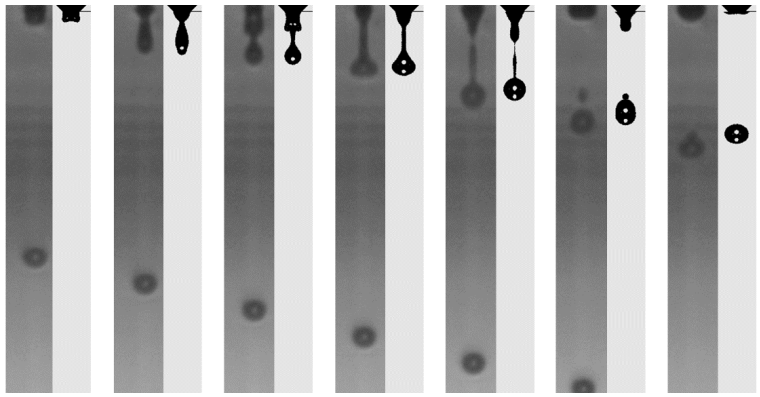

Figure 5.9: Comparison between experimental results of the complex waveform with three sequential pulses and the simulation with the calibrated model. The images are taken at 10, 15, .., 40 μs, respectively.

In general, the simplified model and waveform approximation manage to capture the droplet behaviour and satellite formation even for more complex multi-pulse waveforms to a good extent. This shows the potential of the model to investigate different waveform combinations and fluid parameters. A further investigation into the final droplet velocity and volume is, however, recommended to not only match the droplet formation but also the final droplet speed.

5.1.3 Mixture Change

Switching the model to a different fluid, plays an important role in using the model for future investigations. During the experimental studies, a second mixture was used to observe droplet formation. Slight adaptations are going to be made to

change the model to the new liquid.

The resonance vibration within the ink chamber depends on the chosen liquid. During the experimental investigation, a shift in the quadratic relation between pulse width and velocity could be observed. To change the model to the new fluid, the resonance frequency of the model is changed accordingly. A value of $\omega = 5.2\ \mu s$ is chosen based on the previous calibrations. Moreover, the fluid properties are adjusted to the lower mixture based on the values outlined in Table 4.1.

The special case, presented in Figure 4.8.a, is chosen as a test simulation. For this case, a voltage amplitude of 15 V and a pulse width of 1.97 μs is chosen. The β and ζ values for the waveform transformation are kept the same as for the other fluid. The results are presented in Figure 5.10 and show similar results as the experimental observation. A fast satellite droplet is formed, leaving a slower main droplet behind.

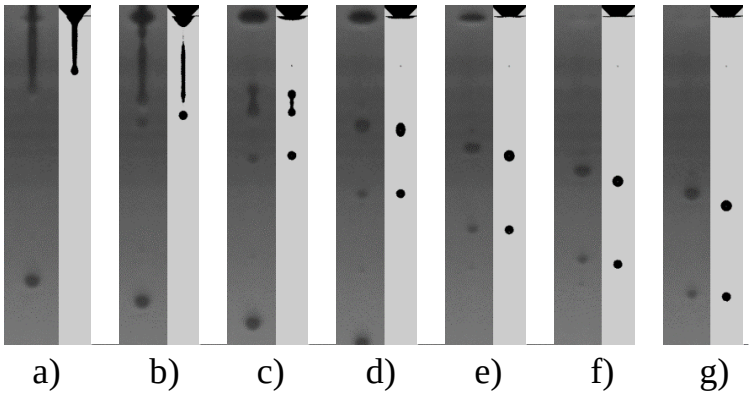

Figure 5.10: Comparison between experimental results of single trapezoidal waveform for the mixture M_{25} and the simulation with the calibrated model. The images are taken at 10, 15, .., 40 μs, respectively.

This shows, that the model is able to switch to different fluids by changing only the resonance frequency and the fluid properties itself. After these outlines switches, the model is again capable to predict droplet behaviour and satellite formation to a good extend, based on these initial investigations. More simulations can be conducted in this regard.

5.2 Parameter Study

The calibrated model was successfully validated through multiple experimental comparisons. The approximated geometry of the printhead and the inlet boundary condition adequately describe the droplet formation process, making the model suitable for various parameter studies. As outlined in the goals of this thesis, these studies will primarily focus on the fluid properties of the chosen liquid. Additionally, a brief investigation into the simulation of multi-drop actuations will also be conducted.

5.2.1 Fluid Property Influence

The important fluid parameters that are further analysed are the density, the viscosity, the surface tension and the contact angle. For all these simulations, the specific property was varied within a reasonable spectrum that is commonly found in fluids. The other parameters were kept constant during the individual investigations. The selected base values are the M_{50} properties listed in Table 4.1. All simulations use the same waveform, which is shown in Figure 5.11. The waveform is the transformed waveform of a single pulse with a voltage amplitude of 20 V and a pulse width of 1.97 μs according to the previously developed approximation method.

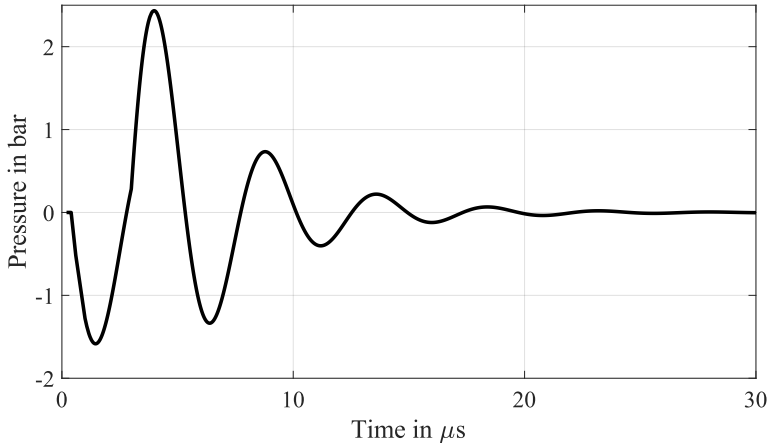

Figure 5.11: Actuation waveform for all parameter investigations.

Following the analysis of fluid properties, the investigation also encompasses the variation of the contact angle and its influence on the droplet formation.

Density

The density of a liquid plays a role in the droplet formation process. Changing the density of the liquid has a proportional effect on the inertia forces during the jetting. Inertial forces act as a resistance against the contraction of the liquid jet due to surface tension and influence the velocity of the droplet. To investigate the possible effects of different density values, ρ has been varied between 950 and 1100 kg/m^3.

Figure 5.12 shows the results of different droplet simulations at a time-step of 20 μs. The velocity of the head droplets is visibly influenced, while the position of the tail droplet stays nearly constant across the different fluids. All tails are either experiencing a front pinch-off at the head droplet around this time-step or are about to. This leads to a slightly longer tail for fluids with a lower density. Since the tail breaks up almost at the same time for all simulations, this would result in a slightly bigger satellite droplet for fluids with a lower density.

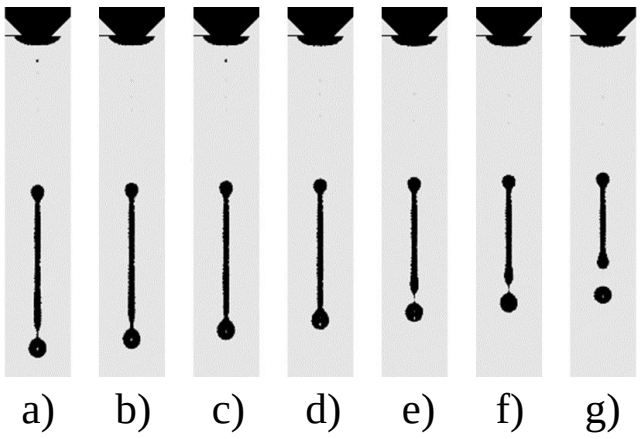

Figure 5.12: Droplet simulation with different densities 950, 975, .., 1100 kg/m^3. All scenes are taken at a simulated time of 20 μs.

When observing the distance of the head droplet to the nozzle in relation to the time (Figure 5.13), a slight change in the trajectory can be observed. The initial motion of the meniscus sees almost no influence. The difference between the fluids develops over time based on the difference in velocity.

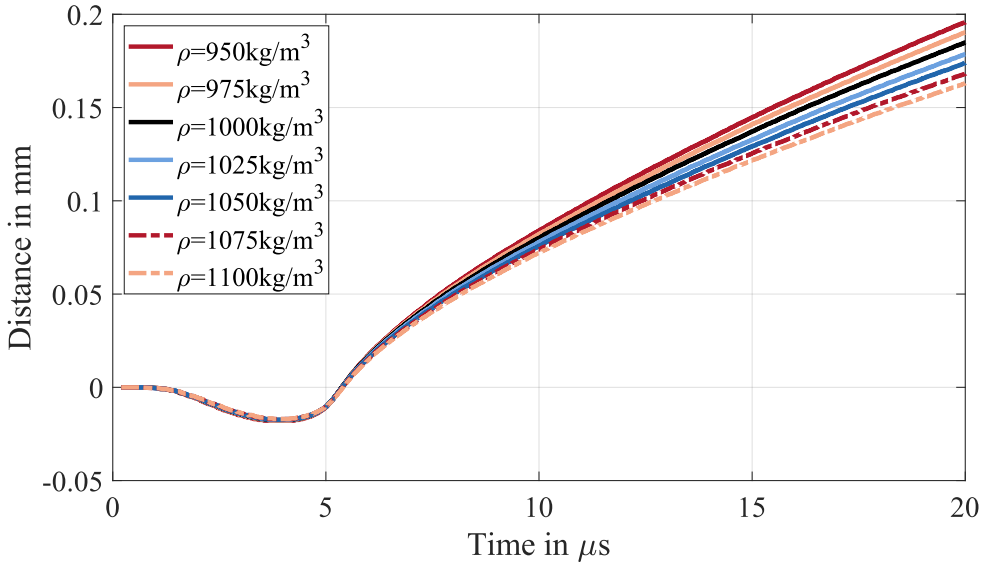

Figure 5.13: Distance (x_h) of the head droplet over time for different fluid densities.

To further analyse these results, characteristic properties for the droplet formation are shown in Figure 5.14. It can be seen that the pinch-off time (a) is only slightly influenced by different density values, explaining to a certain extent the constant position of the tail droplets across the different simulations. The maximum ejection velocity (d) and the droplet velocity after 20 μs is, however, decreasing linearly with increasing density. The volume of the droplet also shows a slight linear decrease with increasing density (c).

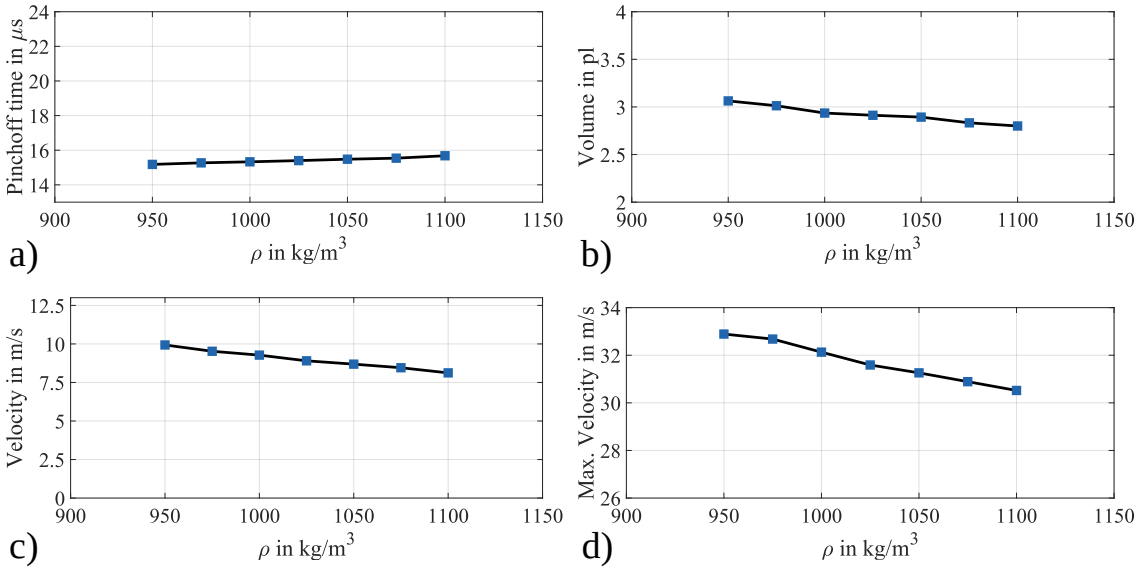

Figure 5.14: Important characteristics at different fluid densities: a) Development of the pinch-off time b) Development of the ejected fluid at the end of the simulation c) Development of the average droplet velocity between 15 and 20 μs after actuation start d) Development of the maximum head droplet velocity during jetting.

The effect of different densities on the droplet formation is only minimal. It can, however, be observed that a lower density results in a faster droplet velocity while simultaneously increasing the tail length.

Viscosity

The fluid viscosity is one of the key parameters during the droplet formation process. A fluid with a higher viscosity needs more energy in order to be ejected since the viscosity of the fluid is a measure of its resistance to deformation. To investigate the extent of the effect on the jetting process, five different viscosities are simulated. The dynamic viscosity η has been varied from 2 cP up to 10 cP, which is a typical viscosity range for usable fluids of the Samba printhead (FUJIFILM 2024). According to the data sheet of the printhead, a viscosity between 4 and 9 cP is recommended, so this investigation exceeds these limits slightly.

Figure 5.15 shows the results of different droplet simulations at a time-step of 20 μs. Both the droplet velocity and the tail breakup are significantly influenced by the viscosity. A lower viscosity leads to an increased speed, which also results into a faster tail breakup and, therefore, satellite formation. This is according to the prediction of the Ohnesorge plot, as a lower viscosity leads to a lower Oh value.

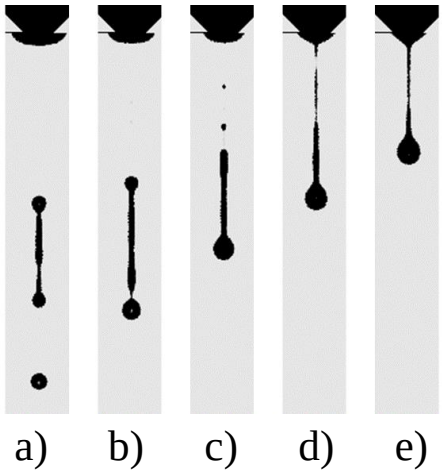

Figure 5.15: Droplet simulation with different viscosities 2, 4, .., 10 cP. All scenes are taken at a simulated time of 20 μs.

When examining the position of the head droplet over time, the impact of a change in viscosity on velocity becomes evident. It can also be observed that the meniscus retracts further into the nozzle with lower viscosity and leaves the nozzle slightly later with a higher speed.

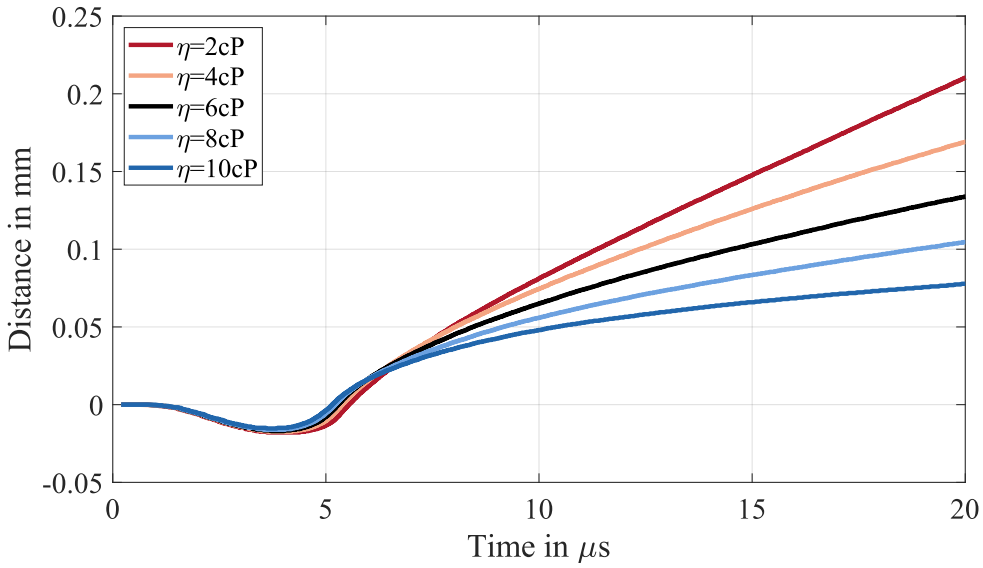

Figure 5.16: Distance (x_h) of the head droplet over time for different fluid viscosities.

Again, a deeper investigation of essential parameters can give information about the droplet formation behaviour (see Figure 5.17).The pinch-off time of the droplet is delayed linearly with an increase in viscosity to a significant extent (a). The volume of the final droplet, however, sees an almost exponential decrease with higher viscosity (b). Both final droplet velocity and maximum jetting velocity decrease significantly (c,d).

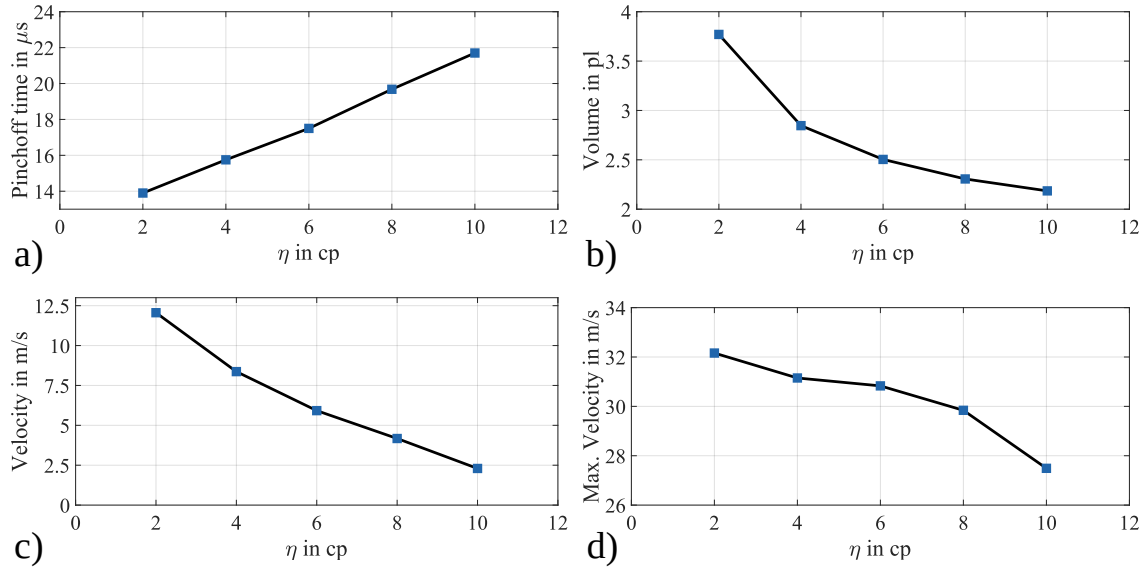

Figure 5.17: Important characteristics at different fluid viscosities: a) Development of the pinch-off time b) Development of the ejected fluid at the end of the simulation c) Development of the average droplet velocity between 15 and 20 μs after actuation start d) Development of the maximum head droplet velocity during jetting.

As could be observed from this investigation, slight changes in the viscosity have a significant impact on a variety of different aspects of the droplet formation process. Since the viscosity is highly dependent on the temperature ($\eta(25°C) = 4.41$ cP and $\eta(30°C) = 3.44$ cP for M_{50}), slight temperature fluctuations can have a strong impact on the droplet behaviour. The heating of the fluid to a constant temperature between different experiments is, therefore, essential to guarantee comparability and the correct droplet formation in the final printhead application.

Surface Tension

The surface tension of the fluid has an impact on the droplet formation. A higher surface tension leads to an increase of cohesive forces between molecules, favouring the minimization of surface area. This leads to a stronger tendency to form spherical droplets. To investigate this effect for the given application, the surface tension is varied between 20 and 60 mN/m.

Figure 5.18 shows the results of different droplet simulations at a time-step of 20 μs. A slight change in velocity can be observed. Additionally, a stronger tendency for a pinch-off can be noted, both at the meniscus and at the head droplet. The tail, therefore, shows a different behaviour as well, depending on the surface tension. The higher change for satellite droplet that results from this behaviour is according the the assumption of the Ohnesorge plot, as a higher surface tension leads to a lower Oh value.

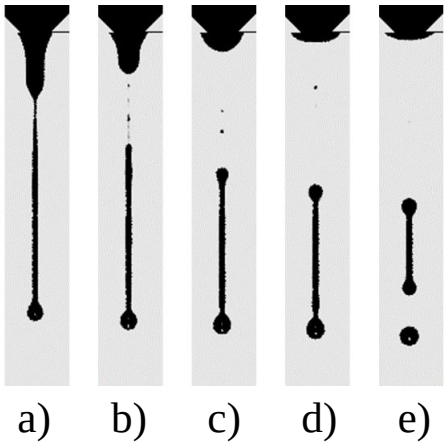

Figure 5.18: Droplet simulation with different surface tensions 20, 30, .., 60 mN/m. All scenes are taken at a simulated time of 20 μs.

Observing the position of the droplet over time (see Figure 5.19) shows a slight delay in the meniscus movement before the fluid leaves the nozzle. The slight change in the final droplet position seems to be mostly resulting from this delay, as the further trajectory follows a similar trend between all simulations without any major influence on the velocity.

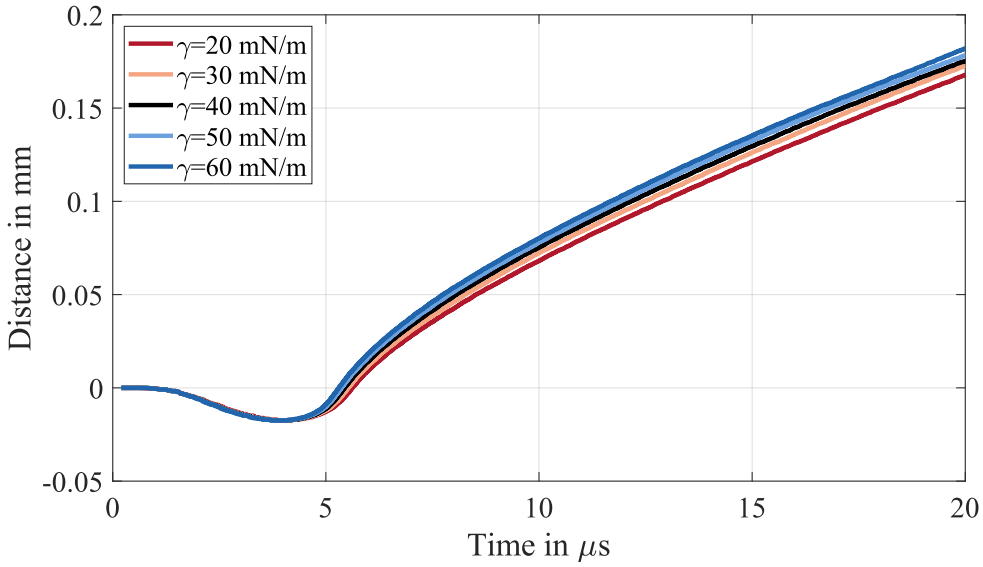

Figure 5.19: Distance (x_h) of the head droplet over time for different surface tensions.

This becomes evident when examining the properties of droplet formation (see Figure 5.20). The final droplet speed and the droplet volume are not affected by the surface tension and remain nearly constant throughout all simulations (a,b). However, a clear difference in the pinch-off time can be noted, which strongly decreases with an increase in surface tension (c). The earlier thinning and pinch-off of the tail could be seen as a reason for the higher jetting velocity that is observed (d).

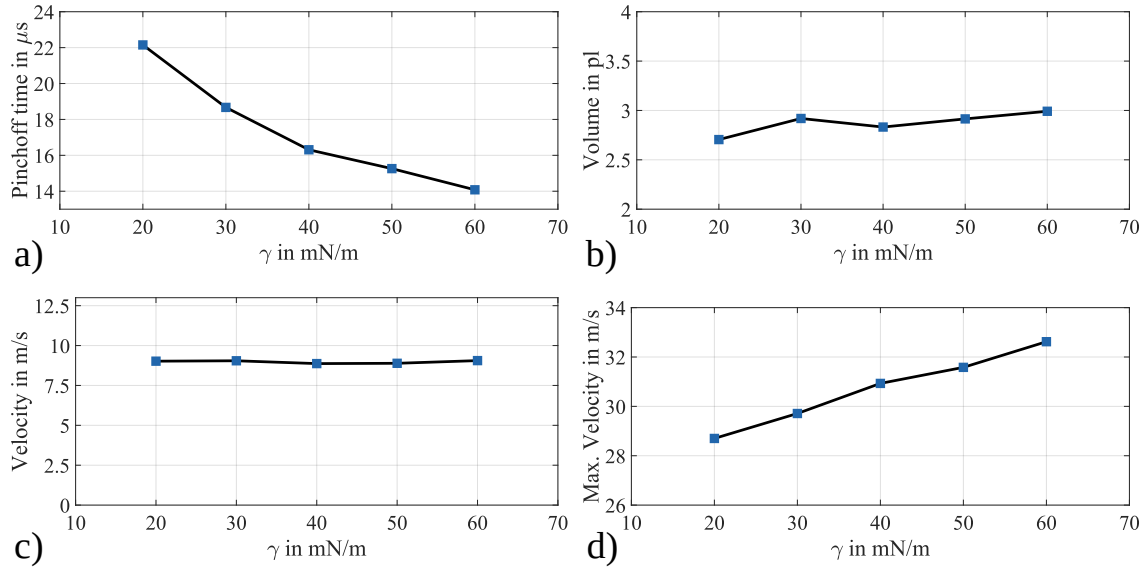

Figure 5.20: Important characteristics at different surface tensions: a) Development of the pinch-off time b) Development of the ejected fluid at the end of the simulation c) Development of the average droplet velocity between 15 and 20 μs after actuation start d) Development of the maximum head droplet velocity during jetting.

The effect of a change in surface tension follows the expectations. An increase in surface tension leads to a faster pinch-off, but also increases the tendency of the tail to break up into several satellite droplets. An optimal value is high enough to promote an early pinch-off to increase the velocity and minimise the tail length and low enough to prohibit the immediate breakup of the tail into satellite droplets.

Contact Angle

The contact angle at the fluid-surface interface influences how the fluid behaves when moving along the nozzle. This can influence the velocity and the breakup of the tail, as has been shown by several articles (Zhang et al. 2022, B. He et al. 2017). A contact angle below 90 deg leads to wetting (hydrophilic) behaviour, while a contact angle above 90 deg results in a non-wetting (hydrophobic) behaviour. To investigate the effect on the current model and waveform, five different contact angles are applied to the nozzle wall and nozzle plate.

Figure 5.21 shows the results of different droplet simulations at a time-step of 20 μs. The tail droplet stays in the same position across all simulations. The velocity of the head droplet starts to decrease for a contact angle higher than 90 deg. At low contact angles, almost no difference is noticeable at this time-step. Only the meniscus shows a clear difference in contact angle across all simulations.

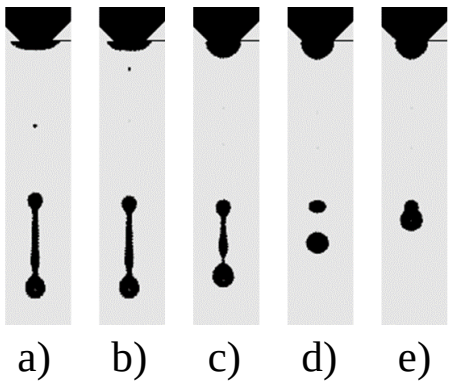

Figure 5.21: Droplet simulation with different contact angles 10, 45, 90, 135, and 170 deg. All scenes are taken at a simulated time of 20 μs.

When looking at the distance of the droplet over time (Figure 5.22), still no significant impact across the low contact angles can be seen. With an increase in the contact angle, a strong velocity decrease can be observed when leaving the wetting regime.

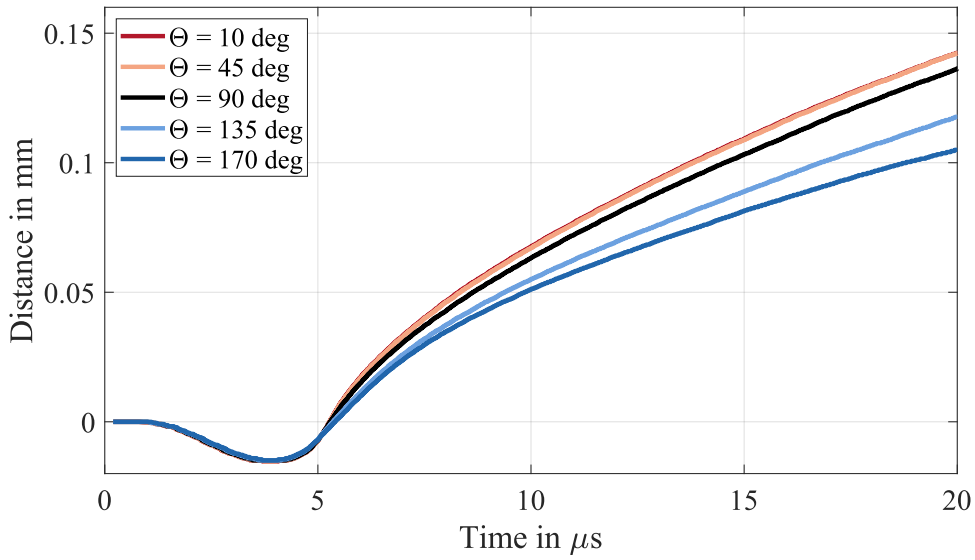

Figure 5.22: Distance (x_h) of the head droplet over time for different contact angles.

When observing the droplet formation properties in Figure 5.23, the clear impact for higher contact angles is visible. Both volume and velocity decrease for high contact angles. An effect on the pinch-off could not be shown with the given waveform. This can be explained by the residual vibration of the waveform, leading to a second push of fluid through the nozzle. The pinch-off happens through the retraction of the residual fluid at the meniscus and is less affected by the contact angle at this point (see, for example, Figure 5.24).

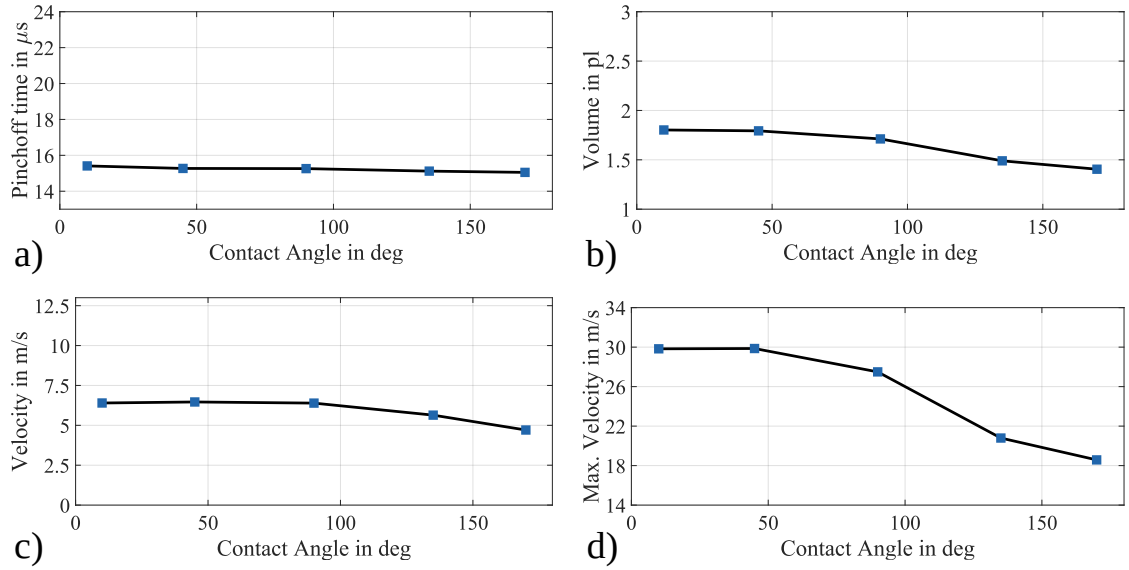

Figure 5.23: Important characteristics at different contact angles: a) Development of the pinch-off time b) Development of the ejected fluid at the end of the simulation c) Development of the average droplet velocity between 15 and 20 μs after actuation start d) Development of the maximum head droplet velocity during jetting.

The effect that the contact angle has on the droplet formation is clearly visible and follows the expectations. An increase in contact angle leads to a reduction in velocity and volume when the wetting regime is left. With an increase in pressure amplitude, the velocities can be matched again to the expected experimental results. This can be used to compare multiple contact angles with the same droplet velocity and compare the results to the experimental values to approximate the contact angle. It can be noted in Figure 5.24 that the effect on the meniscus is especially strong for a hydrophobic contact angle. The meniscus retracts deep into the nozzle, which will effect the following droplet. If only one droplet formation is simulated, it can, therefore, be beneficial to delay the actuation until the meniscus has reached an equilibrium state. In the shown picture, both simulations are calibrated to the same velocity by changing the pressure amplitude. With a contact angle of 170 degrees (a), the meniscus curves back into the nozzle, while with a contact angle of 10 degrees (b), the meniscus remains at the nozzle exit. Also a change in meniscus motion during the droplet formation can be noted, with a differently shaped second push at time-step b.

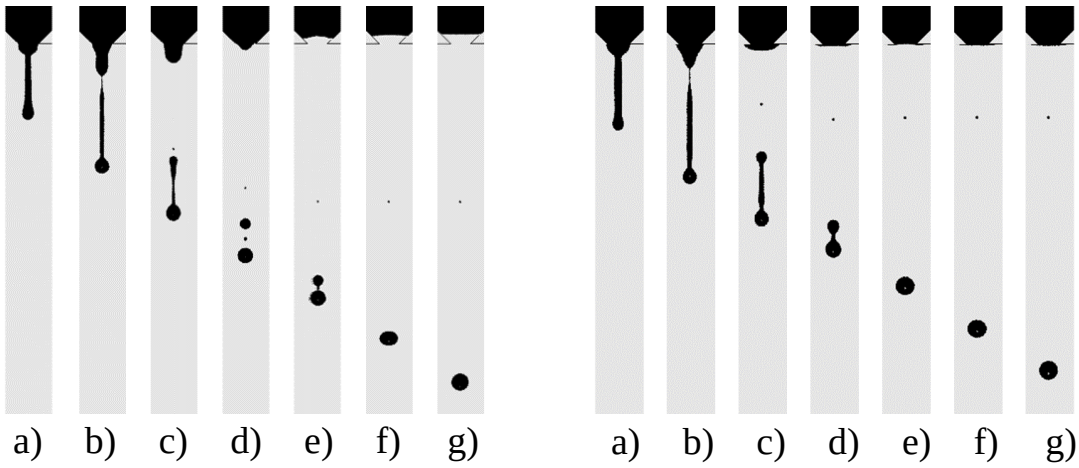

Figure 5.24: Comparison between a simulation with a high contact angle of 170 degrees (a) and a low contact angle of 10 degrees (b). Both simulations aim for an equal droplet velocity. The images are taken at a rate of 5 μs beginning at 10 μs after the actuation.

5.2.2 Multidrop Simulation

When simulating a multi-pulse actuation waveform, it is important to consider potential residual vibrations resulting from sequential actuations. In the observed experiments, it can be noted that the meniscus does not fully retract into the nozzle plate before the next droplet is fired (see Figure 5.25). This can imply that the following droplets are affecting each other at the chosen frequency based on the residual vibration. For all single pulse actuations, the meniscus fully retracts before the next actuation.

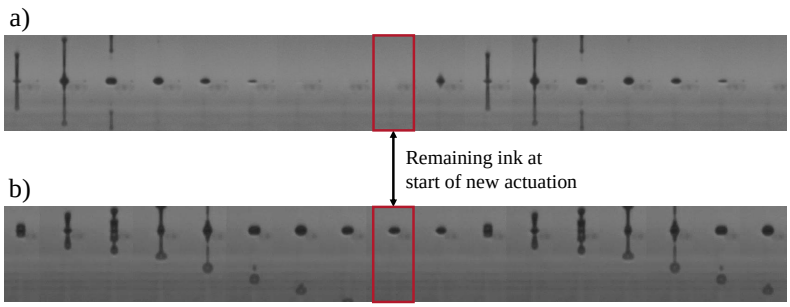

Figure 5.25: Remaining liquid at the nozzle plate: a) single pulse actuation (close up of Figure 4.4) b) multi-pulse actuation (close up of Figure 4.7).

To simulate a possible case with multiple droplets, the complex waveform is repeated four times within the simulation, resulting in four individual droplets. The resulting waveform with the current model is shown in Figure 5.26. A clear overlapping between the separate actuations is visible. The frequency of the actuation is 20 kHz.

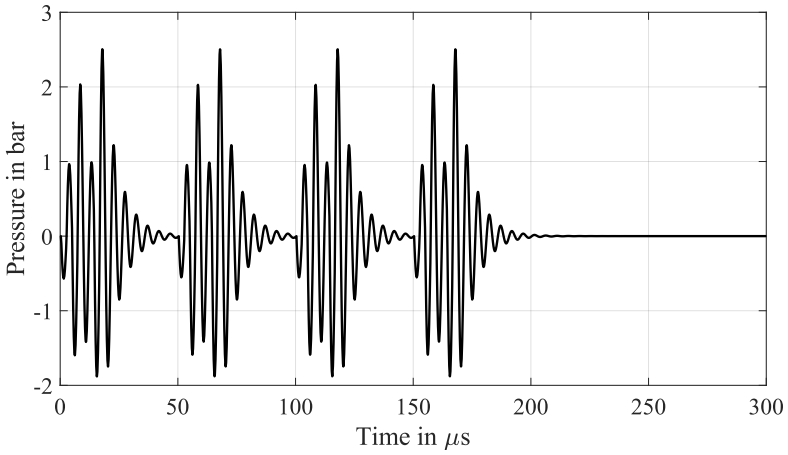

Figure 5.26: Pressure waveform for a multishot simulation with overlapping vibrations between different actuation phases.

When simulating this waveform, a different behaviour between the first droplet and the following droplets can be observed (see Figure 5.27). The first droplet moves with a significantly higher velocity, while the following droplets are slowed down. The difference in the actuation can also be seen in the meniscus movement. When simulating a single droplet, the effect of the previous droplet on the actuation waveform might not be captured. Further analysis in this area could be part of future investigations.

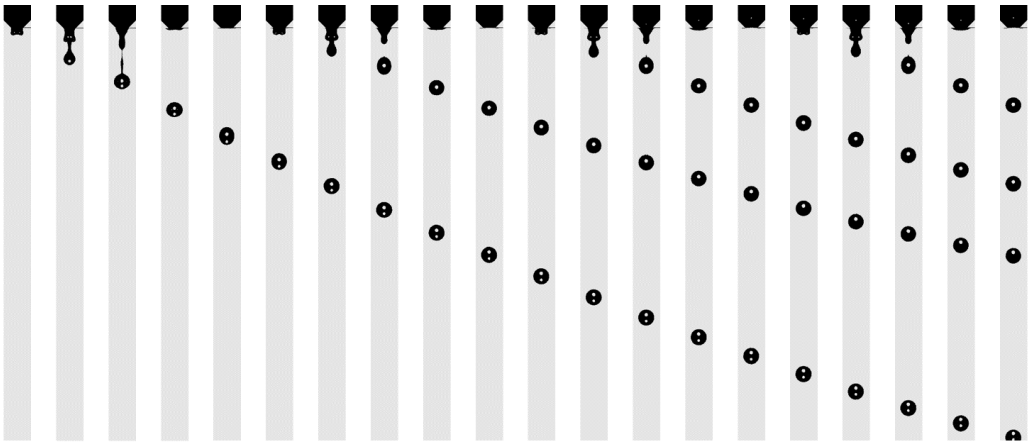

Figure 5.27: Sequential images of the multishot simulation. The images are taken at a rate of 10 μs beginning at 10 μs after the actuation.

Conclusion and Outlook

The goal of this thesis was the creation of a numerical model that can simulate the occurrence of satellite droplets and the investigation of different fluid parameters. The focus was on a printhead with a native droplet size of 2-3 pL, with the additional challenge of limited available data. The project was carried out entirely using the software Star-CCM+. Within this section, the overall results will be summarised, and a future outlook will be presented.

A numerical stand-alone model of the jetting process from a DOD printhead was successfully developed. Multiple axisymmetric mesh sensitivity studies were performed, and a polyhedral mesh was chosen as the most fitting choice regarding consistency of the simulation results. A minimum resolution of 0.4 μm was selected for the given model, providing a resolution that manages to capture the entire droplet formation process. The significance of maintaining mesh consistency across various investigations was noted. The created model could initially be validated with experimental results published by Wijshoff (2008). Numerical simulations managed to capture both velocity and droplet volume based on the chosen inlet boundary condition.

With the validated model, post-processing methods could be implemented, and initial investigations regarding the process and model properties could be conducted. A relationship between the Ohnesorge number of the fluid and the satellite formation could be observed. Additionally, the influence of different inlet boundary conditions was investigated. The results showed a linear relationship between waveform amplitude/oscillation period and the final droplet velocity.

Experimental tests with a Samba printhead were performed and analysed. Two Newtonian fluids, based on a mixture of 1.2 propandiol and water, were chosen for the experimental investigation. The percentages of 1.2 propandiol were 50 % and 25 %, respectively. The conducted tests involved a sweep across multiple voltage amplitudes and pulse width for a single trapezoidal input signal to the piezoelectric actor. Additionally, a M-shaped waveform consisting of two separate voltage pulses and a complex waveform consisting of three individual voltage pulses were tested on the different fluid.

For the stand-alone model, an approximation method for the inlet boundary condition was developed, based on the experimental results. This simple analytical model was based on the resonance behaviour of the printhead and the fluid and was created based on the limited available data. The approximation method uses the natural response of a resonance circuit to approximate a pressure waveform in the ink cham-

ber. Based on a provided calibration method, this method could be validated with several experimental comparisons for single pulse actuations. Additionally, multi-pulse waveforms and multi-shot jetting were investigated. The model managed to capture the general formation of the multi-pulse droplets while deviating slightly regarding final velocity. A strong effect on sequential droplet formations was observed when simulating a multi-shot jetting process, highlighting the importance of the consideration of residual vibrations and the initial meniscus position.

Different ink properties have been investigated and their influence on jetting behaviour has been analysed. An increase in density showed a reduction in jetting velocity and droplet volume while slightly delaying the time of pinch-off. A change in viscosity showed a strong influence on the droplet velocity and volume, as well as the pinch-off timing. Both velocity and volume greatly decrease with an increase in viscosity while the pinch-off time is delayed. An increase in surface tension showed a faster pinch-off and an increase in maximum jetting velocity while only slightly affecting the droplet volume and final velocity. For the given printhead, a change in contact angle only affected the droplet formation when reaching a non-wetting behaviour. An increase in contact angle resulted in a decrease in velocity and volume. The effects of viscosity are considered the most influential, given the strong fluctuation of ink viscosity depending on temperature changes.

One of the future outlooks with the current model involves further exploring the influence of waveform parameters on droplet jetting behaviour, as well as comparing numerical predictions with experimental observations. A more extensive and controlled experimental study regarding pulse width effects or ink parameters could help to improve the model calibration and investigate the observed differences. This could include the possible consideration of the refill resonance circuit or different model changes regarding β or ζ. With a deeper circuit representation, the response of the model could also be adjusted towards a ramp function in contrast to a step response.

The current model can further be used to investigate several process and parameter effects that could not be extensively considered in this thesis. The implemented post-processing methods allow for multiple possible future investigations in several areas, like model parameters, nozzle geometries, or fluid/air properties. These could explore, for example, multi-shot behaviour, jetting frequencies, contact angle effects, or multi-pulse actuations. Moreover, additional enhancements to the model can be incorporated to simulate further production steps of interest, such as the impingement of droplets on the substrate or the influence of air drafts on the trajectory. Transferring the gained knowledge to a three-dimensional model could furthermore increase the accuracy by considering the square nozzle shape of the actual printhead. A comparison between the axisymmetric and three-dimensional models can assess the extent of differences between the actual geometry and the simplified axisymmetric representation.

Ultimately, an extensive analysis of the printhead and the internal flow characteristics with FEM simulations or frequency analysis techniques can lead to more advanced boundary conditions for the stand-alone model. The implementation of

FSI or LEM approaches could help to further understand the internal resonances and simulate the droplet formation with higher precision.

Since the current model is only tested on Newtonian fluids, an additional enhancement towards non-Newtonian fluids with polymer contents is part of future investigations. This would ultimately lead to a better understanding of the behaviour of real inks but requires precise knowledge about boundary conditions and the necessary fluid models within the selected software.

Appendix

Advanced Waveform Approximation Methods

Within this section a short overview over different waveform approximation methods is provided.

Finite-Element-Method

Three-dimensional finite element models build the base for most waveform propagation investigations. Two coupled models are required to simulate the process. Firstly, a computational model for the electromechanical actuation is required to simulate the deformation of the piezoelectric actuator based on the electrical input signal. Secondly, a fluid-structure interaction (FSI) model is needed to simulate the mechanical-acoustic coupling and the pressure wave propagation. Coupling both models can be achieved via a moving mesh as the piezo membrane (Nguyen, Leong, et al. 2021). A method for the electromechanical coupling has been presented and validated by Nguyen, Kumar, and Leong 2018.
In the fluid-structure interaction, the structural velocity of the deforming actuator can be transmitted to the fluid with a moving mesh. Both Wei et al. (2017) and Shah, D.-G. Lee, and Hur (2019) use this method for a waveform simulation using the software COMSOL.

Narrow-Channel-Model

The narrow channel theory has previously been used by Wijshoff 2008 to predict the pressure waveform at the nozzle inlet. In his approach, the governing equations of the narrow channel acoustics are derived based on viscothermal wave propagation theory. This leads to the narrow channel equation for the pressure, defined as:

$$B\frac{\partial^2 p}{\partial x^2} + \left(\frac{\omega^2}{c_0} + \rho_0\omega^2\beta\right)p = -\rho_0\omega^2\alpha U \tag{A.1}$$

where B is the frequency-dependent velocity profile of the wave, which is depending on the geometry and fluid viscosity, and α and β are the specific electrical and pressure compliances. FEM models are used for parameter calculations (B, α, β, etc.). Finally, a solution in the frequency domain is derived, which can be transformed back into the time domain. Another approach that involves the use of frequency analysis has been proposed by B.-H. Kim, S.-I. Kim, et al. (2012), who calculated the pulse width based in the Helmholtz resonance frequency.

Lumped-Element-Model

A lumped-element model (LEM) is a simplification of a physical system or circuit that reduces every component of the system into a concentrated point that can be described by idealized mathematical models. In a LEM, every mechanical component of a system is represented by an equivalent electrical element. This enables the connection of different physical systems.
In the application of an inkjet printhead, an electrical signal is used to generate a mechanical displacement. The mechanical energy is then converted to fluidic/acoustic energy in the fluid chamber and finally to kinetic energy when the droplet leaves the nozzle. To represent these systems in an equivalent circuit, an analogy between electrical circuit and fluidic circuit can be made. In this analogy, the electric current (i) and the voltage (V) are equivalent to the volumetric flow rate (Q) and pressure difference, respectively. The electric capacitance, inductance and resistance are analogous to the fluidic compliance (C) in $[m^3/Pa]$, inductance (L) in $[kg/m^4]$ and resistance (R) in $[Pas/m^3]$, respectively.
A general equivalent circuit with these analogies is presented in Figure A.1. Similar circuits have been used by many researchers to simulate push-printheads (Nguyen, Leong, et al. 2021, Shah, D.-G. Lee, and Hur 2019, Yoshida, Izumi, and Tokito 2019, B.-H. Kim, H.-S. Lee, et al. 2014, Gallas et al. 2003) or squeeze-printheads (M. He et al. 2014, Wang, Huang, and Peng 2019).

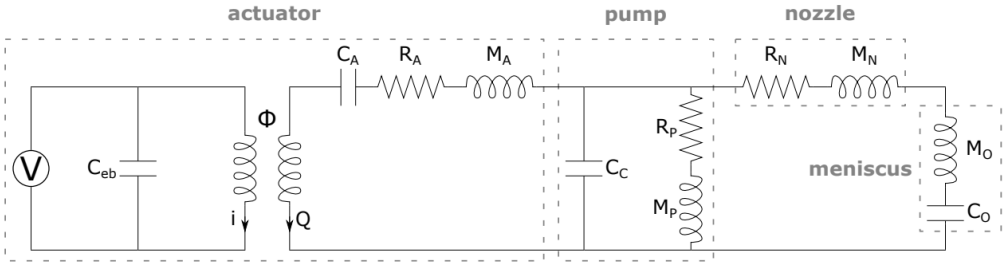

Figure A.1: Simple equivalent electrical circuit representation of an inkjet system, based on (Nguyen, Leong, et al. 2021).

The acquisition of the needed parameters for the successful simulation of the system can be achieved using different assumptions and numerical methods. Some parameters can be approximated with analytical expressions, while others require FEM simulations.
In the given example, the actuator is used as a connection between the electric and fluidic circuit, following earlier work of Nguyen, Leong, et al. 2021 and Gallas et al. 2003. The electric circuit consists of a voltage source (V) and the blocked electrical capacitance (C_{eb}). The connection between the electrical domain and the fluidic domain is represented by an ideal transformer. The coupling factor ϕ, is the ratio of effective acoustic piezoelectric coefficient (d_A) and the short circuit acoustic compliance of the actuator (Prasad et al. 2002):

$$\phi = \frac{d_A}{C_A} \tag{A.2}$$

The inductive terms of the fluid within the pressure channel and the nozzle can be written as:

$$L_i = \left(\frac{\rho l}{A}\right)_i, i = P, N \tag{A.3}$$

where l is the length of the channel and A the cross-sectional area. The hydrolic resistance terms are defined as the pressure difference ΔP divided by the volume flow rate Q. To approximate these terms with a complex geometry, a FEM simulation can be used.

$$R_i = \left(\frac{\Delta P}{Q}\right)_i, i = P, N \tag{A.4}$$

The capacitive term of the fluid within the pressure channel can be written as:

$$C_p = \frac{V_p}{\rho c^2} \tag{A.5}$$

where V is the volume, ρ the density and c the speed of sound in the ink.

At the nozzle exit, a meniscus is formed between the air and fluid due to surface tension. The fluid within the meniscus is represented by the compliance term C_{ms} and can be derived by:

$$C_{ms} = \frac{\pi r_n^4}{3\sigma} \tag{A.6}$$

With all the needed LEM parameters, a state space model can be derived, as shown by Shah, D.-G. Lee, and Hur (2019). They created multiple state variables to represent the different volumetric flow rates and pressure differences to create the state equations of a linear time-varying system of the form:

$$\dot{x}(t) = Ax(t) + Bu(t) \tag{A.7}$$

$$y(t) = Cx(t) + D \tag{A.8}$$

Solving these equations with a given voltage waveform u(t) enables the quick calculation of the pressure and flow rate at different parts of the printhead. With more experimental investigations and detailed data on the printhead in use, a model like this can lead to a fast approximation of the inlet condition to a stand-alone jetting model.

Additional Plots

Detailed Waveform Approximations

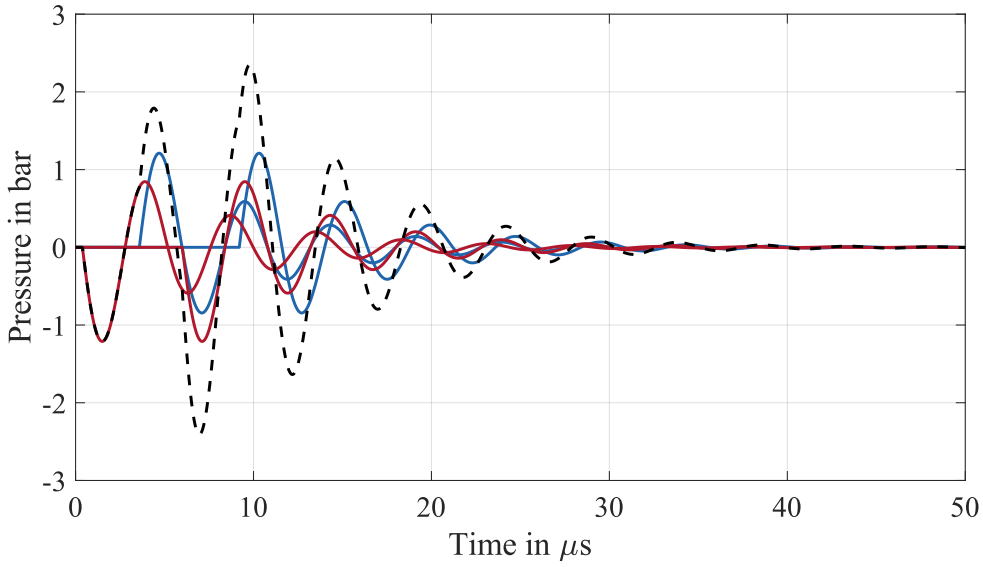

Figure A.2: Individual pull and push waves for the M-shaped waveform shown in Figure 5.7.a

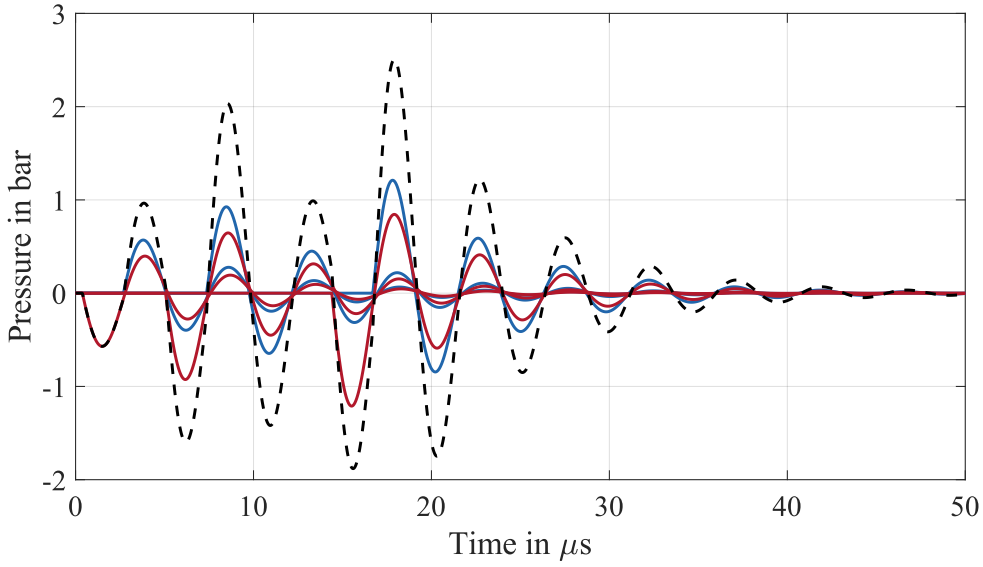

Figure A.3: Individual pull and push waves for the complex waveform shown in Figure 5.7.b

Time-Step Evolution

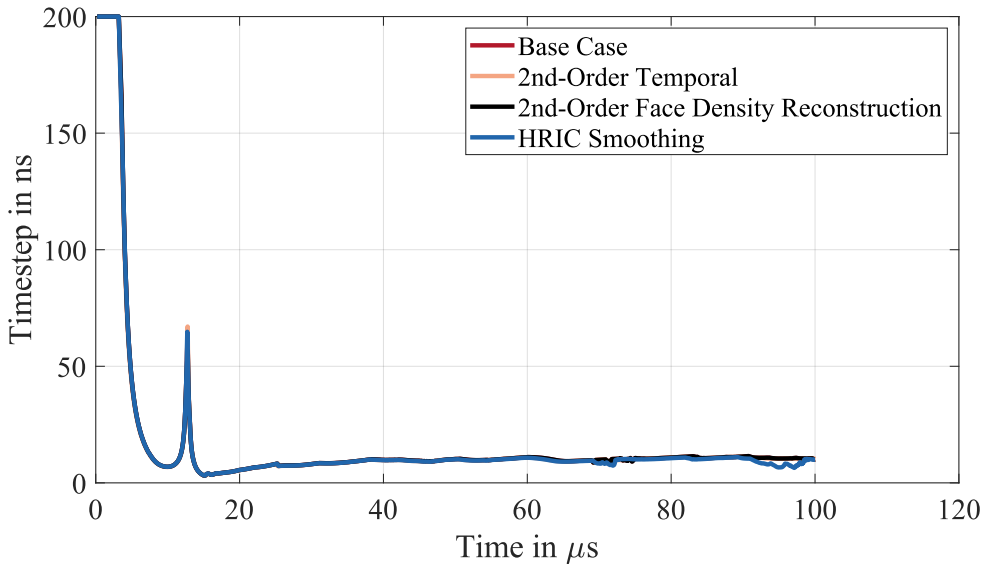

Figure A.4: Comparison of the time-step size throughout the simulations for different model parameters.

Velocity Vector Field

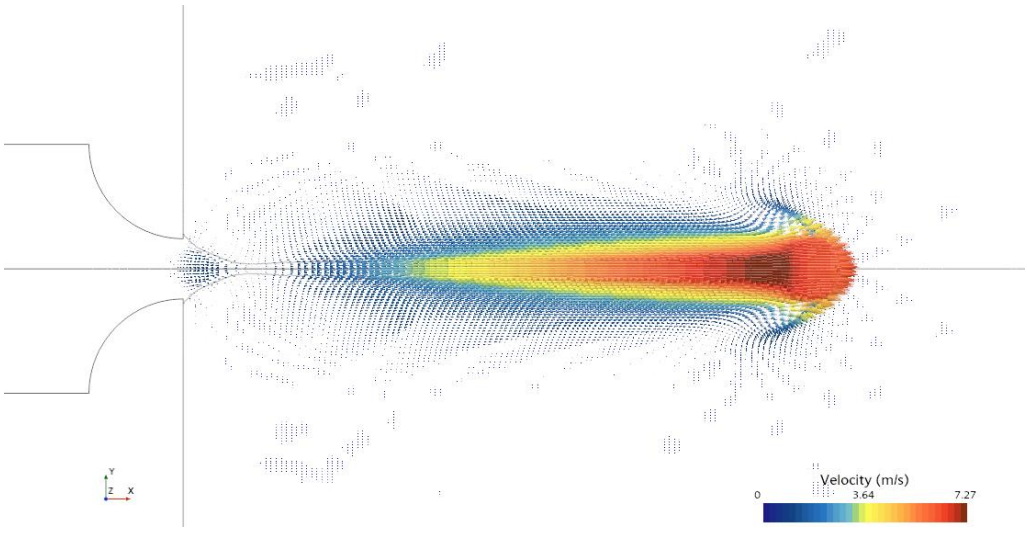

Figure A.5: Velocity vector field of the domain.

Simulation Overviews

Simulation Overview Part 1

Simulation Overview: Chapter 3.3 & 3.4					
Geometry		**Mesh**		**Phases**	
Nozzle Diameter:	24 μm	Type:	**Varied**	Air:	Ideal Gas
Nozzle Shape:	45 deg. with 30 μm throat	Resolution:	**Varied**	Fluid:	Newtonian Fluid
		No. of Cells:	**Varied**	Interaction:	Semi-implicit Surface Tension
Pressure Chamber:	100x200 μm				
Ink Properties				**Boundary Conditions**	
Viscosity (η):	0.007 Pas			Inlet:	Velocity Inlet (Fig. 3.4)
Density (ρ):	1050 kg/m^3			Outlet:	Pressure Outlet
Surface Tension (γ):	0.072 N/m			Nozzle Wall:	No-Slip with Θ_{eq} = 45 deg.
Solver Settings					
Temporal Discretization:	1st order Implicit Unsteady			Timestep Control:	Free Surface CFL <= 0.4
Pressure-Velocity Coupling:	SIMPLE (segregated flow)			Convection Scheme:	HRIC
VOF solver:	Implicit Multi Step (5 steps)			Face Density Reconstruction:	1st order
Simulation Overview: Chapter 3.5 & 3.6.1 (besides Figure 3.24) & 3.6.4					
Geometry		**Mesh**		**Phases**	
Nozzle Diameter:	32 μm	Type:	Polyhedral	Air:	Ideal Gas
Nozzle Shape:	Rounded	Resolution:	0.4 μm	Fluid:	Newtonian Fluid
Pressure Chamber:	300x132 μm	No. of Cells:	325354	Interaction:	Semi-implicit Surface Tension
Ink Properties				**Boundary Conditions**	
Viscosity (η):	0.01 Pas			Inlet:	Pressure Inlet (Fig. 3.18 & 3.29)
Density (ρ):	1000 kg/m^3			Outlet:	Pressure Outlet
Surface Tension (γ):	0.03 N/m			Nozzle Wall:	No-Slip with Θ_{eq} = 20 deg.
Solver Settings					
Temporal Discretization:	1st order Implicit Unsteady			Timestep Control:	Free Surface CFL <= 0.4
Pressure-Velocity Coupling:	SIMPLE (segregated flow)			Convection Scheme:	HRIC
VOF solver:	Implicit Multi Step (5 steps)			Face Density Reconstruction:	1st order
Simulation Overview: Chapter 3.6.3					
Geometry		**Mesh**		**Phases**	
Nozzle Diameter:	32 μm	Type:	Polyhedral	Air:	Ideal Gas
Nozzle Shape:	Rounded	Resolution:	0.4 μm	Fluid:	Newtonian Fluid
Pressure Chamber:	300x132 μm	No. of Cells:	325354	Interaction:	Semi-implicit Surface Tension
Ink Properties				**Boundary Conditions**	
Viscosity (η):	**Varied**			Inlet:	Pressure Inlet (Fig. 3.18)
Density (ρ):	**Varied**			Outlet:	Pressure Outlet
Surface Tension (γ):	**Varied**			Nozzle Wall:	No-Slip with Θ_{eq} = 20 deg
Solver Settings					
Temporal Discretization:	1st order Implicit Unsteady			Timestep Control:	Free Surface CFL <= 0.4
Pressure-Velocity Coupling:	SIMPLE (segregated flow)			Convection Scheme:	HRIC
VOF solver:	Implicit Multi Step (5 steps)			Face Density Reconstruction:	1st order

Simulation Overview Part 2

Simulation Overview: Chapter 4.2.3					
Geometry		**Mesh**		**Phases**	
Nozzle Diameter:	17 μm	Type:	Polyhedral	Air:	Ideal Gas
Nozzle Shape:	Angled with 45 deg.	Resolution:	0.4 μm	Fluid:	Newtonian Fluid
		No. of Cells:	175336	Interaction:	Semi-implicit Surface Tension
Pressure Chamber:	400x150 μm				
Ink Properties		**Boundary Conditions**			
Viscosity (η):	0.0037 Pas	Inlet:	Pressure Inlet (Fig. 4.14, 4.17, 4.19)		
Density (ρ):	1030 kg/m^3	Outlet:	Pressure Outlet		
Surface Tension (γ):	0.04811 N/m	Nozzle Wall:	No-Slip with Θ_{eq} = 20 deg		
Solver Settings					
Temporal Discretization:	1st order Implicit Unsteady			Timestep Control:	Free Surface CFL <= 0.4
Pressure-Velocity Coupling:	SIMPLE (segregated flow)			Convection Scheme:	HRIC
VOF solver:	Implicit Multi Step (5 steps)			Face Density Reconstruction:	1st order

Simulation Overview: Chapter 5.1.1 & 5.1.2					
Geometry		**Mesh**		**Phases**	
Nozzle Diameter:	17 μm	Type:	Polyhedral	Air:	Ideal Gas
Nozzle Shape:	Angled with 45 deg.	Resolution:	0.4 μm	Fluid:	Newtonian Fluid
		No. of Cells:	175336	Interaction:	Semi-implicit Surface Tension
Pressure Chamber:	400x150 μm				
Ink Properties		**Boundary Conditions**			
Viscosity (η):	0.0037 Pas	Inlet:	Pressure Inlet (Eq. 4.4, Fig. 5.7)		
Density (ρ):	1030 kg/m^3	Outlet:	Pressure Outlet		
Surface Tension (γ):	0.04811 N/m	Nozzle Wall:	No-Slip with Θ_{eq} = 20 deg		
Solver Settings					
Temporal Discretization:	1st order Implicit Unsteady			Timestep Control:	Free Surface CFL <= 0.4
Fig. 5.5:	2nd order Implicit Unsteady			Convection Scheme:	HRIC
Pressure-Velocity Coupling:	SIMPLE (segregated flow)			Face Density Reconstruction:	1st order
VOF solver:	Implicit Multi Step (5 steps)				
Fig. 5.5:	Single Step				

Simulation Overview: Chapter 5.1.3					
Geometry		**Mesh**		**Phases**	
Nozzle Diameter:	17 μm	Type:	Polyhedral	Air:	Ideal Gas
Nozzle Shape:	Angled with 45 deg.	Resolution:	0.4 μm	Fluid:	Newtonian Fluid
		No. of Cells:	175336	Interaction:	Semi-implicit Surface Tension
Pressure Chamber:	400x150 μm				
Ink Properties		**Boundary Conditions**			
Viscosity (η):	0.0017 Pas	Inlet:	Pressure Inlet (Eq. 4.4)		
Density (ρ):	1013 kg/m^3	Outlet:	Pressure Outlet		
Surface Tension (γ):	0.05462 N/m	Nozzle Wall:	No-Slip with Θ_{eq} = 20 deg		
Solver Settings					
Temporal Discretization:	2nd order Implicit Unsteady			Timestep Control:	Free Surface CFL <= 0.4
Pressure-Velocity Coupling:	SIMPLE (segregated flow)			Convection Scheme:	HRIC
VOF solver:	Single Step			Face Density Reconstruction:	1st order

Simulation Overview Part 3

Simulation Overview: Chapter 5.2.1					
Geometry		**Mesh**		**Phases**	
Nozzle Diameter:	17 μm	Type:	Polyhedral	Air:	Ideal Gas
Nozzle Shape:	Angled with 45 deg.	Resolution:	0.4 μm	Fluid:	Newtonian Fluid
Pressure Chamber:	400x150 μm	No. of Cells:	175336	Interaction:	Semi-implicit Surface Tension
Ink Properties				**Boundary Conditions**	
Viscosity (η):	**varied**			Inlet:	Pressure Inlet (Fig. 5.11)
Density (ρ):	**varied**			Outlet:	Pressure Outlet
Surface Tension (γ):	**varied**			Nozzle Wall:	No-Slip with Θ_{eq} = 20 deg
Solver Settings					
Temporal Discretization:	1st order Implicit Unsteady			Timestep Control:	Free Surface CFL <= 0.4
Pressure-Velocity Coupling:	SIMPLE (segregated flow)			Convection Scheme:	HRIC
VOF solver:	Implicit Multi Step (5 steps)			Face Density Reconstruction:	1st order
Simulation Overview: Chapter 5.2.2					
Geometry		**Mesh**		**Phases**	
Nozzle Diameter:	17 μm	Type:	Polyhedral	Air:	Ideal Gas
Nozzle Shape:	Angled with 45 deg.	Resolution:	0.4 μm	Fluid:	Newtonian Fluid
Pressure Chamber:	400x150 μm	No. of Cells:	175336	Interaction:	Semi-implicit Surface Tension
Ink Properties				**Boundary Conditions**	
Viscosity (η):	0.0037 Pas			Inlet:	Pressure Inlet (Fig. 5.26)
Density (ρ):	1030 kg/m^3			Outlet:	Pressure Outlet
Surface Tension (γ):	0.04811 N/m			Nozzle Wall:	No-Slip with Θ_{eq} = 20 deg
Solver Settings					
Temporal Discretization:	2nd order Implicit Unsteady			Timestep Control:	Free Surface CFL <= 0.4
Pressure-Velocity Coupling:	SIMPLE (segregated flow)			Convection Scheme:	HRIC
VOF solver:	Single Step			Face Density Reconstruction:	1st order

Bibliography

Alves, M. A., P. J. Oliveira, and F. T. Pinho (2021). "Numerical Methods for Viscoelastic Fluid Flows". In: *Annual Review of Fluid Mechanics* 53.1, pp. 509–541. ISSN: 0066-4189 1545-4479. DOI: 10.1146/annurev-fluid-010719-060107.

Bauer, Koenig und (2024). URL: www.koenig-bauer.com.

Castrejon-Pita, J. R. et al. (2011). "Experiments and Lagrangian simulations on the formation of droplets in drop-on-demand mode". In: *Phys Rev E Stat Nonlin Soft Matter Phys* 83.3 Pt 2, p. 036306. ISSN: 1550-2376 (Electronic) 1539-3755 (Linking). DOI: 10.1103/PhysRevE.83.036306. URL: https://www.ncbi.nlm.nih.gov/pubmed/21517586.

Clasen, Christian et al. (2011). "Dispensing of rheologically complex fluids: The map of misery". In: *AIChE Journal* 58.10, pp. 3242–3255. ISSN: 0001-1541 1547-5905. DOI: 10.1002/aic.13704.

Conto, Francesco Paolo (2019). "Breakup of liquid jets: the capillary retraction". PhD thesis. Queen Mary University of London.

Coşar, Veli Can et al. (2023). "A solenoid injector based drop-on-demand system for generating large droplets". In: *Review of Scientific Instruments* 94.9.

Dannenberg, Erik (2022). URL: https://www.reden.nl/our-work/simulating-drop-formation-in-inkjet-printing.

Derby, B (2010). "Inkjet printing of functional and structural materials: fluid property requirements, feature stability, and resolution". In: *Annual Review of Materials Research* 40, pp. 395–414.

Driessen, Theo et al. (2013). "Stability of viscous long liquid filaments". In: *Physics of fluids* 25.6.

Du, Zhonghui, Xinhong Yu, and Yanchun Han (2018). "Inkjet printing of viscoelastic polymer inks". In: *Chinese Chemical Letters* 29.3, pp. 399–404. ISSN: 1001-8417. DOI: 10.1016/j.cclet.2017.09.031. URL: https://www.sciencedirect.com/science/article/pii/S100184171730373X.

Erqiang, Li (2010). *The generation and experimental study of microscale droplets in drop-on-demand inkjet printing.*

Feng, James Q (2002). "A general fluid dynamic analysis of drop ejection in drop-on-demand ink jet devices". In: *Journal of Imaging Science and Technology* 46.5, pp. 398–408.

Fraters, Arjan et al. (2020). "Secondary Tail Formation and Breakup in Piezoacoustic Inkjet Printing: Femtoliter Droplets Captured in Flight". In: *Physical Review Applied* 13.2. ISSN: 2331-7019. DOI: 10.1103/PhysRevApplied.13.024075. URL: https://journals.aps.org/prapplied/abstract/10.1103/PhysRevApplied.13.024075.

FUJIFILM (2024). URL: www.fujifilm.com.

Gallas, Quentin et al. (2003). "Lumped element modeling of piezoelectric-driven synthetic jet actuators". In: *AIAA journal* 41.2, pp. 240–247.

Hamad, Aamir H, Mohammed I Salman, and Ahsan Mian (2020). "Effect of driving waveform on size and velocity of generated droplets of nanosilver ink (Smartink)". In: *Manufacturing Letters* 24, pp. 14–18.

He, B. et al. (2017). "The roles of wettability and surface tension in droplet formation during inkjet printing". In: *Sci Rep* 7.1, p. 11841. DOI: 10.1038/s41598-017-12189-7. URL: https://www.ncbi.nlm.nih.gov/pubmed/28928447.

He, Maowei et al. (2014). "Drop-on-demand inkjet printhead performance enhancement by dynamic lumped element modeling for printable electronics fabrication". In: *Mathematical Problems in Engineering* 2014.

Hoath, Stephen D. (2016). *Fundamentals of Inkjet Printing: The Science of Inkjet and Droplets*. John Wiley and Sons, Incorporated. ISBN: 9783527684731.

Hutchings, Ian M and Graham Dagnall Martin (2013). *Inkjet technology for digital fabrication*. Wiley Online Library.

Jang, Daehwan, Dongjo Kim, and Jooho Moon (2009). "Influence of fluid physical properties on ink-jet printability". In: *Langmuir* 25.5, pp. 2629–2635.

Khattab, Ibrahim S et al. (2017). "Density, viscosity, surface tension, and molar volume of propylene glycol+ water mixtures from 293 to 323 K and correlations by the Jouyban–Acree model". In: *Arabian Journal of Chemistry* 10, S71–S75.

Kim, Byung-Hun, Sang-Il Kim, et al. (2012). "Dynamic characteristics of a piezoelectric driven inkjet printhead fabricated using MEMS technology". In: *Sensors and Actuators A: Physical* 173.1, pp. 244–253.

Kim, Byung-Hun, Hwa-Sun Lee, et al. (2014). "Hydrodynamic responses of a piezoelectric driven MEMS inkjet print-head". In: *Sensors and Actuators A: Physical* 210, pp. 131–140.

Lei, T., J. Han, and H. Liu (2022). "Numerical Analysis and Optimal CFD Model Verification of Piezoelectric Inkjet Printhead". In: *Journal of Applied Fluid Mechanics* 15.4. ISSN: 1735-3572. DOI: 10.47176/jafm.15.04.33396. URL: https://www.jafmonline.net/article_2051.html.

Liu, Yuanyuan and Brian Derby (2019). "Experimental study of the parameters for stable drop-on-demand inkjet performance". In: *Physics of Fluids* 31.3. ISSN: 1070-6631 1089-7666. DOI: 10.1063/1.5085868.

Lohse, Detlef (2022). "Fundamental Fluid Dynamics Challenges in Inkjet Printing". In: *Annual Review of Fluid Mechanics* 54.1. ISSN: 0066-4189. DOI: 10.1146/annurev-fluid-022321-114001. URL: https://www.annualreviews.org/doi/abs/10.1146/annurev-fluid-022321-114001.

Meulen, Mark-Jan van der (2015). "Meniscus motion and drop formation in inkjet printing". In.

Morrison, Neil F. and Oliver G. Harlen (2010). "Viscoelasticity in inkjet printing". In: *Rheologica Acta* 49.6, pp. 619–632. ISSN: 0035-4511. DOI: 10.1007/s00397-009-0419-z.

Nguyen, Vinh-Tan, Pankaj Kumar, and Jason Yu Chuan Leong (2018). "Finite element modellingand simulations of piezoelectric actuators responses with uncertainty quantification". In: *Computation* 6.4, p. 60.

Nguyen, Vinh-Tan, Jason Yu Chuan Leong, et al. (2021). "A multi-fidelity model for simulations and sensitivity analysis of piezoelectric inkjet printheads". In: *Micromachines* 12.9, p. 1038.

Oktavianty, Oke et al. (2019). "New actuation waveform design of DoD inkjet printer for single and multi-drop ejection method". In: *Additive Manufacturing* 25, pp. 522–531.

Plonus, Martin (2020). *Electronics and communications for scientists and engineers*. Butterworth-Heinemann.

Prasad, Suryanarayana et al. (2002). "Two-port electroacoustic model of a piezoelectric circular composite plate". In: *43rd AIAA/ASME/ASCE/AHS/ASC Structures, Structural Dynamics, and Materials Conference*, p. 1365.

Reis, N and B Derby (2000). "Ink jet deposition of ceramic suspensions: Modeling and experiments of droplet formation". In: *MRS Online Proceedings Library (OPL)* 625, p. 117.

Seerden, Kitty AM et al. (2001). "Ink-jet printing of wax-based alumina suspensions". In: *Journal of the American Ceramic Society* 84.11, pp. 2514–2520.

Shah, Muhammad Ali, Duck-Gyu Lee, and Shin Hur (2019). "Design and characteristic analysis of a MEMS piezo-driven recirculating inkjet printhead using lumped element modeling". In: *Micromachines* 10.11, p. 757.

Shah, Muhammad Ali, Duck-Gyu Lee, Bo-Yeon Lee, et al. (2021). "Classifications and Applications of Inkjet Printing Technology: A Review". In: *IEEE Access* 9, pp. 140079–140102. ISSN: 2169-3536. DOI: 10.1109/access.2021.3119219.

Siemens (2024). *StarCCM+ Documentation*. URL: www.siemens.com.

Staat, Hendrik JJ et al. (2017). "Ultrafast imaging method to measure surface tension and viscosity of inkjet-printed droplets in flight". In: *Experiments in fluids* 58, pp. 1–8.

Tai, Jiayan et al. (2008). "Control of droplet formation in inkjet printing using Ohnesorge number category: materials and processes". In: *2008 10th Electronics packaging technology conference*. IEEE, pp. 761–766.

Technote, MicroFab (1999). *99-02.," Fluid Properties Effects on Ink-Jet Device Performance*.

Tofan, Tim et al. (2022). "Modeling 3D Droplet Movement Using a Drop-on-Demand Inkjet Printhead Model". In: *Processes* 10.8. ISSN: 2227-9717. DOI: 10.3390/pr10081467.

Wang, Jianjun, Jin Huang, and Ju Peng (2019). "Hydrodynamic response model of a piezoelectric inkjet print-head". In: *Sensors and Actuators A: Physical* 285, pp. 50–58.

Wei, Hongfang et al. (2017). "A waveform design method for high DPI piezoelectric inkjet print-head based on numerical simulation". In: *Microsystem Technologies* 23, pp. 5365–5373.

Wijshoff, Herman (2008). "Structure- and fluid-dynamics in piezo inkjet printheads". PhD thesis.

Yang, Qiang et al. (2017). "Rayleigh instability-assisted satellite droplets elimination in inkjet printing". In: *ACS applied materials & interfaces* 9.47, pp. 41521–41528.

Yoshida, Yasunori, Konami Izumi, and Shizuo Tokito (2019). "A push-mode piezo inkjet equivalent circuit model enhanced by diaphragm displacement measurements". In: *AIP Advances* 9.2.

Zhang, Yanzhen et al. (2022). "Suppression and Utilization of Satellite Droplets for Inkjet Printing: A Review". In: *Processes 2022, Vol. 10, Page 932* 10.5. ISSN: 2227-9717. DOI: 10.3390/pr10050932. URL: https://www.mdpi.com/2227-9717/10/5/932.

Zhao, Dengke et al. (2021). “Drop-on-demand (DOD) inkjet dynamics of printing viscoelastic conductive ink”. In: *Additive Manufacturing* 48. ISSN: 22148604. DOI: 10.1016/j.addma.2021.102451.